Optical and Magnetic Control of Electron Spins in Tailored Semiconductors

Dissertation

presented to the Faculty of Physics of the
Technische Universität Dortmund, Germany,
in partial fulfillment of the requirements
for the degree of

Doktor rer. nat.

by
Lukas Langer

Dortmund, August 2016

Contents

1 Introduction **1**

2 Theoretical considerations **5**
2.1 Semiconductors and quantum well structures 5
2.2 Optical excitations 9
2.2.1 The Rabi problem 10
2.2.2 Density matrix and optical Bloch equations 12
2.2.3 Damping 14
2.2.4 Photon echoes 16
2.2.5 Selection rules 19
2.2.6 Spin dynamics in semiconductors 22
2.3 Magnetism 25
2.3.1 Paramagnetism 26
2.3.2 Ferromagnetism 29

3 Experimental approach **35**
3.1 Samples 35
3.1.1 CdMnTe bulk crystal 35
3.1.2 GaAs-based semiconductor/ferromagnet hybrid structure . . . 37
3.1.3 CdTe-based quantum wells 37
3.2 Photoluminescence spectroscopy 38
3.2.1 Polarization-resolved photoluminescence 39
3.2.2 Spectrally resolved photoluminescence 40
3.2.3 Time-resolved photoluminescence 41
3.3 Magneto-optical Kerr effect 42
3.3.1 Time-resolved Kerr rotation 42
3.4 Four-Wave-Mixing spectroscopy 43
3.4.1 Optical setup 45
3.4.2 Optical heterodyne detection and signal recovery 47
3.4.3 Principle of measurement 48

4 Resonant optical orientation of Mn^{2+} spins in bulk CdMnTe **51**
4.1 Time-integrated studies 51
4.2 Time dependence 54

4.3 Role of the spin glass phase . . . 55
4.3.1 Temperature dependence . . . 56
4.3.2 Power dependence . . . 56
4.3.3 Comparison with ZnMnSe . . . 57
4.4 Theoretical modeling . . . 59
4.5 Conclusion . . . 62

5 Spin polarization in a ferromagnet/semiconductor hybrid structure 65
5.1 Characterization and influence of the ferromagnetic layer . . . 65
5.2 Determination of the polarized charge carrier . . . 68
5.3 Spin-dependent capture of charge carriers . . . 70
5.4 Kinetics of spin dependent capture . . . 76
5.5 Temperature dependence . . . 78
5.6 Conclusion . . . 79

6 Transfer of coherence via photon echoes 81
6.1 Spectral dependence of four-wave-mixing . . . 81
6.2 Power dependence of four-wave-mixing . . . 82
6.3 Spontaneous photon echo . . . 83
6.3.1 Linearly polarized excitation . . . 89
6.3.2 Spectral dependence of T_2 . . . 92
6.4 Stimulated photon echo . . . 93
6.4.1 $\sigma^+\sigma^+\sigma^+$ polarized excitation in magnetic field . . . 94
6.4.2 Linearly polarized excitation in magnetic field . . . 97
6.4.3 Spectral dependence of T_1 . . . 101
6.5 Conclusion . . . 102

7 Summary 105

A Calculation of the spontaneous photon echo amplitude 107

B Calculation of the stimulated photon echo amplitude 111

Bibliography 115

1 Introduction

The huge amount of information that is available to and produced by mankind gives indication of the importance and complexity of information processing and storage technology [1]. The cited study by Hilbert and López estimates a global data amount of 300 exabyte already in 2007, the year in which the first iPhone was introduced by Apple Inc [2]. The amount and traffic of digital data is further increasing, alongside with the requirement of hardware miniaturization for the availability on portable devices.
A good measure for the complexity of such technologies is Moore's law [3], stating that the number of transistors on a given chip can be doubled every two years, thereby increasing not only the compactness of chips, but also the speed, the efficiency and the affordability of devices. Since its introduction in 1965, several predictions of the law's expiration have been made. Most notably by Moore himself, prognosticating the end of the principle by 2025 [4]. Indeed, a further miniaturization will inevitably reach an end, at the latest when the length-scale of a single atom is reached [5]. But even prior to this hard limit, quantum mechanical effects begin to play a role and perturb the functionality of the devices [6]. Consequently, new concepts of information processing are sought.

In the early 1980's, first ideas were presented to utilize quantum mechanical effects for information processing [7–10], instead of regarding them as a perturbation. A *quantum computer* would exploit the indefiniteness that is inherent to quantum mechanics in order to strongly parallelize the data processing.
In classical systems, the smallest unit of information, the bit, can be in one of two states: either 0 or 1. Its quantum analogue, the *qubit*, is a quantum mechanical two-level system with the eigenstates $|0\rangle$ and $|1\rangle$ and can exist in all the states $|\psi\rangle = \alpha\,|0\rangle + \beta\,|1\rangle$ (with $\alpha, \beta \in \mathbb{C}$ and $|\alpha|^2 + |\beta|^2 = 1$) that are linear combinations of the eigenstates. It has been shown that with this concept and appropriate algorithms [11, 12], certain problems can be solved fundamentally faster than with classical computers using Boolean algebra.
Promising candidates for the physical representation of a qubit include the polarization states of a photon and the eigenstates of a spin-$^1/_2$ particle [13–15].
The photon is already extensively used in today's data communication, although the quantum properties are not yet (fully) exploited. Since the technology for the long-distance transfer is already established, the polarization states of photons are prime candidates for *flying* qubits, whose primary function is the transmission of quantum states. The electron is the foundation of all present-day data processing,

hence the term electronics. For quantum computation, the electron, being a spin-$^1/_2$ particle, would take the function of an *anchored* qubit, whose primary role is the availability for manipulation and calculation like a processor register, rather than its transmission. Thus, a coupling of flying and anchored qubits is an essential part of quantum information processing.

It is the transfer of polarization between light and electron spins that provides the subject for the investigations of the presented thesis.

The research on electron spins has boosted their significance for information processing. The discovery of the giant magnetoresistance [16, 17] not only revolutionized data storage by providing the core technology for hard drives. It even brought forth a new field of research known as *spintronics* [18, 19].

While present-day data processing exclusively relies on the transport and manipulation of electric charges, and data storage exclusively makes use of the electrons' spin, in spintronics the potential is extended by combining both degrees of freedom. Although the quantum character of the spin is not exploited in spintronics and data processing still relies on Boolean algebra, the spin has significant advantages over the charge. If the value (0 or 1) of the bit is encoded in the presence or absence of an electronic charge, for every single switching a Coulomb potential has to be overcome. If the bit is represented by the projections of an electron spin, the energetic difference between the 0 and 1 state is much smaller and the switching is significantly less energy consuming [20–24].

In the last 50 years, all progress in information processing has been closely interlinked with advances in semiconductor technology. The invention of the transistor [25] marked the starting point for miniaturization, circuit integration and optimization of efficiency found in today's hardware. It is therefore not surprising that the blueprint of the central device of spintronics, the spin-transistor, as discussed by Datta and Das in 1990 [26], is based on semiconductor material. Indeed, the manipulation of electronic states in semiconductors benefits from their tremendous flexibility: via band-gap engineering [27] and the variation of charge carrier density by doping or the field effect, semiconductors can be tailored to meet very specific needs. These versatile manipulations are mastered on an industrial-scale level, which is a cause and consequence of the fact that semiconductor technology forms the cornerstone of modern electronics.

In addition to the manipulation of electronic characteristics, the magnetic properties can be modified to a great extent. Doping with magnetic materials grants access to the modification of the spin system in semiconductors. Depending on the employed materials and doping levels, para-, dia-, and ferromagnetic properties can be attained. The most common approach of fabricating semiconductors with particular magnetic properties is by replacing a fraction of the cations of a semiconductor alloy by transition metal ions. The resulting ternary alloys known as *diluted magnetic semiconductors* are subject to extensive research [28–34]. The integration of (ferro-)magnetism into the semiconductor architecture could allow information

processing and storage on the same chip or even in the same material. Their flexible structure, both with respect to electronic and magnetic properties, makes diluted magnetic semiconductors a model system for spintronics.

In addition to their structural flexibility, semiconductors offer a number of gateways for spintronic operations, i.e. spin manipulation. Most commonly used and today most advanced are the electrical and optical approaches [35–37].

Electrical concepts mostly concentrate on the injection of spin-polarized electrons from ferromagnetic materials into semiconductors [38–40], but also use the spin hall effect [41–43], asymmetric magnetoresistance [44, 45], resonant tunneling [46, 47], and spin torque schemes [48–52].

The optical techniques are based on the illumination with polarized light. On the one hand, the magnetic state of a material can be read almost perturbation-free using the Faraday/Kerr effect [53, 54], on the other hand it is possible to directly manipulate spins by optical orientation [55]. Due to the long coherence lengths of modern laser systems, the read-out as well as the manipulation can be realized fully coherently [56–60].

The operation by light is promoted by the excellent optical properties of semiconductors, like their large oscillator strength [61, 62] and the selection rules indicating the dipole-allowed transitions [55, 63]. As already stated above, the integration of light into the spintronic operation principle facilitates the transmission of information tremendously. Furthermore, optical manipulation allows switching rates as high as terahertz and can be easily focused spatially, allowing for small structures.

In spite of these impressive achievements in spintronics, there are still very tough problems to be solved and many details to be understood. This generates interest in sustained fundamental research on electrons and their spins in semiconductors. The development of new materials and operation principles provides the pathway to seminal innovations.

It is the aim of this thesis to explore new approaches for the utilization of the interaction of polarized light with electron spins in semiconductors.

The theoretical framework of said interaction is reviewed in Chapter 2. Semiconductors and semiconductor quantum wells, as well as optical excitations of these materials are discussed (Sections 2.1 and 2.2). Section 2.3 treats magnetic phenomena induced by spin polarization.

The experimental techniques are presented in Chapter 3. The specifics of the investigated samples are described along with the principles of measurement. The optical setups used for the implementation are shown schematically and the necessary equipment is discussed.

In Chapter 4, the direct optical manipulation of electron spins in the diluted magnetic semiconductor CdMnTe is presented. The intra-ion transition of Mn^{2+} ions is excited resonantly by polarized light in a sample which exhibits the collective magnetic phase of spin glass. Thereby, spin relaxation is suppressed. The optical orientation and alignment is evidenced by the photoluminescence of the intra-ion

transition showing a nonzero degree of polarization. This establishes the Mn^{2+} ion as an optically active center available for the optical control of electron spins.

An alternative material system to diluted magnetic semiconductors are hybrid structures comprising a semiconductor and a ferromagnetic layer, separated by a thin (nanometer scale) barrier. The interaction of the two components is of central importance for the functionality of the device as a whole. This interaction was previously identified as the $p-d$ exchange interaction of holes leading to a spin polarization in the semiconductor [64–66]. The experiments presented in Chapter 5 were carried out in a GaAs-based hybrid structure consisting of an InGaAs quantum well and a GaMnAs ferromagnetic layer. Circularly polarized photoluminescence confirms the spin polarization of charge carriers in the semiconductor. The effect of the $p-d$ exchange interaction is quantified in independent measurements but found to be too small to create the observed polarization. Instead, the experiments point to a novel effect that can be described as the spin-dependent capture of electrons by the ferromagnetic layer.

The experiments discussed in Chapter 6 address the operation, rather than the material system. For the full exploitation of the quantum character, the coherence of the quantum state must be preserved in the interaction of light and electron spin [67, 68]. Therefore, it is necessary to utilize a coherent optical process. In condensed matter, one of such processes is the photon echo. It denotes the spontaneous emission of a burst of light from a medium which was previously excited by subsequent, resonant pulses of light [69].

If trions in a semiconductor quantum well are employed for the excitation of the photon echo, the selection rules allow a spin-sensitive excitation with circularly polarized light. The involvement of states with nonzero angular momentum provides an additional degree of freedom for the control of the photon echo by applying an external magnetic field. This is shown in Section 6.3.

Furthermore, it is possible to transfer the optical excitation into the spin-state of the electron. In this way, the external magnetic field also provides a decoupling from the optically accessible states. The reversal of this process by an additional laser pulse permits the optical retrieval of the photon echo, long after expiration of the optical coherence time of the system. This is presented in Section 6.4, where a maximal extension of the echo signal's decay time by three orders of magnitude is reported.

The thesis is concluded by Chapter 7, summarizing the results and giving an outlook to future investigations.

2 Theoretical considerations

In this chapter, the relevant physical processes of light-matter-interaction are discussed. On the material-side, semiconductors provide the basis for the optical manipulation of charge carriers. Special emphasis is laid on quantum well structures (Sec. 2.1) as well as magnetic doping (Sec. 2.3).

Section 2.2 revises different aspects of optical excitations. The treatment of resonances in semiconductors as two-level systems is discussed. Subsection 2.2.1 addresses the interaction of the two-level system with an intensive light pulse in (near) resonance in a semiclassical model. Subsection 2.2.2 extends the approach by including also the effects that are not described by the occupations of the two basis states. The decay of the excitations is treated in Subsec. 2.2.3. An excitation protocol that reverses the decay (partially), namely the photon echo, is introduced in Subsec. 2.2.4. The basis for the integration of the spin's angular momentum in optical excitations is provided by the selection rules reviewed in Subsec. 2.2.5. Subsection 2.2.6 treats dynamics caused by the spin's magnetic moment.

Collective magnetic aspects of spins are recapitulated in Sec. 2.3, where relevant aspects of paramagnetism (Subsec. 2.3.1) and ferromagnetism (Subsec. 2.3.2) are discussed.

2.1 Semiconductors and quantum well structures

Semiconductors are characterized by an energy gap that separates the electronic states of the valence band from those of the conduction band. These bands are defined by their occupation at zero temperature: the valence band is the energetically highest fully occupied band and the conduction band is the lowest unoccupied band. Hence there are no free charge carriers available at zero temperature and the material is insulating. Nonzero conductivity can be induced by the excitation of electrons from the valence band into the conduction band or by the introduction of additional charge carriers via doping.

The semiconductors investigated in this work are *direct* band gap semiconductors: the maximum in energy of the valence band and the minimum in energy of the conduction band are situated at the same point of the first Brillouin zone [62, 70]. In the case of zinc blende crystals like GaAs and CdTe, this is the Γ-point – the center of the Brillouin zone at $\boldsymbol{k} = 0$.

The schematic representation in Fig. 2.1 contains only the bands that are closest

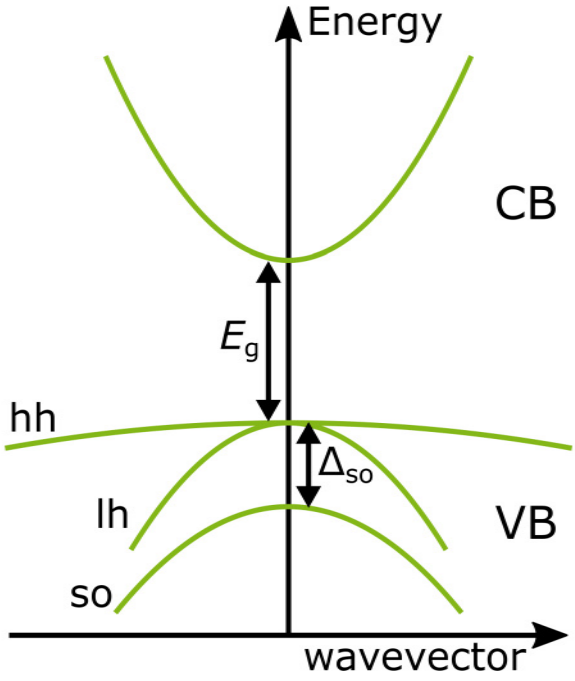

Figure 2.1 Scheme of the band structure of a direct band gap semiconductor near the center of the Brillouin zone. The conduction band (CB) is separated from the valence band (VB) by the band gap E_g. The valence band is composed of heavy hole (hh), light hole (lh), and split-off (so) subbands. Due to spin-orbit interaction, the split-off band is shifted by $-\Delta_{SO}$ with respect to the valence band edge.

to the energy gap and that are therefore relevant for the interaction with light. The conduction band (CB) originates from s-like[1] atomic states, so that the total angular momentum $j = s = 1/2$ of the electronic states is defined by the spin. The valence band (VB) states emerge from p-like atomic states, having a total angular momentum of $j = 3/2$ due to spin-orbit coupling. This results in the formation of three distinct valence bands[2]: the heavy-hole (hh) band with $j = 3/2$, $m_j = \pm 3/2$, the light-hole (lh) band with $j = 3/2$, $m_j = \pm 1/2$ and the split-off band (so) with $j = 1/2$, $m_j = \pm 1/2$. The designation as heavy and light holes stems from the concept of the effective mass defined as

$$m^* = \hbar^2 / \frac{\partial^2 E(k)}{\partial k^2}, \tag{2.1}$$

where $E(k)$ is the electron dispersion relation. The effective mass formalism allows the mathematical description of electrons and holes in semiconductors as free par-

[1] The bands evolve from the hybridization of atomic orbitals. The letters s, p, d, ... denote the value of the angular momentum quantum number l of the respective underlying orbital.

[2] The quantum theory of angular momentum (and their summation) is covered in any quantum mechanics textbook like [71–74], and others.

ticles by representing the influence of the crystal field.
The valence band and the conduction band are separated by the energy gap E_g and the spin-orbit interaction shifts the split-off band by $-\Delta_{SO}$. The split-off energies $\Delta_{SO}^{GaAs} = 0.34\,eV$ [75] and $\Delta_{SO}^{CdTe} = 0.92\,eV$ [75] of the studied materials are substantial, especially compared to the band gaps ($E_g^{GaAs} \approx 1.4\,eV \approx E_g^{CdTe}$ [70]) and render the split-off states irrelevant for optical excitation.

The electronic properties of semiconductors can be influenced by *doping*, the purposeful incorporation of impurity atoms into the semiconductor material. The doping with an element that possesses one valence electron more as compared to the replaced semiconductor host material supplies an additional electron that does not take part in the lattice binding but is instead easily ionized and can be treated as a free (quasi-)particle in the conduction band.[3] In that case the dopant is called a *donor* that causes *n-doping*.
In the opposite case, when the dopant possesses one electron less than the replaced host element, it is referred to as *acceptor*, leading to *p-doping*. By analogy to the case of n-doping, the "missing" electron can be treated as a free particle in the valence band, called *hole*. The concept of holes will be treated in more detail in Sec. 2.2. In both cases the doping leads to an increased conductivity. The effects of doping on other properties of semiconductors will be discussed in the respective sections.

The particularly relevant case of magnetic doping with the transition metal manganese (Mn) will be reviewed in more detail in Sec. 2.3.

The advances in industrial fabrication of semiconductors not only allowed the mastering of doping, but also the development of new material structures, known as nanostructures. These nanostructures possess patterning in the size of the extent of the de Broglie wavelength $\lambda_B = h/p$ (h – Planck constant, p – relativistic momentum) of the electrons and thereby make quantum effects accessible. The concept relies on the combination of materials with different band gaps E_g, creating a potential landscape in which the charge carriers become localized and thereby effectively reducing the dimensionality of the material. Depending on the degree of this confinement, quantum wells (confinement in one dimension), quantum wires (confinement in two dimensions) and quantum dots (confinement in three dimensions) are distinguished [77].
As the experiments presented in this thesis were performed on quantum wells, these are discussed in more detail here.

For the fabrication of quantum wells, a semiconductor material with a smaller band gap is sandwiched between two layers of semiconductor material with a larger band gap. Along with the resulting potential landscape, this is sketched in Fig. 2.2.

[3] The treatment as a free particle is within the scope of the effective mass model, which can only be applied in the case of *shallow* impurities. The low binding energy of the electron is due to the effective mass and the screening of the Coulomb potential by the dielectric constant of the material [76].

As mentioned before, for quantum confinement the thickness of the well must be of the size of the de Broglie wavelength, more precisely, it must be smaller than the mean free path of the charge carrier. The mean free path is strongly dependent on crystal quality, doping and temperature and typically amounts to several hundred nanometer or even a few micrometer [61, 78, 79]. Modern epitaxial crystal growth

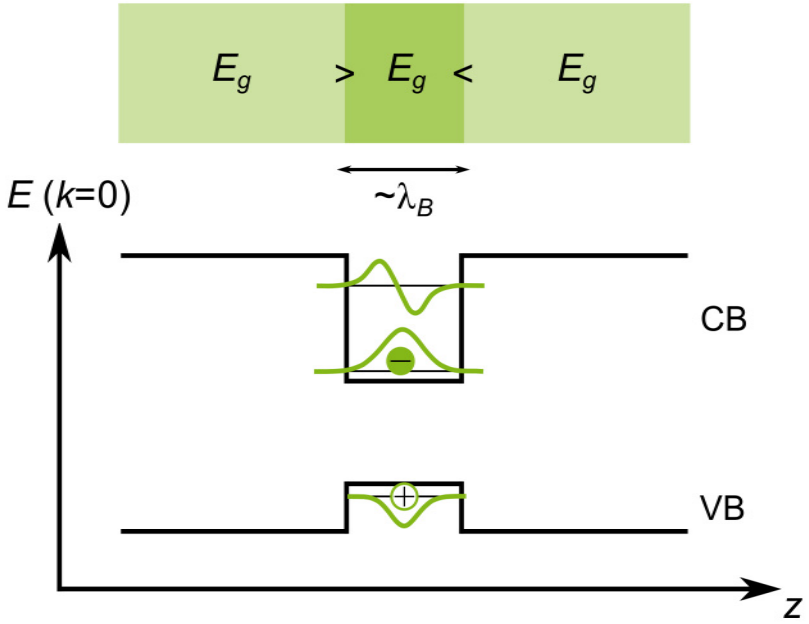

Figure 2.2 Potential curve along the growth direction for a semiconductor with smaller band gap embedded in a semiconductor of larger band gap. Free charge carriers are localized in the region with smaller band gap.

techniques allow precise control over the thickness of quantum well structures. In combination with an abundance of materials and material combinations, a very flexible design of quantum wells, also known as "band gap engineering" [27], is possible. In such a situation, the charge carriers in the medium become localized in the quantum well's potential minimum and the confinement leads to a quantization of the energy levels in the direction perpendicular to the quantum well plane. The motion of a charge carrier within the quantum well plane can still be described as a free particle with an effective mass. Due to the different effective masses of heavy and light holes, their quantization energies are different and the levels for heavy and light holes are split (including at $\boldsymbol{k} = 0$). Moreover, fluctuations in the thickness and/or smoothness of the quantum well lead to additional confinement potentials.

The effects of quantum confinement on the energy levels of the semiconductor also find expression in the optical properties. For example, the binding energy of an exciton will increase, because the electron and hole are close to each other. Excitons and other excitations in semiconductors are the subject of the next section.

2.2 Optical excitations

The fundamental optical excitation in a direct band gap semiconductor consists of the promotion of an electron from the top of the valence band to the bottom of the conduction band. The transition leaves behind an unoccupied state in the valence band. This absence of a negatively charged particle can be treated as a positively charged particle in an otherwise empty band. This concept results in the definition of a quasiparticle known as *hole*. In this picture, the situation in the valence band and in the conduction band are very similar: in both bands there is only a single charge carrier to be taken into account.

Consequently, the properties of both, electron and hole, can be defined by the band structure within the single particle approximation [62], which replaces the influence of the crystal lattice by assigning an effective mass m^* to the charge carrier. By this replacement it is possible to treat electrons and holes in semiconductors like free (quasi-)particles.

Negatively charged electron and positively charged hole are subject to Coulomb attraction. This leads to a bound state called *exciton*, that was first proposed theoretically by Frenkel [80] and confirmed 20 years later experimentally in cuprous oxide [81, 82]. Excitons have been the subject of extensive research in various materials [83–85]. The excitation of an exciton is sketched in the top row of Fig. 2.3.

For the influence of a confinement potential on the exciton properties, the exciton Bohr radius $a_X = a_0 m_0/m^*$ (m_0 – free electron mass, m^* – exciton effective mass, a_0 – hydrogen Bohr radius) has to be taken into account. If the width of the potential is bigger than the exciton Bohr radius, the exciton behaves like a free particle with effective mass $M = m_{\text{electron}} + m_{\text{hole}}$ and the maximum confinement length is determined by the exciton mean free path. In the case of a confinement length that is smaller than a_X, the exciton properties are modified strongly. For example, since the constituting electron and hole are forced closer to each other, the exciton binding energy will increase [61].

The additional binding energy that is introduced due to the quantum confinement paved the way for the discovery of bound complexes that comprise more than two charge carriers. Excitons with one additional bound electron or hole are called *trions* [86] and were first observed in a CdTe quantum well [87] that is similar to the structures studied in this thesis. An additional requirement for the formation of a trion by the binding of a particle to an exciton is the presence of free charge carriers [61]. These can be easily provided by (modulation) doping.
The excitation of a negatively charged trion is sketched in the bottom row of Fig. 2.3. The orientation of spins that is indicated there is determined by the polarization of the exciting light via the optical selection rules discussed in Subsec. 2.2.5.

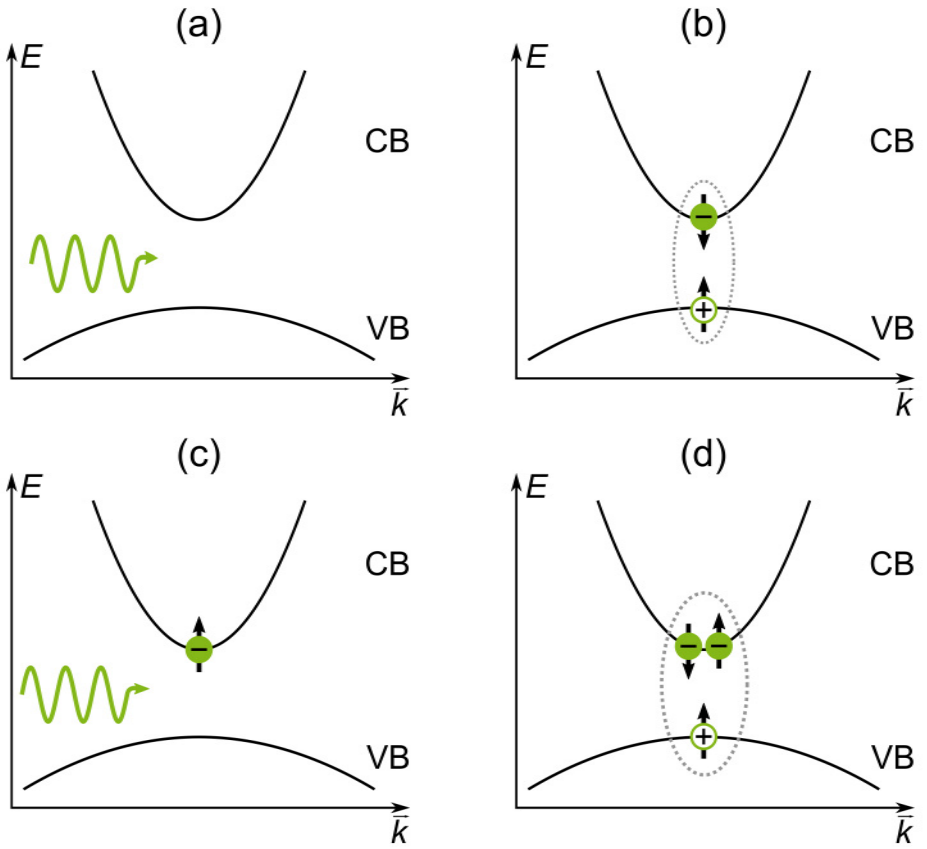

Figure 2.3 Schematic presentation of the excitation of multiparticle states. In a), a photon is absorbed by an undoped semiconductor, promoting an electron from the valence band (VB) to the conduction band (CB) and binding it with the resulting hole into an exciton pictured in b). In c), a photon is absorbed by a n-doped semiconductor, resulting in a bound state of two electrons and one heavy hole called trion, shown in d). The indicated spin-orientations are in accord with the absorption of right-handed circularly polarized light (see Subsec. 2.2.5).

2.2.1 The Rabi problem

For a more thorough treatment of the excitations, the interaction of light and matter will be treated in a semiclassical model.[4] Another simplification comes from the fact that the wavelength of the light (several hundred nanometer) is big compared to the atomic scales of the semiconductor (exciton Bohr radius is about 100 Å, see [61]). This is known as the dipole approximation. Furthermore, only the ground state and the excited state are taken into account, since other states are separated energetically or do not interact due to the localization and the low temperatures maintained in

[4] In the semiclassical approach, the light field is treated classically, while the energy structure of the material is treated quantum-mechanically.

experiment. Such a two-level system is described by the wave function

$$\Psi(\boldsymbol{r},t) = a_1(t)\phi_1(\boldsymbol{r})\mathrm{e}^{-\mathrm{i}E_1 t/\hbar} + a_2(t)\phi_2(\boldsymbol{r})\mathrm{e}^{-\mathrm{i}E_2 t/\hbar}, \tag{2.2}$$

where $|a_n(t)|^2$ denotes the probability[5] for the system to be in the eigenstate described by ϕ_n at time t. The Hamiltonian for the system interacting with an electromagnetic field can be decomposed into an unperturbed part H_0 with eigenenergies E_1 and E_2, and a time-dependent interaction potential $V(\boldsymbol{r},t)$. For a monochromatic plane wave of amplitude E_0 and angular frequency ω

$$V(\boldsymbol{r},t) = -\frac{1}{2}e\boldsymbol{r}\left(\hat{\boldsymbol{e}}E_0\mathrm{e}^{-\mathrm{i}\omega t} + c.c.\right) \tag{2.3}$$

holds in dipole approximation.

For the analytical solution of the Schrödinger equation

$$\mathrm{i}\hbar\frac{\partial}{\partial t}\Psi = (H_0 + V)\,\Psi, \tag{2.4}$$

it is convenient to set the arbitrary zero of energy at E_1, so that only

$$\hbar\omega_0 = E_2 - E_1 \tag{2.5}$$

has to be regarded for the eigenenergies. Furthermore the Rabi frequency Ω_R, which is a measure for the atom-field interaction energy is defined via

$$\hbar\Omega_\mathrm{R} = e\,(\boldsymbol{r}\cdot\hat{\boldsymbol{e}})\,E_0. \tag{2.6}$$

With these substitutions, the Schrödinger equation (2.4) yields

$$\begin{aligned}\dot{a}_1(t) &= \frac{\mathrm{i}}{2}\Omega_\mathrm{R}\mathrm{e}^{\mathrm{i}(\omega-\omega_0)t}a_2(t)\\ \dot{a}_2(t) &= \frac{\mathrm{i}}{2}\Omega_\mathrm{R}\mathrm{e}^{-\mathrm{i}(\omega-\omega_0)t}a_1(t)\end{aligned} \tag{2.7}$$

for the coefficients a_i in (2.2). In this, terms that are $\propto \exp(\pm\mathrm{i}(\omega+\omega_0)t)$ are disregarded, since they oscillate very fast and are therefore averaged to zero in any realistic time interval. This is also known as the *rotating wave approximation* [63]. It is however important to note here, that Eqs. (2.7) hold for resonant ($\omega=\omega_0$) as well as near-resonant ($\omega-\omega_0 \ll \omega$) excitation. In the case of resonance, the solution for the occupations $|a_i|^2$ is

$$\begin{aligned}|a_1(t)|^2 &= \cos^2(\Omega_\mathrm{R}t/2)\\ |a_2(t)|^2 &= \sin^2(\Omega_\mathrm{R}t/2)\,,\end{aligned} \tag{2.8}$$

[5] The commonly used interpretation as probabilities also demands $|a_1(t)|^2 + |a_2(t)|^2 = 1$.

describing a periodic change between ϕ_1 and ϕ_2 with the frequency Ω_R. This is known as *Rabi oscillations*: in an undamped system under continuous excitation, the occupation changes periodically between the ground state and the excited state.

In the case of near-resonance $\omega - \omega_0 \ll \omega$, the occupation probabilities $|a_1(t)|^2$ and $|a_2(t)|^2$ have to be modified [63] to take into account the detuning $\Delta = \omega - \omega_0$:

$$\begin{aligned} |a_1(t)|^2 &= 1 - |a_2(t)|^2 \\ |a_2(t)|^2 &= \frac{1}{2}\frac{\Omega_\mathrm{R}^2}{\Delta^2 + \Omega_\mathrm{R}^2}\left[1 - \cos\left((\Delta^2 + \Omega_\mathrm{R}^2)t\right)\right]. \end{aligned} \tag{2.9}$$

As can be seen from (2.9), the detuning Δ changes the frequency as well as the amplitude of the Rabi oscillations.
For a complete description of the system, not only the occupations $|a_i(t)|^2$ need to be taken into account, but coherent superpositions of both states need to be regarded as well. A formalism for this is the *density matrix*, which will be discussed in the following.

2.2.2 Density matrix and optical Bloch equations

The density matrix ρ of a system described by the wave function Ψ is defined as the ensemble average over the product of the ket and bra state vectors [88] with

$$\rho = \overline{|\Psi\rangle \langle\Psi|}. \tag{2.10}$$

The equation of motion for ρ

$$\dot{\rho} = \frac{1}{\mathrm{i}\hbar}[H, \rho] \tag{2.11}$$

follows from the Schrödinger equation in (2.4) and is known as the Lindblad equation. In the case discussed here, the Hamilton operator H consists of the Hamilton operator H_0 for the unperturbed system and the interaction potential V via $H = H_0 + V$. The eigenstates $|i\rangle$ of the unperturbed system fulfill $H_0 |i\rangle = E_i |i\rangle$ with the eigenenergies E_i. The interaction potential $V = e\boldsymbol{r} \cdot \boldsymbol{E}$ is again given by the dipole approximation of the interaction with an electromagnetic wave [88].

In the case of a two-level-systen, the density matrix is of dimension 2x2:

$$\rho(t) = \begin{pmatrix} \rho_{11}(t) & \rho_{12}(t) \\ \rho_{21}(t) & \rho_{22}(t) \end{pmatrix}. \tag{2.12}$$

Thereby the diagonal elements stand for the occupations with $\rho_{ii}(t) = |a_i(t)|^2$ (see Eq. (2.9)). The off-diagonal elements are related to the polarization of the medium and represent coherent superpositions of the states [62, 88, 89]. In this way, the density matrix reflects the entire dynamic of the two-level system and is therefore a

helpful tool for its understanding, as exercised in Chap. 6 and the appendix for the trion resonance in a n-doped semiconductor quantum well.

For the description of the system, the density matrix is used in the optical Bloch equations [89–91]. Thereby it is convenient to not regard the entries of the density matrix themselves, but rather composite variables

$$\begin{aligned} u &= \rho_{21} + \rho_{12} \\ v &= \mathrm{i}(\rho_{21} - \rho_{12}) \\ w &= \rho_{22} - \rho_{11}. \end{aligned} \tag{2.13}$$

The quantities u and v are derived from the (complex) polarization, while w is a measure for the population inversion. With these variables, the time evolution of the system is given by

$$\begin{aligned} \dot{u} &= -\Delta v \\ \dot{v} &= \Delta u + \Omega_\mathrm{R} w \\ \dot{w} &= -\Omega_\mathrm{R} v. \end{aligned} \tag{2.14}$$

It can be seen that u and v are coupled by the detuning Δ, and v and w are coupled by the Rabi frequency Ω_R. In 1957, a geometrical interpretation of this finding[6] was published, in which the variables u, v, w are understood as the elements of a three-dimensional *Bloch vector* $\boldsymbol{B} = u\hat{\mathbf{1}} + v\hat{\mathbf{2}} + w\hat{\mathbf{3}}$ [92].

Any state of the system can thus be represented by a point in three-dimensional space. Since damping is not included in (2.14), all states must have the same distance from $(0, 0, 0)$, meaning that they all lie on the surface of a sphere, the *Bloch sphere*, as shown in Fig. 2.4. The eigenstates of the two-level system are represented by the poles of the sphere, along the $\hat{\mathbf{3}}$-axis. The action of a resonant laser pulse is expressed as a rotation about the $\hat{\mathbf{1}}$-axis and the action of the detuning Δ is illustrated by a rotation about the $\hat{\mathbf{3}}$-axis. It is in this context, that the concept of the pulse area

$$\Theta = \int_0^{\tau_p} \Omega_\mathrm{R} \mathrm{d}t, \tag{2.15}$$

with τ_p meaning the duration of the interaction, is used to describe the action of a laser pulse on a two-level system. The pulse area is measured in multiples of π and is equal to the angle of rotation of the Bloch vector about the $\hat{\mathbf{1}}$-axis. With this concept, it is possible to graphically follow the action of pulses, as is done in Figs. 2.5 and 2.6 for the photon echo.

[6] The original paper discussed magnetic resonance theory, but the concept can be applied here as well.

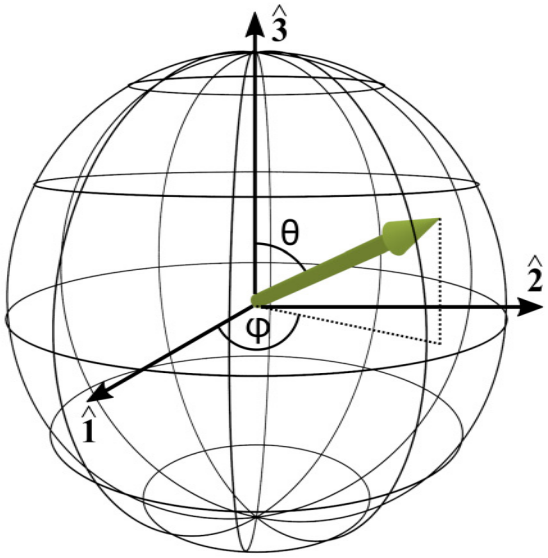

Figure 2.4 A Bloch sphere for the illustration of a quantum mechanical two-level system. The poles of the sphere denote the eigenstates of the system. The Bloch vector (green) represents the quantum mechanical state of the two-level system, where the polar angle is a measure for the proportion of the basis vectors and the azimuthal angle is a consequence of the detuning between the driving field and the eigenfrequency of the system.

2.2.3 Damping

The most obvious damping mechanism is due to the loss of energy to the system's environment by scattering or recombination. This is accompanied with the decay of the excited state into the ground state. In case of a radiative decay, the selection rules discussed in Subsec. 2.2.5 apply. The decay occurs with a constant rate and therefore yields an exponential law describing the number of excited charge carriers

$$N(t) = N_0 \exp(-t/T_1). \tag{2.16}$$

The time constant T_1 describes the lifetime of the excited state. Since this process only concerns the occupations ρ_{ii}, it only affects the optical Bloch equation for the parameter w (compare (2.14)), which is modified to

$$\dot{w} = \frac{1-w}{T_1} - \Omega_\mathrm{R} v. \tag{2.17}$$

In addition to that, there are also elastic processes. These are scattering events with lattice defects, phonons and other excitations, causing arbitrary jumps of the phase and thereby deteriorating the coherence of the system. Since only the polarization is susceptible to decoherence, only the Bloch equations for the parameters u

and v have to be modified. For a constant scattering rate, resulting in an exponential decay of the polarization

$$P(t) = P_0 \exp(-t/T_2), \tag{2.18}$$

the respective optical Bloch equations read

$$\begin{aligned} \dot{u} &= -\frac{1}{T_2} - \Delta v \\ \dot{v} &= -\frac{1}{T_2} + \Delta u + \Omega_\mathrm{R} w. \end{aligned} \tag{2.19}$$

Thereby it has to be kept in mind that the coherence of the polarization is also limited by the lifetime T_1 of the excited state. The overall coherence time T_2 is defined by

$$\frac{1}{T_2} = \frac{1}{2T_1} + \gamma, \tag{2.20}$$

where γ describes the decoherence due to purely elastic processes. This means that if the decoherence is only due to population relaxation, $T_2 = 2T_1$. For a nonzero contribution of elastic processes, the decoherence time is shorter than the double lifetime $T_2 < 2T_1$. In both cases the factor of two stems from the fact that the polarization is governed by the field amplitude, while the population is defined by the square of the field amplitude.

For inhomogeneously broadened ensembles, an additional damping mechanism can be identified, that does act neither on the occupation nor on the polarization of the two-level systems described so far, but is instead a consequence of the superposition of many of theses systems.[7]
Instantly after the excitation, all oscillators are in phase with the light field and their superposition creates a macroscopic polarization. Due to inhomogeneous broadening and the resulting distribution of eigenfrequencies of the two-level systems, the oscillators gradually pick up different phases with respect to the exciting light field. This can be described as an effective detuning from the light field frequency. As Eq. (2.14) shows, a detuning leads to an interchange of u and v, which can be shown as a rotation in the equatorial plane of the Bloch sphere. The value of the polarization of the individual two-level systems is not affected. Only their phases change, depending on the respective detuning. Due to this distribution of different phases, the superposition of the polarizations of all oscillators cancels and a loss of the macroscopic polarization occurs. This decay is known as *free polarization decay* and can be characterized by the dephasing time T_2^*. The Bloch equations do not need to be modified with T_2^*, since they describe individual two-level systems

[7] The density matrix in Eq. (2.10) was defined as the ensemble average.

only. It is important to note here, that the individual oscillators are not affected by the free polarization decay and can maintain their coherence beyond T_2^*. Therefore $T_2^* \leq T_2$ must always be the case. The exact relation of T_2^* and T_2 is defined by the relative importance of inhomogeneous and homogeneous broadening for the respective system under study. In most systems (including systems considered in Chap. 6), the inhomogeneous broadening is much larger than the homogeneous broadening, making $T_2^* \ll T_2$.
Furthermore, the dephasing can be reversed, restoring the macroscopic polarization. This peculiarity is used in photon echo experiments as discussed in the next subsection.

2.2.4 Photon echoes

The term *photon echo* denotes the delayed emission of light from a medium previously irradiated by two (or more) subsequent, coherent, resonant pulses of light. This phenomenon makes use of the reversibility of the dephasing of an inhomogeneously broadened ensemble (see Subsec. 2.2.3) and was first observed in ruby in 1964 [69]. Since then, photon echoes have been studied in different material systems like atomic vapors [93], rare earth crystals [94] and semiconductors [95–97]. Spontaneous as well as stimulated photon echoes were reported and employed in the spectroscopy of energy levels and in the investigation of the coherent evolution of optical excitations [98–100]. Recently, photon echoes have attracted attention for their application in quantum storage schemes [67, 68, 101].

In this subsection, the basics of the photon echo process are reviewed for the excitation of an ensemble of two-level systems. Special emphasis is laid on the relation to the time constants discussed in Subsec. 2.2.3. Depending on the number of exciting laser pulses, spontaneous and stimulated photon echoes can be distinguished, as will be done in the following.

Spontaneous photon echoes

The medium is excited coherently by a laser pulse, creating a macroscopic polarization. The ensemble starts dephasing due to the inhomogeneous distribution of oscillator-eigenfrequencies. This leads to a fast decay of the macroscopic polarization with time constant T_2^*. The (microscopic) polarization of the individual oscillators, however, decays with time constant T_2 (see Subsec. 2.2.3). After a time τ_{12} the (dephased) ensemble is hit by a second laser pulse that inverts the phase the oscillators so that a rephasing process begins. The rephasing occurs at the same rate as the dephasing did before so that the macroscopic polarization is restored at time $2\tau_{12}$ after the incidence of the first pulse.

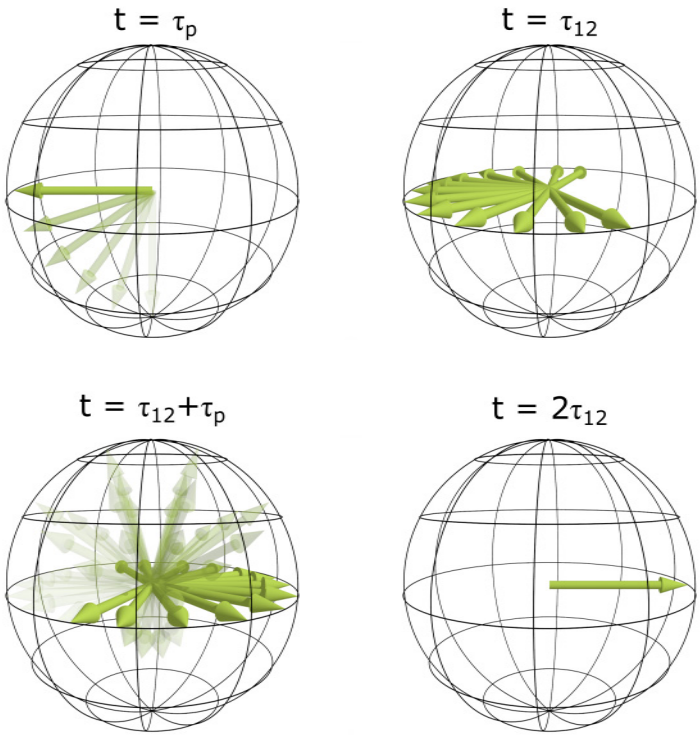

Figure 2.5 Depiction of the spontaneous echo process with Bloch spheres. The first laser pulse excites the two-level systems from the ground state into a coherent superposition of the ground state and the excited state during the pulse duration τ_p. During the delay between the pulses τ_{12}, the ensemble dephases. The second pulse inverts the phases of the individual two-level systems during the pulse duration τ_p. The inverted phases lead to a rephasing of the ensemble which is complete at $2\tau_{12}$.

This process is pictured in Fig. 2.5 with the help of (modified) Bloch-spheres, in which instead of a single two-level system the entire ensemble is displayed. In this representation, the laser pulses are displayed as having pulse areas (see (2.15)) of $\pi/2$ and π for the first and second pulse, respectively. Before any excitation, the system is in the ground state ($\rho_{11} = 1, \rho_{22} = 0$), represented by an arrow pointing to the south pole. The first laser pulse with pulse area $\Theta = \pi/2$ excites a coherent superposition of the ground state and the excited state, depicted by a rotation of the vector into the equatorial plane during the pulse duration τ_p. Due to the inhomogeneous broadening, not all dipoles are excited with their respective eigenfrequency and a relative phase between the dipoles builds up, represented by a spread of arrows in the equatorial plane. After a time τ_{12}, the second pulse of pulse area $\Theta = \pi$ arrives, reversing the phase (i.e. adding a phase of π) of the dipoles. This is shown as a further rotation of the arrows, around the same axis as for the previous pulse, but with an angle of π. Subsequently, the relative phase of the dipoles is annihilated due to the spread of eigenfrequencies and at $t = 2\tau_{12}$

all dipoles are in phase again, restoring the macroscopic polarization and producing a photon echo. The in-phase dipoles are again pictured as a single arrow in the equatorial plane.

It is important to note that the coherence that was introduced by the first laser pulse remains in the equatorial plane of the Bloch sphere. The coherent state is a superposition of the ground state and the excited state. Therefore, the observation of the spontaneous photon echo is limited by the (optical) coherence time T_2 of this superposition. Hence the amplitude of the electric field emitted during the photon echo can be described with

$$P \propto \exp(-2\tau_{12}/T_2). \tag{2.21}$$

This situation can be changed when a *stimulated* photon echo is studied.

Stimulated photon echo

The stimulated photon echo comprises an additional, third pulse. The situation can be regarded as a spontaneous echo with the second pulse split into two separate pulses. However, a closer look reveals also a qualitative change. In Fig. 2.6 the time evolution of the laser-induced coherence is shown. As before, the first pulse ($\Theta = \pi/2$) excites a coherent superposition of the ground state and the excited state and the ensemble starts dephasing. The second pulse again induces a rotation about the $\hat{\mathbf{1}}$-axis, but the pulse area is smaller compared to the situation of the spontaneous photon echo so that the angle of rotation is also smaller. In the case of a $\pi/2$ pulse, the coherence is transferred into the $\hat{1}\hat{3}$-plane. This means that part of the coherence is encoded in the occupation of the ground state and the excited state. In this condition, the coherence of the system is no longer affected by elastic processes, but is limited only by population relaxation, occurring with a characteristic time constant T_1 (see Subsec. 2.2.3). A third pulse of pulse area $\Theta = \pi/2$ then completes the rotation back into the equator plane and induces the rephasing and the photon echo.

Since the dephasing took place only during the delay τ_{12} between the first and the second pulse, the rephasing is complete at time τ_{12} after the third pulse. Accordingly, for a delay of τ_{23} between the second and third pulse, the time of echo emission after the first pulse is

$$t_{\mathrm{SPE}} = 2\tau_{12} + \tau_{23}. \tag{2.22}$$

The complete time dependence of the signal is determined by the coherence time T_2 and the lifetime T_1 of the excited state, depending on what sequence of the process is regarded. During the times in which the system is in the equator plane (i.e. between the first and second pulse and between the third pulse and echo emission), the decay is the same as in the spontaneous echo case. When the system is in a

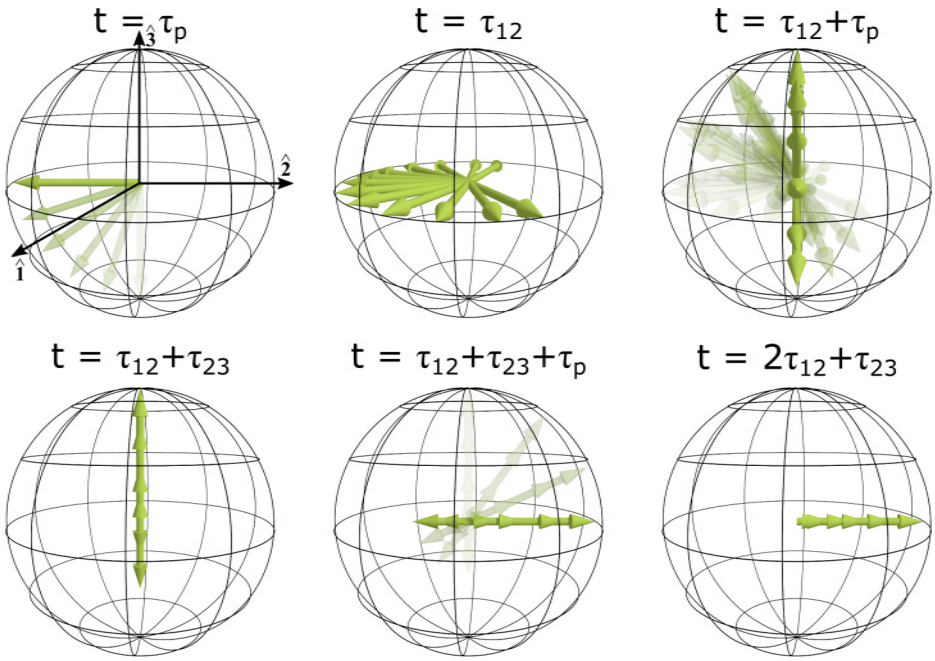

Figure 2.6 The process of the stimulated photon echo illustrated with Bloch spheres. The first laser pulse creates a coherent superposition of the ground state and the excited state. During the delay τ_{12} between the pulses, the ensemble dephases. The second laser pulse encodes the optically excited coherence in the population. All components that are not parallel to the vertical axis are still subject to dephasing and will average out during τ_{23}. The third laser pulse brings the system back into the equatorial plane and induces the rephasing. The stimulated echo is emitted at τ_{12} after the third pulse.

state that is described by occupations (i.e. during the time τ_{23} between the second and the third pulse), the decay is governed by the lifetime of the excited state. A typical experiment for the stimulated echo leaves the delay τ_{12} between the first and second pulse constant and only varies the delay τ_{23} between the second and third pulse, as described in the last paragraph of Subsec. 3.4.3. In this way, the signal follows

$$P \propto \exp(-\tau_{23}/T_1), \tag{2.23}$$

granting access to the lifetime T_1 of the excited charge carriers.

2.2.5 Selection rules

For the optical excitation of charge carriers in semiconductors not only the band gap has to be bridged. The excitation process must also conserve the angular mo-

mentum.[8]
Circularly polarized light carries an angular momentum of $l_{\text{photon}} = 1$. Upon the absorption, this angular momentum is transferred to the medium, so that only transitions with a change in angular momentum by $\Delta l = \pm 1$ can be excited. Taking into account the quantum numbers of the involved states, the optical selection rules, coupling the polarization of light and the polarization of spins, can be derived from these principles. For the general case of dipole-allowed transitions in bulk direct band gap semiconductors, the selection rules are shown in Fig. 2.7.

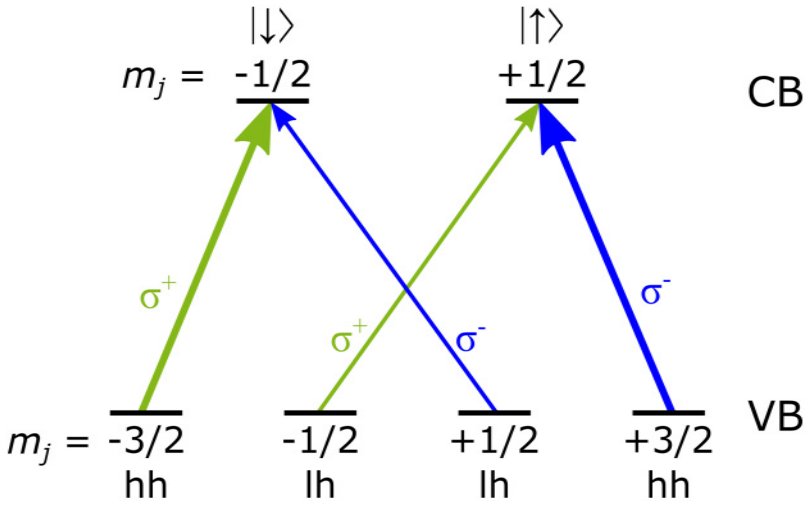

Figure 2.7 Electric dipole-allowed transitions for $\boldsymbol{k} = 0$ and circularly polarized light. Transitions from the p-like ($j = 3/2$) valence band into the s-like ($j = s = 1/2$) conduction band must conserve angular momentum. The different projections m_j for heavy and light holes result in different transition probabilities for the conduction band states for right- (σ^+) and left-handed (σ^-) circularly polarized light. Transitions from the heavy hole band are three times more probable than from the light hole band.

The absorption of σ^+ (i.e. right-handed circularly) polarized light can either lead to a transition between the $m_j = -3/2$ heavy hole state and the $m_j = -1/2$ electron state or the $m_j = -1/2$ light hole state and the $m_j = +1/2$ electron state. The transitions occur with a probability ratio of 3:1, indicated by the thickness of the respective arrow in Fig. 2.7. For the opposite polarization σ^-, the signs of the m_j states must be reversed.
Linearly polarized light can be described as a superposition of σ^+ and σ^-. The action is hence a superposition of the described transitions.

For the more specific case of trions in n-doped CdTe quantum wells, the selection rules are pictured in Fig. 2.8. There, the ground state is constituted by the resident

[8] The conservation of momentum is fulfilled in optical transitions, because the momentum of the photon is negligibly small compared to the dispersion of the band structure.

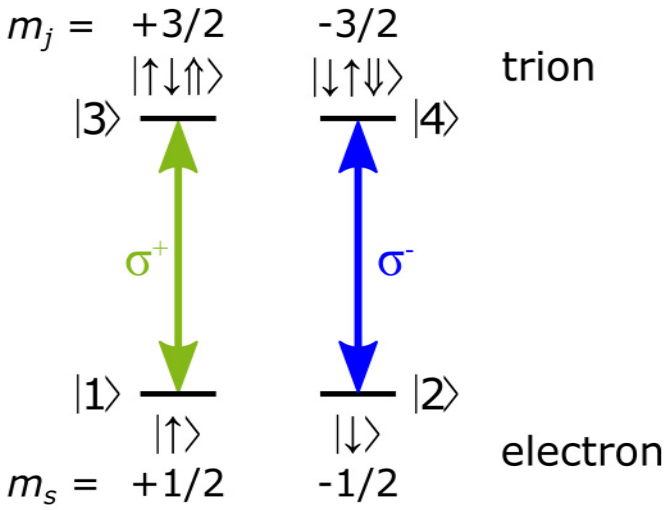

Figure 2.8 Selection rules for the excitation of trions from an electron state with circularly polarized light. Right-handed (σ^+) circularly polarized light drives the transition between the $m_s = +1/2$ electron state $|1\rangle$ and the $m_j = +3/2$ trion state $|3\rangle$, while left-handed (σ^-) circularly polarized light drives the $|2\rangle \leftrightarrow |4\rangle$ transition.

electron and the excited state is the trion. More specifically, it is a heavy hole trion in its ground state with the electrons forming a spin-singlet (see Tab. 2.1).

Again, the spin orientation of the optically addressed states is directly related to the circular polarization of light. The ground states are defined by the resident electron's spin orientation, while for the excited states, the orientation of the hole spin of the trion is the distinguishing property. Right-handed circularly (σ^+) polarized light connects the $m_j = 1/2$ electron and the $m_j = 3/2$ trion state and σ^- polarized light works on the other pair of states with reversed signs for the m_j. Linearly polarized light acts on both pairs of states.

Selection rules govern all optical transitions in semiconductors. Not only the spin configurations of free excitons and trions are subject to selection rules. Depending on the band structure and the impurity complexes, many different other excitations are possible, such as bound excitons and trions and intra-ion transitions in dopants.

In all cases, the absorption of polarized light has a direct effect on the spin state of the excited charge carriers. The injection of spin-polarized charge carriers by circularly polarized light is known as *optical orientation* [55]. It grants access to the optical excitation, purposeful manipulation and investigation of the spin system and forms the basis of many spectroscopic techniques (see Sec. 3.2).

So far, the spin has been treated in the context of band structure and optical excitations. In this frame, it is sufficient to consider the angular momentum that is associated with the spin. But the angular momentum of a charged particle gives rise to a magnetic moment which is the fundamental object of magnetism. The polarization of magnetic moments causes magnetism. That this is also valid for the

magnetic moments of electron spins was confirmed experimentally by the discovery of electron spin resonance [102, 103].

2.2.6 Spin dynamics in semiconductors

The magnetic properties of the spin are defined by its magnetic moment

$$\boldsymbol{\mu}_s = g\frac{\mu_\mathrm{B}}{\hbar}\boldsymbol{S}. \tag{2.24}$$

The Bohr magneton μ_B and Planck's constant $\hbar$ are fundamental constants [104] and the Landé factor g is a property of the spin-bearing particle. In the case of semiconductors, the value of g is mainly defined by the band structure, as can be seen from the Roth-Lax-Zwerdling relation [105]

$$g = g_0\left[1 - \left(\frac{m}{m^*} - 1\right)\frac{\Delta_\mathrm{SO}}{2\Delta_\mathrm{SO} + 3E_\mathrm{g}}\right], \tag{2.25}$$

describing the Landé factor for bulk material. Apart from the Landé factor for free electrons $g_0 \approx 2$ and the electron mass m, all parameters (E_g – band gap, Δ_SO – spin-orbit energy, m^* – effective mass, see Fig. 2.1) are determined by the semiconductor material.

The confinement of charge carriers in nanostructures strongly alters the potential landscape and induces anisotropy. In a phenomenological approach, this can be understood in the following way: In the directions without confinement (e.g. in the in-plane direction of quantum wells), the band parameters are equal or close to those of the bulk material. In the confinement direction (i.e. in the growth direction for quantum wells), the wave function of the charge carriers extends into the semiconductor material of the barrier. This leads to an admixture of the band parameters of the barrier. Additionally, the charge carriers become localized, which affects the effective mass. Consequently, influencing factors for the value of the Landé factor include the compound and the confinement length of the nanostructure [61, 106].

The response of a spin to an external magnetic field is determined by its Landé factor.

Spin in an external magnetic field

For the action of an external magnetic field $\boldsymbol{B}$ on the spin magnetic moment $\boldsymbol{\mu}_s$ the relative orientation has to be taken into account. The Zeeman effect describes an energy splitting of the components of $\boldsymbol{\mu}_s$ that are parallel to the magnetic field $\boldsymbol{B}$ and is given by

$$E_\mathrm{Zeeman} = -\boldsymbol{\mu}_s \cdot \boldsymbol{B}. \tag{2.26}$$

Obviously, the spin components perpendicular to the external magnetic field are not shifted in energy. Instead, they experience a torque

$$\boldsymbol{L} = \boldsymbol{\mu}_s \times \boldsymbol{B}, \tag{2.27}$$

causing a precession by the magnetic moment about the external magnetic field. This precession is known as the Larmor precession and occurs at the Larmor frequency

$$\Omega_\mathrm{L} = \frac{|g|\mu_\mathrm{B}}{\hbar} B. \tag{2.28}$$

A measurement of the Larmor frequency for different magnetic fields allows the deduction of the Landé factor $|g|$ (see Subsec. 3.3.1).

Also without an external magnetic field, the spin polarization shows a dynamic behavior – it is subject to decay.

Spin relaxation

In general terms, the relaxation of spin polarization is due to fluctuating effective magnetic fields. Such fields can be generated by the Elliott-Yafet, Bir-Aronov-Pikus and Dyakonov-Perel mechanisms as well as by hyperfine interaction with nuclear spins [78].

Depending on the material, every electron interacts with a large number of nuclear spins (hyperfine interaction). These have random orientations, leading to random effective magnetic fields that cause spin relaxation. This mechanism has the characteristics of point-type interaction and is rather weak. The spin relaxation mechanisms to be discussed in the following rely on scattering and are typically much more effective than the hyperfine interaction. Still, for strongly localized electrons, the hyperfine interaction can become the dominant relaxation mechanism, especially for materials with large nuclear angular momenta.

The *Elliott-Yafet mechanism* [107, 108] originates from momentum relaxation in conjunction with spin-orbit interaction. The momentum relaxation is caused by scattering by (optical) phonons and (charged) impurities so that the efficiency of the scattering depends on their concentrations. While the concentration of impurities is a sample property and cannot be influenced, the amount of phonons is temperature-dependent, rendering the Elliott-Yafet mechanism negligible for clean samples at low temperatures [77].

The relaxation due to the *Bir-Aronov-Pikus mechanism* is a consequence of an exchange interaction of electrons in the conduction band and unpolarized holes in the valence band. The spin relaxation rate is proportional to the electron scattering rate and hence proportional to the number of holes. Since a sizeable hole concentration

is required, the Bir-Aronov-Pikus mechanism is important especially for p-doped materials [109].

Unlike the two previously discussed mechanisms, the spin relaxation due to the *Dyakonov-Perel mechanism* is not proportional to the electron scattering rate. In non-centrosymmetric crystals (e.g. such with zinc blende symmetry like GaAs and CdTe), the degeneracy of the conduction band is lifted due to spin-orbit coupling [110]. This, in turn, gives rise to an effective magnetic field $B(\boldsymbol{k})$ that depends on the electron's momentum $\boldsymbol{k}$. The magnetic field therefore acts on the spin *between* scattering events, rather than during. Accordingly, the spin relaxation becomes more efficient when less scattering occurs, i.e. when the impurity concentration decreases. For clean samples usually the Dyakonov-Perel mechanism is the dominant one [77].

The main spin relaxation mechanism for *holes* is a consequence of the band structure. The valence band is split into sub-bands of light and heavy holes, having different spin projections. The strong coupling of spin and orbit as well as heavy and light holes makes momentum scattering very efficient for spin relaxation. Therefore, in bulk material, the spin relaxation of holes is generally much faster than for electrons [109, 111, 112].

The involvement of momentum in the spin relaxation mechanisms motivates the investigation of localization of charge carriers. In the case of quantum wells, where the charge carriers are confined in (only) one dimension, the spin relaxation rate becomes anisotropic. A potential asymmetry in the quantum well gives rise to an additional effective magnetic field due to the Bychkov-Rashba splitting [113, 114]. Still, the spin relaxation due to spin-orbit coupling is generally smaller as compared to bulk material [75].

For holes, the spin structure is very different in quantum wells, as the spin relaxation rate is strongly dependent on momentum [115, 116]. The quantum well potential splits the light and heavy hole sub-bands and decouples them at the center of the Brillouin-zone. Due to this decoupling, holes at the center of the zone (i.e. with zero momentum) experience very low spin relaxation, while for finite momentum, the spin relaxation due to heavy-light hole mixing is still very effective, making the hole spin relaxation much faster than the electron one [117–121].

Through thermal excitation, the strong momentum dependence is equivalent to a strong temperature dependence [109]. For low temperatures, when the particle states are close to the center of the Brillouin zone, the spin evolution will be dominated by excitonic effects [109]:

An important difference of excitons as compared to free charge carriers is the additional electron-hole exchange interaction. When the fine structure of the exciton complex is taken into account, three different relaxation processes can be distinguished. The simultaneous spin-flip of electron and hole, describing the transition between the bright states of the exciton, is associated with the exciton spin relaxation time that is typically in the picosecond range [122, 123]. The spin flip of the exciton-bound hole couples the bright and dark states of the exciton and exhibits a very short

time constant in the picosecond range [124–126]. In the case of the exciton-bound electron, the electron-hole exchange is found to act as a static external magnetic field, which reduces the spin relaxation rate due to energy mismatch [124, 127]. Consequently, the spin relaxation time of the exciton-bound electron is found to be in the nanosecond range [122, 123]. Also for exciton-bound charge carriers, the spin relaxation of holes is significantly faster than for electrons (picosecond-range vs. nanosecond-range, respectively).

In the presence of an external magnetic field, the relaxation times for spins are distinguished with respect to their relative orientation to the field. The time constant T_1 stands for the spin relaxation parallel to the magnetic field. Since the spin directions parallel to the external field represent the energy eigenstates, the relaxation process is an inelastic one. Since it is mostly mediated by phonons, the T_1-relaxation is also called spin-lattice relaxation [128].
The relaxation of the spin components perpendicular to the external magnetic field is accounted for by the transverse relaxation time T_2. In the corresponding relaxation processes, only the phase of the spin state needs to be changed, hence there is no energy transfer necessary. An inelastic relaxation into the ground state, however, also leads to a relaxation of the transverse spin component. Therefore T_2 is limited by T_1.

In order to prevent confusion of the spin-related time constants and the optical relaxation times discussed in Subsec. 2.2.3, the spin-related times will be equipped with an additional superscript, indicating the spin-bearing particle. For instance, the spin relaxation times for electrons will be denoted with T_1^e and T_2^e.

The various different properties and dependencies of spin-bearing particles lead to diverse magnetic phenomena.

2.3 Magnetism

Magnetic phenomena in solid state can be classified as dia-, para- or ferromagnetic. Diamagnetic materials possess no magnetic moment, unless an external magnetic field is applied. In accord with Lenz's law, the action of the induced magnetic moments is opposite to the external magnetic field, attenuating it.
In the case of paramagnetism, permanent magnetic moments are associated with the atoms or molecules of the material due to unpaired electrons. Similarly, permanent magnetic moments that behave paramagnetically also originate from excess electrons, excitons and trions. The interaction among the magnetic moments is very weak, so that they can be assumed to be independent. Without an external field, the magnetic moments will be oriented randomly. The application of an external magnetic field aligns the magnetic moments, enhancing the external field.

A ferromagnet also possesses permanent magnetic moments, but additionally it exhibits a spontaneous magnetization even in the absence of an external magnetic

field. The magnetization is caused by the parallel alignment of the magnetic moments that is generally a consequence of exchange interaction (see Subsec. 2.3.2).

Since the samples studied in this thesis include paramagnetic and ferromagnetic structures, these two will be discussed in more detail in this section. In Subsec. 2.3.1, paramagnetism will be treated. The Brillouin function giving the magnetization of a paramagnet is introduced and the diluted magnetic semiconductor CdMnTe is discussed. Subsection 2.3.2 contains remarks on ferromagnetism that are relevant for the experiments presented in Chap. 5. The exchange interaction as the quantum-mechanical origin of ferromagnetism is discussed as well as the characteristic macroscopic phenomena of hysteresis and the Curie temperature. The ferromagnetic semiconductor GaMnAs is reviewed as a component of the ferromagnet/semiconductor hybrid structure introduced at the end of the subsection.

2.3.1 Paramagnetism

Brillouin function

The magnetization of a paramagnetic material due to an external magnetic field is caused by the thermal occupation of spin-split energy levels. The splitting is caused by the Zeeman effect, which for spin components parallel to the magnetic field is

$$E_{\text{Zeeman}} = -\boldsymbol{\mu}_s \cdot \boldsymbol{B} = m_s g \mu_{\text{B}} B, \tag{2.29}$$

with $m_s = \pm\frac{1}{2}$ for electron spins. The spin projections hence have Zeeman energies of $E_1 = \frac{1}{2} g \mu_{\text{B}} B$ and $E_2 = -\frac{1}{2} g \mu_{\text{B}} B$. For thermal equilibrium, the populations N_1 and N_2 of the split levels are described by the Boltzmann distribution:

$$\begin{aligned} \frac{N_1}{N} &= \frac{\exp\left(\frac{g\mu_{\text{B}}B}{2k_BT}\right)}{\exp\left(\frac{g\mu_{\text{B}}B}{2k_BT}\right) + \exp\left(-\frac{g\mu_{\text{B}}B}{2k_BT}\right)} \\ \frac{N_2}{N} &= \frac{\exp\left(-\frac{g\mu_{\text{B}}B}{2k_BT}\right)}{\exp\left(\frac{g\mu_{\text{B}}B}{2k_BT}\right) + \exp\left(-\frac{g\mu_{\text{B}}B}{2k_BT}\right)}, \end{aligned} \tag{2.30}$$

where N is the total number of spins, k_B is the Boltzmann constant and T is the temperature.

With the substitution $q = \frac{g\mu_{\text{B}}B}{2k_BT}$, the magnetization $M = \frac{1}{2} g \mu_{\text{B}} N (N_1 - N_2)$ can be written as

$$M = \frac{1}{2} g \mu_{\text{B}} N \cdot \frac{\mathrm{e}^{q} - \mathrm{e}^{-q}}{\mathrm{e}^{q} + \mathrm{e}^{-q}} = \frac{1}{2} g \mu_{\text{B}} N \cdot \tanh(q). \tag{2.31}$$

For high temperatures and/or low magnetic fields, this can be approximated via $\tanh(q) \approx q$ to show the simple relation $M \propto \frac{B}{T}$.

This finding is known as *Curie's law* with

$$M = C\frac{B}{T} \tag{2.32}$$

and C being the (material-specific) Curie constant.

In the general case of a particle with angular momentum number J, the Zeeman splitting results in $(2J+1)$ equally spaced energy levels. With

$$p = \frac{Jg\mu_\mathrm{B}B}{k_B T}, \tag{2.33}$$

relating the Zeeman energy and the thermal energy, the magnetization reads

$$M = Jg\mu_\mathrm{B}N \cdot B_J(p), \tag{2.34}$$

where

$$B_J(p) = \frac{2J+1}{2J}\coth\left(\frac{(2J+1)p}{2J}\right) - \frac{1}{2J}\coth\left(\frac{p}{2J}\right) \tag{2.35}$$

is the Brillouin function [70, 129].

CdMnTe

Due to the unique electron configuration of the Mn^{2+} ion, it plays an important role for the magnetic doping of semiconductors [130–132].

The crystal growth procedure for CdMnTe is very similar to the production of CdTe. With the commonly used Bridgman technique [133], $Cd_{1-x}Mn_xTe$ crystals in CdTe zinc blende structure can be produced with manganese accounting for up to $x = 77\,\%$ among the cations [134].

In CdTe, being a II-VI semiconductor, manganese represents an isoelectronic dopant, replacing cadmium at a cation site. In this situation, the Mn atom, having a $[\mathrm{Ar}]3d^5 4s^2$ electron configuration, provides both $4s$ electrons for the crystal binding. The $3d$ shell of the Mn^{2+} ion is half filled, so that all five electron spins can align ferromagnetically (as demanded by Hund's rules [135, 136]). The ground state of the Mn^{2+} is hence characterized by spin $s = 5/2$ and orbital angular momentum $l = 0$.

The effect of the manganese ions is strongly dependent on the manganese concentration x. Roughly three different regimes can be distinguished: paramagnetic, antiferromagnetic and spin-glass-like [137]. For very low concentrations, the manganese ions are magnetically isolated and can be treated individually. Each ion then represents a tiny paramagnet and the total magnetization is proportional to the molar fraction x of manganese. For intermediate Mn concentrations (starting

at $x \approx 0.005$ [138]), the mean distance between Mn ions becomes shorter, favoring the formation of Mn nearest-neighbor pairs and Mn clusters. The coupling of Mn nearest and next-nearest neighbors is mediated by short-range superexchange interaction (see paragraph "exchange interaction" below, in Subsec. 2.3.2), which leads to an antiferromagnetic alignment of the Mn magnetic moments. Accordingly, the magnetization is no longer proportional to the concentration of Mn ions, but shows a nonmonotonic behavior with a maximum at $x \approx 0.12$ [139, 140]. For Mn concentrations of $x > 0.17$ [141] (nearest-neighbor percolation threshold is $x \approx 0.2$ [142]), the Mn clusters can reach the size of the sample. Due to the position of the Mn ions on a fcc sublattice, an antiferromagnetic alignment throughout the cluster is not possible. This is known as *frustration* [143]. In connection with low temperatures, i.e. when the thermal energy is below the exchange energy, this leads to a magnetic phase called *spin glass* [144–146]. The term accounts for the random but stable spin orientations in the low-temperature state that is analogous to the positional disorder found in chemical glass.

The existence of the spin glass phase can be evidenced by the temperature dependence of the magnetization of the medium [140, 147]. More precisely, the presence of a spin glass phase leads to a deviation of the magnetic susceptibility from the Curie-Weiss law [70, 148] at low temperatures [138]. An additional property of the spin glass phase is the dependence of the magnetization on whether the sample is cooled in the presence or absence of a magnetic field.

The effect of manganese on the CdTe band structure is restricted to the increase of the band gap with rising Mn concentration, while the shapes, symmetries and characters of the valence and conduction bands are not affected by doping with Mn [134].

The linear increase of the absorption edge with increasing Mn content is pinned at about 40 % [149, 150] due to the onset of absorption of an intra-ion transition of Mn^{2+}. This transition has an absorption edge of around 2.2 eV (at cryogenic temperatures), independent from the doping concentration x [151, 152].

As already mentioned above, in the Mn ion ground state the electron spins are aligned, forming an $S = 5/2$ spin state with zero orbital angular momentum ($L = 0$) designated as ${}^6S$ (${}^6A_1$ in group theoretical notation). Due to the s-like character, this state is not split by the crystal field.

The first excited state is described by the spin reversal of a single $3d$ electron which gives rise to four quartet states with total spin $S = 3/2$, namely ${}^4P$, ${}^4D$, ${}^4F$, and ${}^4G$. The lowest in energy, the ${}^4G$ state, has a $2L + 1 = 9$-fold degeneracy that is lifted by the crystal field and again split into four states (see Fig. 2.9). The energetically lowest of which is labeled ${}^4T_1$ [130, 132], in accord with the irreducible representation of symmetry group T_d [153, 154].

It is the transition from ${}^6A_1$ to ${}^4T_1$ that is generally accepted as the transition pinning the absorption energy of CdMnTe at 2.2 eV [132, 149, 151].

The experimental findings on optical orientation of Mn^{2+} ions presented in Chap. 4

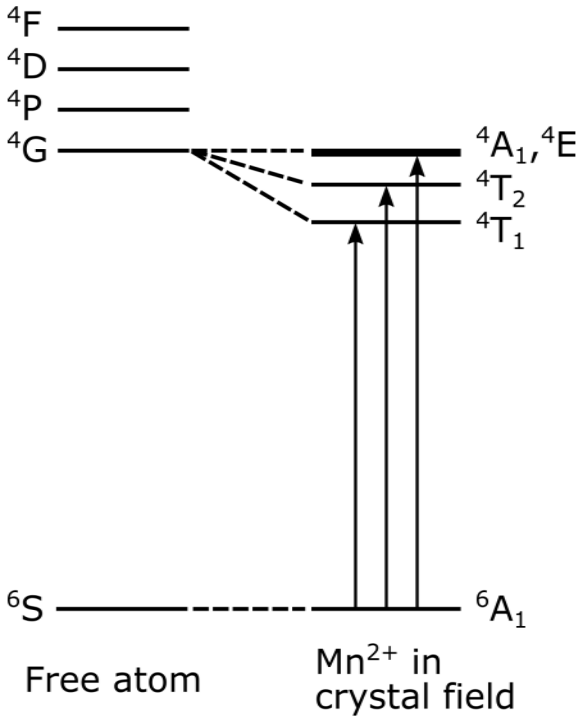

Figure 2.9 Level scheme of manganese. In the crystal field, the lowest excited state (^4G) is split into four states, but the ^6S ground state remains unaltered. Vertical arrows indicate possible intra-Mn transitions. Reproduced from [130], with the permission of AIP Publishing.

were achieved studying this transition.

2.3.2 Ferromagnetism

Exchange interaction

The exchange interaction is a quantum mechanical effect that results from the exchange of indistinguishable particles in a system. Specifically, two electrons at locations $\boldsymbol{r}_1$ and $\boldsymbol{r}_2$, described by individual wave functions $\phi(\boldsymbol{r}_1)$ and $\psi(\boldsymbol{r}_2)$ are considered. The wave function of the joint state can be written as a product of single electron states but must be, as for all fermions, antisymmetric (Pauli exclusion principle, [155]). That means that the wave function resulting from a particle swap (exchange) must be the negative of the original wave function. Hence for a symmetric space state, the spin part of the wave function must be antisymmetric and vice versa. The eigenstates of the spin part of a two-electron wave function are listed in Tab. 2.1.

The singlet state Σ_S is antisymmetric and the triplet state Σ_T is symmetric under

eigenstate	m_s	s	$\boldsymbol{S}_1 \cdot \boldsymbol{S}_2$	
$\vert\uparrow\uparrow\rangle$	1	1	1/4	triplet state Σ_T
$\frac{\vert\uparrow\downarrow\rangle+\vert\downarrow\uparrow\rangle}{\sqrt{2}}$	0	1	1/4	
$\vert\downarrow\downarrow\rangle$	-1	1	1/4	
$\frac{\vert\uparrow\downarrow\rangle-\vert\downarrow\uparrow\rangle}{\sqrt{2}}$	0	0	$-3/4$	singlet state Σ_S

Table 2.1 Eigenstates of a system of two spins $\boldsymbol{S}_1$ and $\boldsymbol{S}_2$ with a coupling of the form $\boldsymbol{S}_1 \cdot \boldsymbol{S}_2$. The corresponding values of m_s, s and the eigenvalues are listed along with the degeneracy of the spin state.

particle exchange. The joint wave functions then take the form

$$\begin{aligned} \Phi_S &= \frac{1}{\sqrt{2}} \left[\phi(\boldsymbol{r}_1)\psi(\boldsymbol{r}_2) + \phi(\boldsymbol{r}_2)\psi(\boldsymbol{r}_1)\right] \Sigma_S \\ \Phi_T &= \frac{1}{\sqrt{2}} \left[\phi(\boldsymbol{r}_1)\psi(\boldsymbol{r}_2) - \phi(\boldsymbol{r}_2)\psi(\boldsymbol{r}_1)\right] \Sigma_T \end{aligned} \tag{2.36}$$

and the corresponding energies are

$$\begin{aligned} E_S &= \int\int \Phi_S^* \hat{H} \Phi_S \mathrm{d}\boldsymbol{r}_1 \mathrm{d}\boldsymbol{r}_2 \\ E_T &= \int\int \Phi_T^* \hat{H} \Phi_T \mathrm{d}\boldsymbol{r}_1 \mathrm{d}\boldsymbol{r}_2. \end{aligned} \tag{2.37}$$

Exploiting the eigenvalues of $\boldsymbol{S}_1 \cdot \boldsymbol{S}_2$, the Hamiltonian describing the system can be rewritten to an effective Hamiltonian reading

$$\hat{H}_{\text{eff}} = \frac{1}{4}\left(E_S + 3E_T\right) - \left(E_S - E_T\right) \boldsymbol{S}_1 \cdot \boldsymbol{S}_2. \tag{2.38}$$

Obviously, only the second term is dependent on spin. Its prefactor is referred to as *exchange constant* J, where

$$J = E_S - E_T. \tag{2.39}$$

The sign of J indicates whether the singlet or the triplet is the favored state.

In the *Heisenberg model* [156, 157], defined by the Hamiltonian

$$H_{\text{Heisenberg}} = -\sum_{i>j} J_{ij} \boldsymbol{S}_i \cdot \boldsymbol{S}_j, \tag{2.40}$$

this approach is applied for all neighboring spins of a system (J_{ij} is the exchange constant of spin $\boldsymbol{S}_i$ and spin $\boldsymbol{S}_j$, which, in the simplest case, is assumed to be equal for all nearest neighbors and 0 otherwise). In this way, ordering of spins can be explained even for larger systems.

Although this model provides the basis for the understanding of magnetic ordering, the situation in real systems is somewhat more complicated. Especially the restriction to nearest-neighbor interaction is not compatible with the indirect exchange observed in many systems. For example, the exchange interaction between magnetic ions in metal can be mediated by conduction electrons. In the RKKY interaction [158–160], a localized magnetic moment polarizes the conduction electron spins which then lead to a polarization of the neighboring localized magnetic moment.

In many magnetic alloys, the interaction among magnetic ions occupying next-to-nearest lattice sites is mediated by non-magnetic atoms that are situated on lattice sites between the magnetic ions. This typically antiferromagnetic interaction is known as *superexchange* [161–164].

In the ferromagnetic semiconductor GaMnAs, the long-range ferromagnetic ordering is mediated by a locally antiferromagnetic interaction between the Mn electrons and valence band states (holes). The holes are provided by the doping with manganese itself – see paragraph "GaMnAs" below.

Hysteresis

A unique property of ferromagnets is the hysteresis of their magnetization in dependence of the external magnetic field. That is, the magnetization not only depends on the current value of the external field, but also on its previous value. A typical hysteresis loop is shown in Fig. 2.10. For large external fields, the magnetization reaches a saturation value M_s. When the external field is decreased again, the magnetization also reduces, but at zero external field a nonzero magnetization prevails (upper curve). This is known as the remanent magnetization M_r. In order to fully demagnetize the ferromagnet (i.e. to bring the magnetization to zero), an external field of the opposite orientation with a value of $|H_c|$ is necessary. This field is called the coercive field.

The values of M_r, M_s and H_c are material-specific and can be used to characterize a ferromagnet. Additionally, a ferromagnet can be characterized by its Curie temperature.

Curie temperature

Above a certain temperature, the spontaneous magnetization that is characteristic for ferromagnets vanishes. This temperature is called the Curie temperature T_C and is a material property. For the naturally ferromagnetic elements of iron,

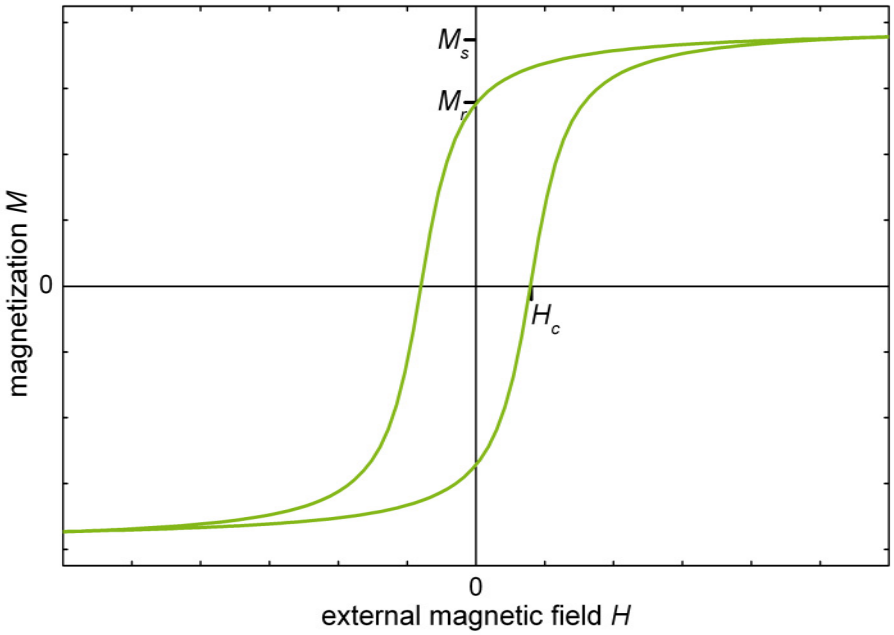

Figure 2.10 A generic hysteresis loop, exhibiting the saturation magnetization M_s, the remanent magnetization M_r and the coercive field H_c.

cobalt and nickel, the Curie temperatures are 1043 K, 1388 K and 627 K, respectively [70]. Among the ferromagnetic semiconductors, manganese plays a central role as a dopant [32, 165, 166]. In these materials, the Curie temperature is strongly dependent on the manganese concentration and the fabrication process. In the case of GaMnAs, for instance, the Mn content can lead to Curie temperatures as high as 172 K [167], but typically values well below 110 K are observed [168]. Additionally, the annealing of the GaMnAs has a profound effect on the Curie temperature [167]. Furthermore, the influence of the surface and thickness of the GaMnAs-layer [169, 170] and its capping [171] leads to a wide range of Curie temperatures [32].

GaMnAs

The most stable position of manganese inside the GaAs lattice is at the cation site [166], replacing a gallium atom (substitutional Mn). In the host lattice, gallium, having a $[\mathrm{Ar}]3d^{10}4s^2 4p^1$ valence electron structure, participates in the crystal bonding with its $4s$ electrons and the $4p$ electron. Manganese ($[\mathrm{Ar}]3d^5 4s^2$) also provides two $4s$ electrons but lacks the $4p$ electron, hence acts as an acceptor and supplies one hole per Mn atom.
A local magnetic moment is introduced by the five $3d$ electrons of manganese. In agreement with Hund's rules [135, 136], the electrons align ferromagnetically, forming a $s = 5/2$ state with zero orbital angular momentum. The hybridization of

these Mn d orbitals with the valence band state of the hole, which has a p character and is centered at the Arsenic anion site, is the origin of the ferromagnetic ordering observed in GaMnAs.

For a collective ferromagnetic ordering, a sufficient density of magnetic moments must be supplied, which is the case for a Mn content of about 2 % or more. This is however well above the Mn equilibrium solubility limit in GaAs [166], so that a non-equilibrium growth technique has to be employed to prevent MnAs clusters and Mn precipitation. This is achieved by low-temperature (about 250 °C) molecular beam epitaxy. The downside of this method is a relatively poor sample quality with a low conductivity [165, 172] and a high concentration of point-defects [32]. Among those, two defects have been identified as the most relevant: the arsenic antisite defect and the manganese interstitial [173]. The former means the presence of an As atom at a cation site, acting as a double-donor and hence compensating the holes provided by the substitutional Mn. The latter defect signifies a Mn atom at an interstitial site of the GaAs lattice, also acting as a double-donor. Additionally, the interstitial manganese exhibits strong local direct antiferromagnetic coupling to neighboring substitutional manganese, reducing the net effective magnetic moment and hence inhibiting the magnetism. It has been shown that post-growth annealing at temperatures around the growth temperature can effectively reduce the impact of interstitial manganese defects [174]. For the healing of As antisite defects, considerably higher annealing temperatures are necessary [175], so that this is not possible without the precipitation of Mn or the formation of MnAs metallic clusters [166].

A suitable parameter for the evaluation of GaMnAs samples is the ferromagnetic transition temperature (Curie temperature) T_C. Not only the annealing has been found to have a profound effect [167] on the Curie temperature, but also the surface and thickness of the GaMnAs-layer [169, 170] and the capping [171] of the sample. In this way, a wide range of Curie temperatures is attainable, but still the ferromagnetism can only be observed below room temperature.

Due to this demanding set of crucial parameters along with the inherent difficulty of low temperature molecular beam epitaxy, a novel approach to ferromagnetic semiconductor structures has been suggested that can be described as a *ferromagnet/semiconductor hybrid system.*

Ferromagnet/semiconductor hybrid structures

The most straightforward way of incorporating ferromagnetism into semiconductors is the manufacturing of a monolithic device with an inherently ferromagnetic functional area.

Examples for this approach, like GaMnAs or InMnAs have allowed remarkable progress [32, 33], but exhibit ferromagnetism only for cryogenic temperatures [168] and show relatively poor charge carrier mobility [165, 172].

An alternative strategy is provided by ferromagnet/semiconductor hybrid struc-

tures [176–178]. Here, the different functions are assumed by individual constituents that are combined to a device fulfilling all the requirements. The important aspect is that all constituents maintain their respective properties without deteriorating those of the other components. The selection and combination of optimal components and materials is the principal task to be solved in this approach.

The preservation of the excellent optical and electrical properties of semiconductor nanostructures in combination with ferromagnetism is possible by spatially separating the semiconductor and the ferromagnet. Modern molecular beam epitaxy allows a monolayer-resolved growth of heterostructures, so that a separation of ferromagnet and semiconductor on the length scale of a few nanometers is possible. This opens the possibility for different mechanisms to mediate the cross-talk between ferromagnet and semiconductor. Among them are the exchange interaction between electrons of the semiconductor and electrons of the ferromagnet, stray fields and tunneling of charge carriers. A long-range effect involving elliptically polarized phonons was published in [179].

3 Experimental approach

This chapter addresses the methods that were used to obtain experimental data. The samples for the resonant manipulation of Mn^{2+} spins, for the investigation of a ferromagnet/semiconductor hybrid structure and for the observation of the photon echo are discussed in the respective subsections of Sec. 3.1. The spectroscopic procedures of photoluminescence (Sec. 3.2), Kerr rotation (Sec. 3.3) and four-wave-mixing (Sec. 3.4) are explained along with the associated optical setups.

3.1 Samples

For the different approaches to combine optics and magnetism in semiconductors, specially tailored samples were used. For the direct optical addressing of electron spins in manganese ions, a bulk crystal of cadmium manganese telluride (CdMnTe) with a high concentration of manganese was used (see also paragraph "CdMnTe" in Subsec. 2.3.1). The sample is described in detail in Subsec. 3.1.1.
To examine the influence of a nearby ferromagnet on carrier spins in a quantum well, a ferromagnet/semiconductor hybrid structure (as introduced in Subsec. 2.3.2) based on gallium arsenide (GaAs) was used. Further details on the sample can be found in Subsec. 3.1.2.
In the third approach, no magnetic doping is involved, but instead the carrier spins of an n-doped quantum well are employed in coherent photon echoes (see 2.2.4). The samples are based on cadmium telluride (CdTe) and presented in Subsec. 3.1.3.

3.1.1 CdMnTe bulk crystal

The CdMnTe bulk crystals were prepared from a $Cd_{1-x}Mn_xTe$ ingot grown by the Bridgman technique [133]. The samples were cut along the (100) cleavage plane into pieces of $5\,\mathrm{mm} \times 5\,\mathrm{mm} \times 0.5\,\mathrm{mm}$ size. The experimental results presented in Chap. 4 comprise samples with three different manganese concentrations: $x = 0.36$, $x = 0.40$ and $x = 0.45$.

All of these concentrations allow a direct access to the intra-ion transition discussed in Subsec. 2.3.1, since the exciton resonance is spectrally well separated and energetically higher (see Fig. 3.1, compare Fig. 4.1).

Additionally, the studied manganese concentrations induce the formation of a spin glass phase at sufficiently low temperatures (see paragraph "CdMnTe" in Sub-

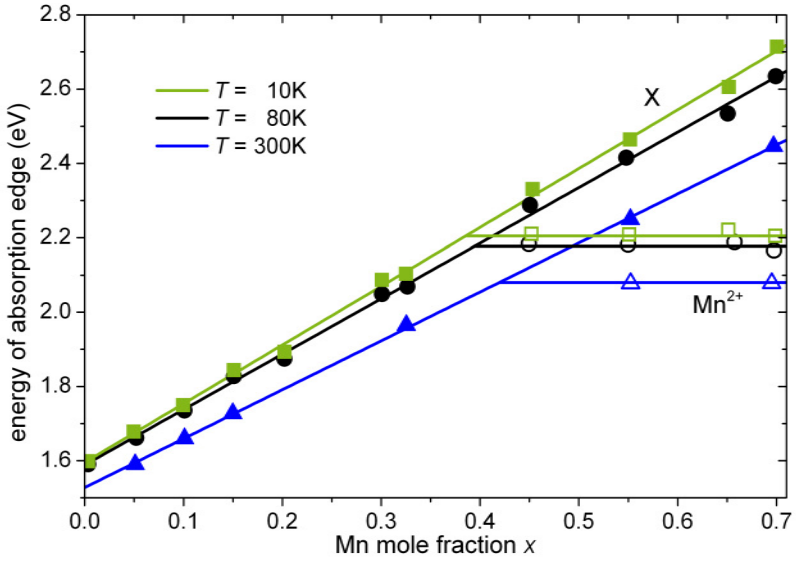

Figure 3.1 Dependence of the absorption edge energy on the manganese concentration x for different temperatures. Due to their dependence on x, the absorption of the exciton (X) and the Mn^{2+} intra-ion transition (Mn^{2+}) can be distinguished. Reproduced from [180], with permission from Elsevier.

sec. 2.3.1). The associated temperatures for the spin glass transition according to [137] are given in Table 3.1.

x (%)	T_{sg} (K)
35	8
40	12
45	18

Table 3.1 Spin glass transition temperatures T_{sg} for different Mn concentrations x in $Cd_{1-x}Mn_xTe$ [137].

In order to study the Mn^{2+} intra-ion transition at low temperatures, but without the influence of the spin glass phase, an additional sample is provided. CdTe as a host material for the Mn ion is replaced by ZnSe. Due to the larger band gap and exciton energy of ZnSe, the direct observation of the Mn^{2+} intra-ion transition is possible already at low Mn concentrations. The studied sample was grown by the same technique as the CdMnTe crystals, but contained a considerably smaller manganese concentration of about 2 %.

3.1.2 GaAs-based semiconductor/ferromagnet hybrid structure

The hybrid structures were grown by metal-organic vapor phase epitaxy [181] in Nizhny Novgorod, Russia. The structures consist of an InGaAs quantum well that is separated by a barrier of GaAs from a Mn-doped layer. The thickness d_S of this barrier is the distinguishing criterion of the individual samples. A schematic representation of the samples is given in Fig. 3.2.

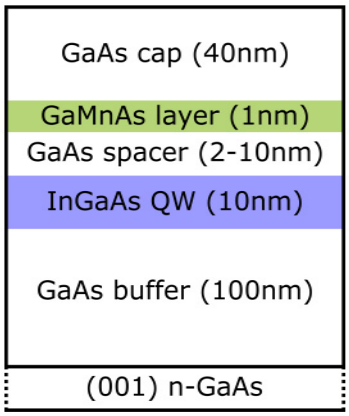

Figure 3.2 Sketch of the studied ferromagnet-semiconductor hybrid structure. The thin ferromagnetic GaMnAs layer (green) resulting from δ-doping is separated from the InGaAs quantum well (blue) by a GaAs spacer. Samples with three differnt spacer thicknesses of 2 nm, 5 nm, and 10 nm were studied (see Chap. 5).

A wafer of n^+-GaAs in (001) orientation serves as a substrate for the samples. A weakly Si doped n-GaAs buffer layer is followed by an InGaAs quantum well with a thickness of 10 nm and an In concentration of about 10 % to 20 %. On top of this, an undoped GaAs spacer was grown. The thickness d_S of this spacer is varied for the three different samples, having values of 2 nm, 5 nm or 10 nm. The GaMnAs-layer is created by δ-doping [182] of Mn into the GaAs matrix, resulting in a 1 nm-thick ferromagnetic GaMnAs layer with a Mn concentration of about 5 %. The ferromagnetism is mediated by Mn-provided holes (see paragraph "GaMnAs" in Subsec. 2.3.2) with a density of $10^{13}\,\mathrm{cm}^{-2}$ to $10^{14}\,\mathrm{cm}^{-2}$ and has a Curie temperature of $T_C \approx 35\,\mathrm{K}$.
Further description and in-depth studies of the samples were performed before by Dorokhin et al. [183] and Pankov et al. [184].

3.1.3 CdTe-based quantum wells

The quantum well sample was grown by molecular beam epitaxy at the Polish Institute of Physics and is identified by the number 031901C. A sketch of the

sample is given in Fig. 3.3. A wafer of (100)-surface oriented GaAs is used as a substrate, on which several layers of CdTe are grown, forming a 2 µm thick buffer layer.

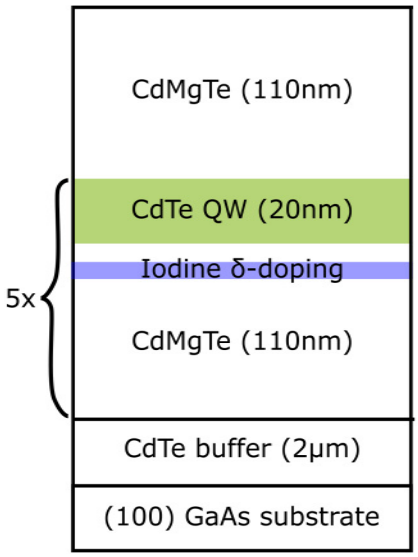

Figure 3.3 Sketch of the CdTe-based heterostructure. Five 20 nm-thick CdTe quantum wells (blue) are separated by CdMgTe barriers of 110 nm thickness. The spacers contain regions with iodine δ-doping (green) near the quantum wells. The excess electrons provided by the iodine diffuse into the quantum wells and form a 2D electron gas.

In this way, the lattice constant is matched to the CdTe-based heterostructure comprising five thin (20 nm) layers of CdTe, separated by $Cd_{0.78}Mg_{0.22}Te$-spacers of 110 nm thickness. Due to the smaller band gap of CdTe, compared to CdMgTe, the thin layers act as quantum wells, trapping free charge carriers. These are provided by modulation-doping of the barriers with iodine donors adding excess electrons to the crystal. The electrons diffuse into the quantum well and are trapped by the potential minimum, forming a 2D electron gas of density $n_e \approx 1 \times 10^{10}\,\mathrm{cm}^{-2}$. The structure is capped by an additional 110 nm CdMgTe layer to reduce the influence of surface charges.

3.2 Photoluminescence spectroscopy

The term photoluminescence denotes the emission of light from matter that was excited optically.

In semiconductors the photoluminescence results from the radiative recombination of photoexcited electrons with holes. The spectroscopy of photoluminescence hence gives insight into the energy level structure of the investigated material. The resolu-

tion of different experimental parameters grants access to the respective properties of the involved charge carriers.

A spectral resolution of the photoluminescence identifies the contributions of different energy levels and transitions, a time resolution gives insight into the radiative lifetimes of the excited states. A polarization-sensitive detection or excitation grants access to the spin-system of the sample, as the optical transitions are subject to selection rules as discussed in Subsec. 2.2.5. Furthermore, a combination of these parameters further increases the potential of this spectroscopic tool. The experimental arrangement for the investigation of photoluminescence is shown in Fig. 3.4.

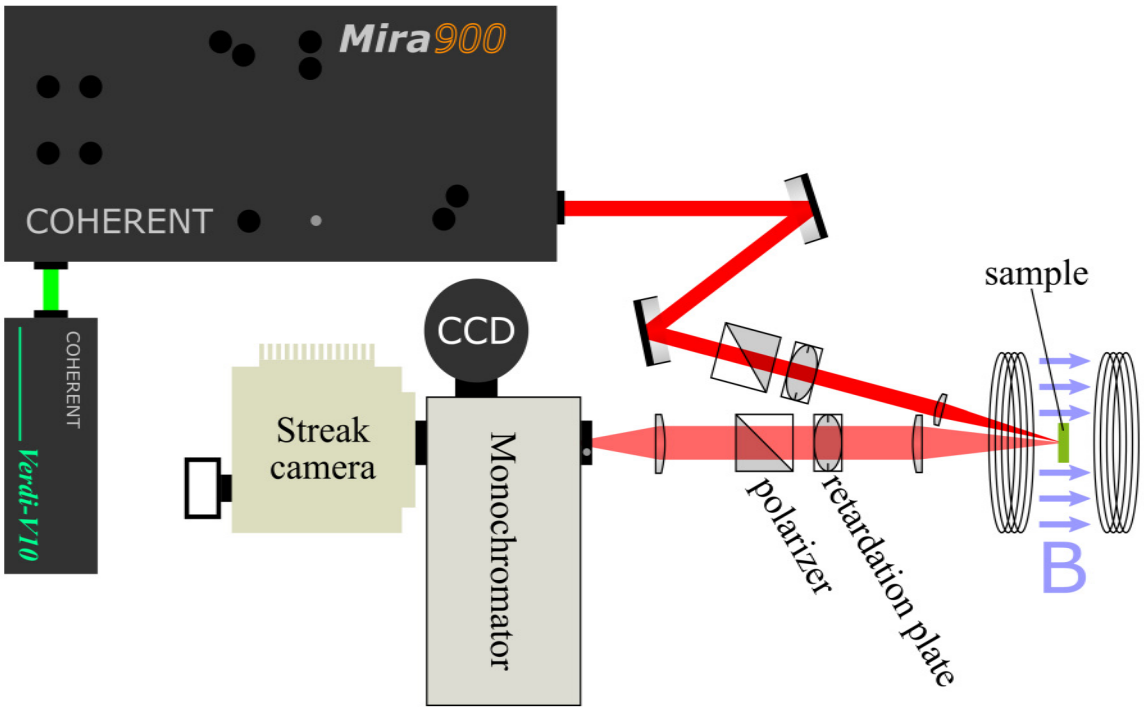

Figure 3.4 Optical setup for photoluminescence spectroscopy. The polarization of the excitation can be adjusted with a polarizer and a retardation plate ($\lambda/4$ for circular, $\lambda/2$ for linear polarizations). The detected polarization is determined by another set of retardation plate and polarizer. For the detection of the full intensity, the retardation plate is replaced by a depolarizer. A monochromator in connection with a CCD camera allows a spectrally resolved and time-integrated measurement of the photoluminescence intensity. For time-resolved investigation, a streak camera is used.

3.2.1 Polarization-resolved photoluminescence

As discussed in Subsec. 2.2.5, the transition of an electron from the *s*-like conduction band to the *p*-like valence band is accompanied by the change of angular momentum.

This leads to the emission of polarized light, whereby the polarization depends on the spin-orientation of the charge carriers, as can be seen in Fig. 2.7.

In the case of right-handed (σ^+) and left-handed (σ^-) circular polarization, the respective intensities I_+ and I_- give a direct measure for the optical recombination rates for the two spin orientations. The degree of circular polarization is defined as

$$\rho_c = \frac{I_+ - I_-}{I_+ + I_-}. \tag{3.1}$$

Analogously, the spin alignment perpendicular to the direction of light propagation can be measured by the degree of linear polarization defined as

$$\rho_l = \frac{I_x - I_y}{I_x + I_y}. \tag{3.2}$$

Thereby I_x and I_y denote the intensities of orthogonally linearly polarized components of the photoluminescence.

As the optical selection rules are also valid for the excitation, the use of polarized light allows the optical orientation of spin-polarized charge carriers. Studying the photoluminescence of optically oriented charge carriers allows the investigation of spin relaxation mechanisms.

In addition to time-resolved approaches, the Hanle effect [55, 185] can be used to determine the spin relaxation time without time-resolving the photoluminescence signal. It is based on the spin depolarizing action of a transverse external magnetic field. Spin-polarized charge carriers are injected optically by circularly polarized continuous-wave excitation. The polarization of the photoluminescence is measured as a function of the external magnetic field applied in Voigt geometry.[1] In the time-integrated detection, the field-induced Larmor precession (Eq. (2.28)) of the injected spins results in depolarization of the photoluminescence with rising magnetic field. The resulting Hanle curve contains information about the dynamic parameters of the spin system.

Experimentally, the polarization of excitation and detection is controlled by retardation plates in connection with polarizers. The laser systems that are employed in the excitation deliver linearly polarized light.

3.2.2 Spectrally resolved photoluminescence

In order to distinguish contributions of different energy levels and transitions, the photoluminescence signal is resolved spectrally. Therefor, a monochromator using a diffraction grating for the spatial separation of photon energies is used. The spectrum is then recorded with the array detector of a charge-coupled device (CCD).

[1] Voigt geometry denotes a configuration in which the magnetic field is parallel to the sample surface, but perpendicular to the direction of light propagation and optically induced spin.

The recorded spectrum indicates the energy, spectral width and intensity of the respective transitions.

A variant of spectrally resolved photoluminescence is the *photoluminescence excitation (PLE)*, in which a distinct feature of the photoluminescence (e.g. the intensity of a single peak) is observed while the excitation energy is scanned. The signal strength is then proportional to the carrier density, which is determined by the absorption coefficient. Accordingly, photoluminescence excitation represents a possibility to measure absorption without the necessity of a translucent sample.

In the experiments discussed in this thesis, both types of spectrally resolved photoluminescence experiments were carried out.
The excitation was implemented with a Titanium-Sapphire-laser Coherent Mira 900 providing a spectral range of 700 nm to 980 nm or by the addition of an optical parametric oscillator from APE offering an extended wavelength range of 505 nm to 4000 nm. Typically the laser sources were run in the mode-locked (i.e. pulsing) regime. The spectral width of the pulses is then typically about 0.8 nm.
The detection was realized with a spectrometer Acton SP2500 from Princeton Instruments, providing a resolution of about 0.1 nm in connection with a CCD camera.

3.2.3 Time-resolved photoluminescence

For time-resolved photoluminescence spectroscopy, the excitation is carried out with a short light pulse. The photoluminescence emission is then recorded as a function of time after the excitation pulse. The detected intensity transients depend on the carrier relaxation and recombination mechanisms and allow a determination of the radiative lifetimes. Likewise, an additional resolution of the polarization (see 3.2.1) grants access to the time constants of the spin system.

In the time-resolved photoluminescence experiments discussed in this thesis, the excitation was again provided by a Coherent Mira 900, either directly or with an additional optical parametric oscillator from APE. Both systems provide laser pulses of $\tau_p < 3$ ps duration.
The detection was accomplished with a Hamamatsu streak camera, achieving a time resolution of 20 ps (synchroscan unit) in the setup combining spectral and temporal resolution as shown in Fig. 3.4.

Alternatively, the modulation of the excitation light source can also be accomplished by an electro-optical modulator. In this way, either a pulse of variable duration (cw-laser) or a picosecond pulse train (ps-laser) of variable duration can be produced. The electro-optical modulator has a switching time of below 1 µs and is operated at repetition rates of several kilohertz. Thus, this variant of excitation is especially favorable for signals that exhibit time constants in the microsecond range. Also in this case, the detection is implemented with the same streak camera, but with exchanged scanning unit (slow single sweep unit instead of synchroscan unit). The temporal resolution is defined by the length of the excitation pulse (train) as

defined by the electro-optical modulator.

3.3 Magneto-optical Kerr effect

The magneto-optical Kerr effect describes the rotation of the polarization plane of linearly polarized light upon reflection from a magnetized surface and was discovered by John Kerr in 1877 [54].

Linearly polarized light can be understood as a superposition of two circularly polarized components. The magnetized material exhibits a spin polarization that gives rise to a difference in refractive indices for the two circular polarizations. Hence the group velocities are not equal for the two components and the reflection produces a phase-lag between them. This phase-lag between circular polarizations is equivalent to a rotation of the polarization plane of linearly polarized light. The angle of rotation is thereby proportional to the magnetization of the medium [129].

For the excitation, a mode-locked Ti:sapphire laser with a pulse duration of 2 ps was used. A linear polarizer in front of the sample ensures the linear polarization of the excitation. The reflected light is passed through a photoelastic modulator (PEM), that is installed with the main axis parallel to the polarization of excitation. In this way, only the part of reflected light, which was rotated out of the original polarization plane is modulated by the PEM. Light that did not experience Kerr rotation is transmitted through the PEM unmodulated. A subsequent polarizer that is twisted by 45° with respect to the excitation polarization translates the polarization modulation into an intensity modulation at the same frequency. The amount of modulated light is thereby proportional to the angle of polarization rotation.

A photodiode detects the intensity of the light and feeds a proportional voltage to a lock-in amplifier, that multiplies the signal with an AC voltage oscillating at the modulation frequency of the PEM. The product of the multiplication is averaged over several oscillations, canceling the contributions of other frequencies (especially the DC component). The output of the lock-in amplifier is a DC voltage that is proportional to the amplitude of the oscillatory signal.

Therefore, the output of the lock-in amplifier is proportional to the intensity of modulated light and hence proportional to the Kerr rotation of polarization and to the magnetization of the sample.

3.3.1 Time-resolved Kerr rotation

A time resolution of the Kerr rotation is possible when a pump-probe scheme with two subsequent laser pulses is implemented. The first laser pulse (pump pulse) induces a change in the sample that can be probed by a delayed second laser pulse

(probe pulse). A change of the delay between the pulses provides the time resolution of the induced excitation. The experimental setup is shown in Fig. 3.5.

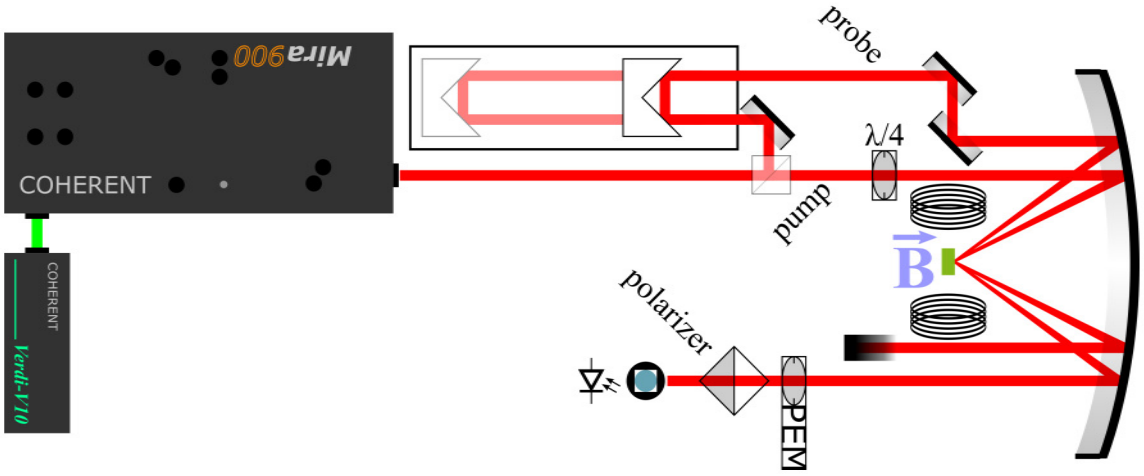

Figure 3.5 Setup for the time-resolved measurement of the magneto-optical Kerr effect. Upon reflection from a magnetized sample, the linearly polarized probe beam experiences a rotation of the plane of polarization. A photoelastic modulator (PEM) in conjunction with a linear polarizer translates this rotation into an intensity modulation. The intensity is detected by a photodiode and its modulation is analyzed by a lock-in amplifier. For time-integrated measurements, the pump-beam is blocked.

In the case of pump-probe Kerr rotation, the pump pulse is circularly polarized, so that it induces a spin orientation (i.e. magnetization). Upon reflection, the linearly polarized probe pulse experiences a rotation of the polarization plane that can be detected as described above, giving a measure for the spin orientation in the sample. In this scheme, the spins are oriented along the axis of light propagation. The application of a magnetic field in Voigt geometry, i.e. perpendicular to the light propagation axis, induces a precession of the spin about the magnetic field axis with the Larmor precession frequency Ω_L, see Eq. (2.28). As the magnetization changes accordingly, the precession can be detected as an oscillation in the pump-probe Kerr signal. With a measurment of the magnetic field dependence of the Larmor frequency $\Omega_\mathrm{L}(B)$, the absolute value of the Landé factor g of the respective charge carrier can be determined. A potential intercept when plotting $\Omega_\mathrm{L}(B)$ (extrapolated value for $\Omega_\mathrm{L}(B = 0) \neq 0$ from linear fit) results from a zero-field splitting of the spin states coupled by an external magnetic field in Voigt geometry.

3.4 Four-Wave-Mixing spectroscopy

The response of condensed matter to an illumination with an electromagnetic field is described by the polarization. A power series expansion of the polarization P in

the electric field E reads

$$\begin{aligned} P_i(\boldsymbol{r},t)/\epsilon_0 = &\sum_j \chi^{(1)}_{ij}(\boldsymbol{r},t) * E_j(\boldsymbol{r},t) \\ &+ \sum_{jk} \chi^{(2)}_{ijk}(\boldsymbol{r},t) * E_j(\boldsymbol{r},t) * E_k(\boldsymbol{r},t) \\ &+ \sum_{jkl} \chi^{(3)}_{ijkl}(\boldsymbol{r},t) * E_j(\boldsymbol{r},t) * E_k(\boldsymbol{r},t) * E_l(\boldsymbol{r},t) \\ &+ \mathcal{O}(E^4). \end{aligned} \tag{3.3}$$

The indices i, j, k, l denote spatial coordinates and ϵ_0 is the vacuum permittivity. The optical susceptibilities χ classify phenomena as linear (governed by $\chi^{(1)}$) or non-linear (governed by $\chi^{(>1)}$). The magnitude of χ is a material property and strongly dependent on crystal symmetries.

The term four-wave-mixing (FWM) denotes a phenomenon that is governed by $\chi^{(3)}$. Generally, three electromagnetic fields interact with the medium and produce a third-order nonlinear polarization which is the source of a fourth electromagnetic wave. Hence this process is called four-wave-mixing. In the simplified case of instantaneous, local action, the third order polarization reads

$$P^{(3)}(\boldsymbol{r},t) \propto \chi^{(3)} \cdot E_1(\boldsymbol{r},t) \cdot E_2(\boldsymbol{r},t) \cdot E_3(\boldsymbol{r},t). \tag{3.4}$$

The frequency and direction of the fourth wave created by this nonlinear polarization depend on the geometry of the incident waves E_1, E_2, E_3. With the assumption of plane waves $E_n = \hat{E}_n \exp(\mathrm{i}\omega_n t - \mathrm{i}\boldsymbol{k}_n\boldsymbol{r}) + c.c.$, with $n = 1,\ 2,\ 3$, the multiplication in (3.4) leads to mixing terms that contain, e.g., a frequency $\nu_4 = -\nu_1 + \nu_2 + \nu_3$ and a direction $\boldsymbol{k}_4 = -\boldsymbol{k}_1 + \boldsymbol{k}_2 + \boldsymbol{k}_3$.

In the case of *degenerate* four-wave-mixing the direction and frequency of two or more of the involved waves can be the same. This is the case in the experiments discussed in Chap. 6, where the geometry was chosen such that $E_3 = E_2$. Hence the properties of the FWM signal are

$$\nu_{\mathrm{FWM}} = 2\nu_2 - \nu_1 \tag{3.5}$$

$$\boldsymbol{k}_{\mathrm{FWM}} = 2\boldsymbol{k}_2 - \boldsymbol{k}_1 \tag{3.6}$$

$$P^{(3)}_{\mathrm{FWM}} \propto \chi^{(3)} \hat{E}_1^* \hat{E}_2^2. \tag{3.7}$$

In Fig. 3.6 this situation is sketched for reflection geometry. It is important to note here that the FWM signal is emitted in a background-free direction, see Eq. (3.6) and Fig. 3.6, and that the nonlinear polarization depends on the field amplitudes of the generating waves, rather than on their intensities.

Since in the realization of the photon echo, the electric fields of the exciting beams are decisive and not their intensities, the optical polarization can be important.

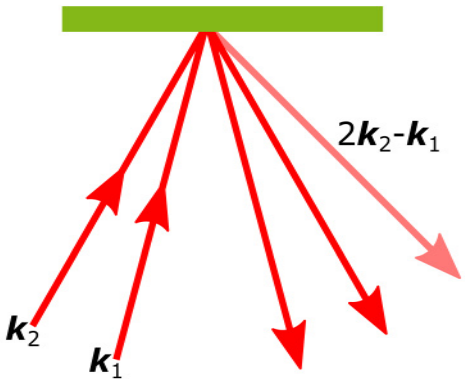

Figure 3.6 Generation of an additional beam by degenerate four-wave-mixing. Apart from the reflections of the generating beams incident under $\boldsymbol{k}_1$ and $\boldsymbol{k}_2$, the four-wave-mixing signal being emitted in the background-free direction $2\boldsymbol{k}_2 - \boldsymbol{k}_1$ is shown.

Indeed, the optical selection rules (see Subsec. 2.2.5) determine which states and transitions are involved in the generation of the echo. These states can exhibit very different dependence on various parameters. However, the optical polarization of the echo is generally identical to the polarization of the first excitation pulse [186].

3.4.1 Optical setup

The optical setup for the detection of four-wave-mixing signals is shown in Fig. 3.7. The single beam that is emitted from the mode-locked Titanium-Sapphire-laser Coherent Mira 900 (compare 3.2) is divided into four beams. Three of them are used to excite the sample and produce a four-wave-mixing signal, the fourth beam is used as a reference for heterodyne detection (see Subsec. 3.4.2).

A crucial ingredient for this detection scheme is the information and control of the relevant frequencies. To this end, two acousto-optical modulators (AOM) from IntraAction are used to imprint specified frequencies to Beam 1 and the reference beam. The working principle is as follows: using the piezoelectric effect, a high-frequency voltage excites a traveling ultrasound wave in a transparent medium (here: flint glass) inside the AOM. Thereby a periodic fluctuation of the material density is created that causes spatial oscillations of the refractive index, which act as an optical grating. Consequently, an incident light beam is diffracted and experiences a shift of its optical frequency due to the Doppler effect. The frequency shift can be varied from 30 MHz to 50 MHz. The sign of the shift depends on the direction of the diffraction relative to the direction of propagation of the ultrasound wave.

For the following description, the excitation beams are identified with numbers, representing the sequence of arrival at the sample in a typical photon echo experiment (see 2.2.4).

The control of the arrival time of pulses is achieved by the use of delay lines, that

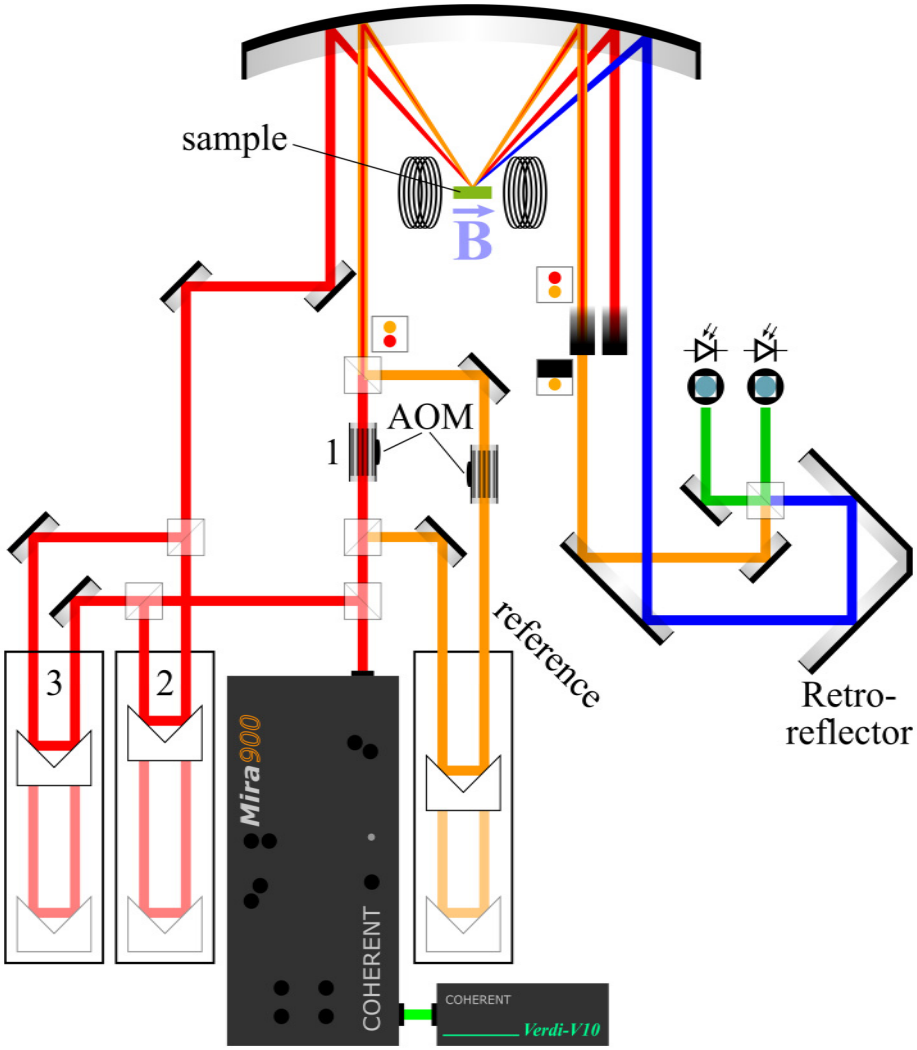

Figure 3.7 Optical setup for four-wave-mixing spectroscopy. The beam of the picosecond laser is split into four beams. Three of them are used for excitation (red) and the fourth (orange) serves as a reference. All beams are focused on the sample by a spherical mirror, which also collects the reflections of all beams as well as the four-wave-mixing signal (blue). For the detection, the excitation beams are blocked. Beam 1 and the reference beam are aligned with a small vertical shift, so that a selective blocking can be ensured. The four-wave-mixing signal and the reference beam are superimposed using an interferometer and detected by balanced photodiodes. The detection scheme is explained in detail in Subsec. 3.4.2.
A magnetic field can be applied parallel to the sample surface with an electromagnet. The figure shows the setup in the configuration for the stimulated photon echo. For the measurement of spontaneous photon echoes, the leftmost beam is blocked. The different colors for the beams are only for illustration and are no indication for the optical wavelength.

mechanically shift a retroreflector and thereby increase the traveling distance of a light pulse and thereby delay a pulse in time. For the experiments presented in Chap. 6, three delay lines OWIS LIMES were used, two with a length of 25 cm and one with a length of 15 cm. Thereby, respective maximum delays for the pulses of about 1.7 ns and 1.0 ns are possible. The delay lines can be moved with a resolution of 0.3 µm, corresponding to 2 fs. Since this is considerably smaller than the duration $\tau_p \approx 2\,\mathrm{ps}$ of the optical pulses, the delay line does not deteriorate the overall time resolution of the setup.

The path of Beam 1 does not contain a delay line, so the time of arrival is fixed. It is, however, passed through an AOM that shifts the optical frequency by 42 MHz and that is operated at a frequency of 1 kHz, imprinting an additional intensity-modulation. Apart from different delay lines, allowing for individual retardation, beams 2 and 3 share the exact same path. Acousto-optical modulators are not introduced in their paths, so that the optical frequencies $\nu_2 = \nu_3 = \nu_{\mathrm{laser}}$ remain unchanged.

For the reference beam, an individual delay line is used to control the time of arrival independently. The optical frequency is shifted to $\nu_{\mathrm{ref}} = \nu_{\mathrm{laser}} - 41.01\,\mathrm{MHz}$ by using an acousto-optical modulator that is continuously operated (no additional modulation of the intensity). The opposite sign of the shift as compared to Beam 1 is achieved by utilizing the opposite order of diffraction.

All beams are directed to a spherical mirror with a radius (and focal length) of 40 cm, which focuses the beams in the plane of the sample. While the beams 1, 2 and 3 are all absolutely parallel and thus focused in the same spot, the reference beam is aligned such that it is focused with a small vertical shift. The size of the shift is approximately 200 µm – about the same size as the beam diameter.

The reflections of all beams, as well as the four-wave-mixing signal are collected by the same mirror and are again parallelized. Beam dumps block all beams except for the reference and the FWM signal. For the detection, the FWM signal and the reference beam are superimposed in an interferometer and focused on balanced photodiodes. The functional principle of the detection is further specified in the next subsection.

3.4.2 Optical heterodyne detection and signal recovery

Optical heterodyne detection is an interferometric technique of signal processing. It relies on nonlinear mixing of the oscillating signal with a reference of nearby frequency. The beat (more precisely: the difference frequency) that results from this mixing exhibits the same properties as the signal of interest but is generally easier to detect and process.

For the experiments discussed in Chap. 6, the signal of interest is of course the optical FWM signal. The reference beam passes the same optical elements as the other beams and does not interact with any other beam or an induced polarization.

According to (3.6), the optical frequency of the FWM signal is given by

$$\begin{aligned}\nu_{\mathrm{FWM}} &= 2\nu_{\mathrm{laser}} - (\nu_{\mathrm{laser}} + 42.00\,\mathrm{MHz}) \\ &= \nu_{\mathrm{laser}} - 42.00\,\mathrm{MHz}.\end{aligned} \tag{3.8}$$

Because of the intensity modulation of Beam 2 at f_{mod}, the intensity of the FMW-signal is also modulated at the same frequency.

The FWM signal and the reference beam, which was frequency-shifted to $\nu_{\mathrm{ref}} = \nu_{\mathrm{laser}} - 41.01\,\mathrm{MHz}$, are superimposed using an interferometer and focused on two photodiodes.

The mixing (i.e. interference) with the reference beam gives rise to a beat at frequency

$$\begin{aligned}\nu_{\mathrm{signal}} &= \nu_{\mathrm{ref}} - \nu_{\mathrm{FWM}} \\ &= \nu_{\mathrm{laser}} - 41.01\,\mathrm{MHz} - (\nu_{\mathrm{laser}} - 42.00\,\mathrm{MHz}) \\ &= 0.99\,\mathrm{MHz}.\end{aligned} \tag{3.9}$$

This frequency can easily be processed electronically and is immune against influences from stray light, mechanical vibrations and other environmental instabilities. The intensity modulation at $f_{\mathrm{mod}} = 1\,\mathrm{kHz}$ is preserved and can be understood as the envelope of the signal. The electronic signal is transferred to a lock-in amplifier that is provided with the beat frequency of $\nu_{\mathrm{signal}} = 990\,\mathrm{kHz}$ by the power supply of the AOMs. The time constant of the lock-in amplifier is set to 100 µs, corresponding to a bandwidth of 10 kHz. The modulation of the signal at $f_{\mathrm{mod}} = 1\,\mathrm{kHz}$ is therefore not damped by the lock-in amplifier.
In order to achieve an even better signal-to-noise ratio, the output of the lock-in amplifier is connected to a second lock-in amplifier which is adjusted to $f_{\mathrm{mod}} = 1\,\mathrm{kHz}$. The signal detected by this second lock-in amplifier is transferred to a LabView script run on a desktop computer.

3.4.3 Principle of measurement

In order to detect the dynamics of the four-wave-mixing signals and the photon echo, the laser pulses have to be delayed with respect to each other. This is achieved by introducing detours into the paths of the beams. Depending on the parameters that are to be accessed, different scanning routines can be implemented. Figure 3.8 gives an overview of the pulse sequence.

Reference scan

Moving (only) the reference delay line results in a changed overlap of the FWM signal and the reference beam. The step size can be chosen such that it is shorter than the dephasing time and the laser pulse duration. In that way, the temporal profile of the FWM signal, more particularly the photon echo, can be resolved.

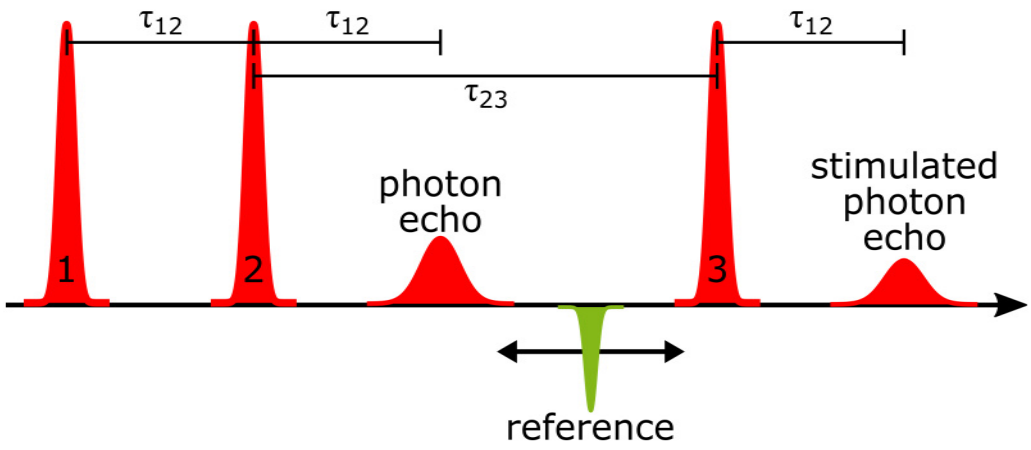

Figure 3.8 Sequence of laser pulses and photon echo occurrence in a (stimulated) photon echo experiment. The time delays τ_{12} and τ_{23} between the excitation pulses can be controlled independently. Furthermore, the independent delay of the reference pulse (green) grants access to multiple scanning routines.

τ_{12} scan

It is possible to measure the decay constant of the photon echo in the following way: for different delays between the first and second pulse, the echo profile is scanned in the way described in the previous paragraph. All the peak intensities of the resulting curves are then plotted against the respective delay time. A decay function can be fitted to the resulting curve, allowing the extraction of the time constant. This procedure is however very time-consuming and produces a lot of data that is not actually needed, since only the maximum signal intensity of the photon echo is of interest. Hence the amount of data and the required amount of time can be decreased by recording data only at the exact time of photon echo occurrence. For this purpose, the delay lines for the reference beam and for the second beam are moved in parallel. Since the delay of the second beam determines the time τ_{12} and the reference pulse has to arrive at time $\tau_{\text{ref}} = 2\tau_{12}$, the step for the reference beam delay has to be set to twice the size as the step of the second beam delay.

τ_{23} scan

For the case of the stimulated echo, the dependence on two different time delays can be studied. In addition to the time delay between the first and the second beam that is investigated as described in the previous paragraph, the dependence on the time delay of the third beam is of interest. Therefor the time delay between the first and the second beam (τ_{12}) is set to a fixed value.

For the case of the stimulated photon echo, an additional mode of measurement is required in order to investigate the dependence on Beam 3. In this case, the echo

signal is expected at time $t = 2 \cdot \tau_{12} + \tau_{23}$. For recording the echo amplitude, the reference beam is set to the time of echo occurrence. The delay line for Beam 3 and for the reference beam are moved in parallel and with equal step sizes.

The scan protocols mentioned before can be employed for the investigation of the stimulated photon echo as well.

4 Resonant optical orientation of Mn^{2+} spins in bulk CdMnTe

One of the most extensively studied semiconductor materials is cadmium telluride (CdTe). The increasing application of CdTe as a solar cell material hints at its industrial significance but fast progress is inhibited by intrinsic difficulties in material preparation and lack of structural material knowledge [187].

For spintronic applications, the diluted magnetic semiconductor CdMnTe offers a large versatility due to the high Mn contents of up to 77 % that are achievable without loss of crystallographic structure [134]. The flexibility in Manganese concentration allows an abundance of different magnetic behaviors (see paragraph "CdMnTe" in Subsec. 2.3.1 and [137, 188]). In any case, the five electrons of the outer 3*d* shell of the Mn^{2+} ion represent an optically active magnetic center [130, 132, 189].

The ion can be excited either directly [149] or via energy transfer from optically excited electron-hole pairs and excitons [190, 191]. The relaxation into the ground state is accompanied by intracenter photoluminescence with characteristic photon energies around 2.0 eV and decay times of several tens of microseconds [192, 193]. The optical control of Mn spins via optically excited and oriented charge carriers was demonstrated in CdTe quantum dots [194, 195]. This was achieved by exploiting the exchange interaction between electron-hole pairs and the Mn ions. A direct optical optical control of the Mn spins has not yet been reported.

This chapter presents the resonant optical orientation and alignment of Mn^{2+} spins in the $Cd_{1-x}Mn_xTe$ crystals described in 3.1.1. The spin orientation and alignment is evidenced optically by the circular and linear polarization of photoluminescence, respectively. Part of the results discussed in this chapter are published in [196].

4.1 Time-integrated studies

Figure 4.1 shows the photoluminescence spectra of CdMnTe crystals with different Mn content. The high-energy peak is attributed to the free exciton and experiences a blue shift with rising Mn concentration as the recombination energy follows the band gap of $Cd_{1-x}Mn_xTe$ [134]. For $x = 0.45$, the exciton recombination is expected at about 2.31 eV [180, 197], but not observed. This is due to the fact that for manganese concentrations higher than $x = 0.4$, the excitation of the Mn^{2+} intra-ion transition is energetically favored compared to the excitation of an exciton [130].

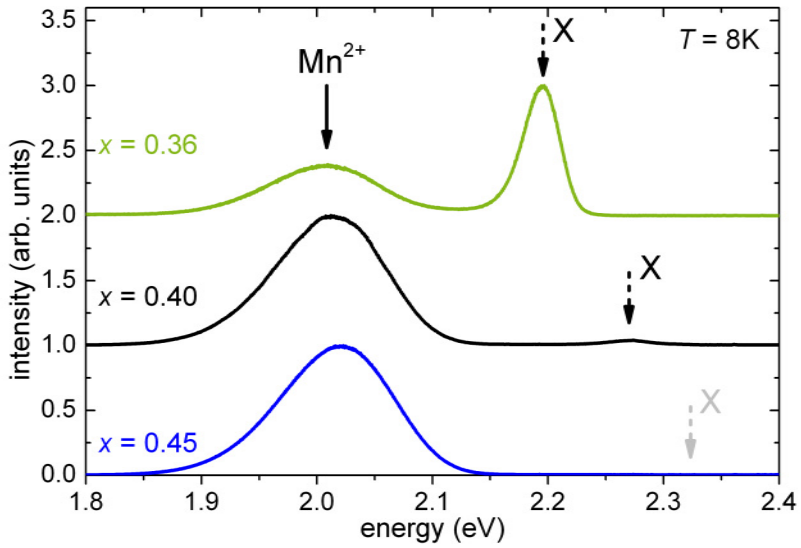

Figure 4.1 Photoluminescence spectra of $Cd_{1-x}Mn_xTe$ for different Mn concentrations x. Independent from the manganese amount, the intra-ion transition of Mn^{2+} (solid arrows) can be observed at about 2 eV. The recombination of the exciton (X, dashed arrows) shifts to higher energies with rising manganese concentration. For a manganese percentage of $x \geq 45\,\%$ it is not observed. The spectra were recorded for continuous-wave excitation at $E_{\mathrm{exc}} = 3.06\,\mathrm{eV} (\lambda_{\mathrm{exc}} = 405\,\mathrm{nm})$, normalized, and shifted by 1 for better readability.

The low-energy peak is attributed to the Mn^{2+} intracenter transition. The spectral position of this peak is the same for all studied Mn concentrations. As discussed in the paragraph "CdMnTe" of Subsec. 2.3.1, the fundamental optical transition in Mn^{2+} ions is generally accepted to involve the ${}^6A_1$ ground state and the ${}^4T_1$ excited state.

This transition is further studied by photoluminescence spectroscopy. The variation of the excitation wavelength causes a spectral shift of the peak intensity as shown in Fig. 4.2 for the sample with $x = 0.45$. The reason for the shift is the inhomogeneous broadening induced by the Jahn-Teller distortion of the crystal field. At an excitation wavelength of 570 nm (2.175 eV), the peak of the photoluminescence is observed at 1.996 eV, which is the minimal value. This condition is hence identified as the resonant excitation of the Mn^{2+} intracenter transition.
Accordingly, a sizeable Stokes shift of about 0.2 eV is observed, caused by excitation energy transfer among manganese ions and electron-lattice interaction (Franck-Condon principle). The observation of a Stokes shift of this order is typical for II-VI crystals [132, 193, 198, 199].

For the same excitation energies, the intensity of the photoluminescence and the degrees of circular (ρ_c, see eq. (3.1)) and linear (ρ_l, see eq. (3.2)) polarization were measured. The results are shown in Fig. 4.3.

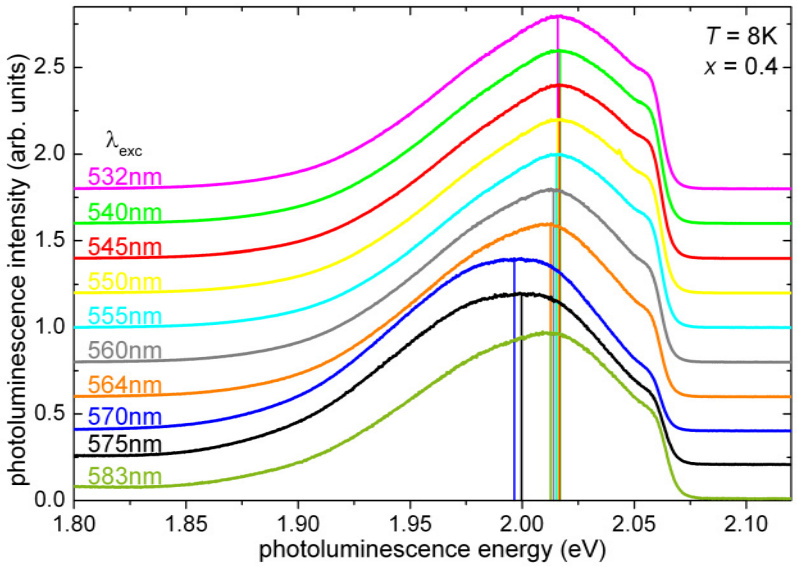

Figure 4.2 Photoluminescence spectra of the Mn^{2+} intra-ion transition for different excitation wavelengths. The vertical lines mark the positions of the intensity maxima for the respective curves. The intensity peak is shifted by ca. −40 meV for an excitation wavelength of 570 nm (2.175 eV). The different shape of the spectra as compared to Fig. 4.1 is due to the application of a long-pass filter with a cut-on wavelength of 600 nm (2.066 eV) that suppresses stray light of the laser.

The PLE spectrum shows a steep increase in photoluminescence intensity when the photon energy exceeds the resonance at 2.175 eV (570 nm). Furthermore, the photoluminescence from the intracenter transition exhibits a degree of polarization of about 8 %, both circular (green circles) and linear (blue triangles), for resonant excitation.

The PLE spectra of all three studied samples (see Subsec. 3.1.1) show the same behavior and exhibit no correlation with the optical generation of excitons. The optically induced polarization is therefore attributed to the resonant excitation of Mn^{2+} ions.

The circular polarization of the photoluminescence evidences the optical orientation of Mn spins along the light propagation axis $\boldsymbol{z} \parallel [110]$. When the polarization of the excitation is reversed from σ^+ to σ^-, the polarization of the photoluminescence changes accordingly $\rho_c^+ = -\rho_c^-$.

The linear polarization signifies the optical alignment of Mn spins in the x-y-plane. When the direction of linear polarization of the excitation is changed from $\boldsymbol{x} \parallel [001]$ to $\boldsymbol{y} \parallel [1\bar{1}0]$, the polarization of the photoluminescence changes accordingly $\rho_l^x = -\rho_l^y$. Moreover, the magnitude of optical alignment is independent from the direction of linear polarization, so that $\rho_l^x \approx \rho_l^{x'}$, excluding a noteworthy anisotropy for the observed effect.

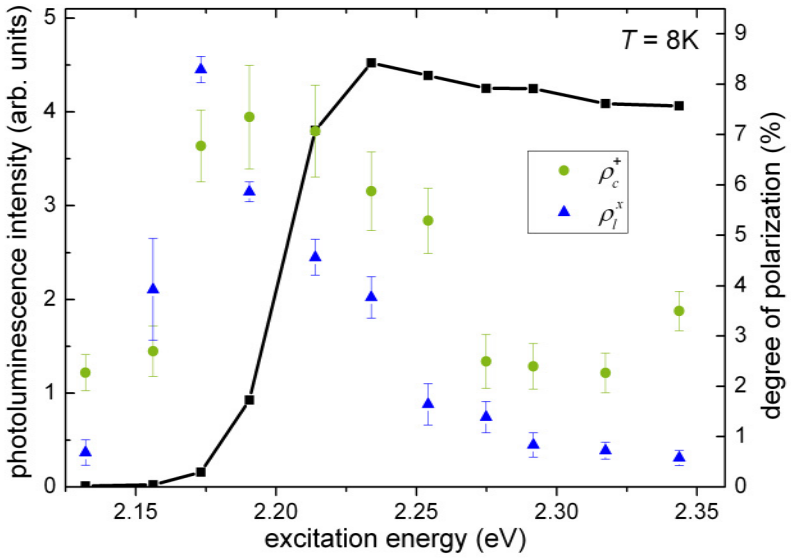

Figure 4.3 Photoluminescence excitation spectra in $Cd_{0.55}Mn_{0.45}Te$. Dependence of the Mn^{2+} intra-ion photoluminescence intensity (black line, left axis) and the circular and linear polarization degrees (circles and triangles, right axis) on the excitation energy.

4.2 Time dependence

The dynamics of the effect can be monitored using time resolved photoluminescence spectroscopy. The excitation was implemented with an electro-optical modulator modulating the beam of a picosecond laser (2 ps pulse length, 76 MHz repetition rate) and thereby producing 5 µs-long trains of pulses at a repetition period of 100 µs.

The decay of the total photoluminescence intensity $I(t) = I_+ + I_- = I_x + I_y \propto \exp(-t/\tau)$ is defined by the lifetime τ of the Mn^{2+} excited state. The spin dynamics, including the spin relaxation time, of the optically oriented or aligned spins can be determined by the polarization transients.

In Fig. 4.4 the transients of the photoluminescence intensity (top panel) and the degree of polarization (bottom panel) are shown for the sample with a manganese fraction of $x = 0.40$ and for an excitation energy of $\hbar\omega_{\mathrm{exc}} = 2.175\,\mathrm{eV}$.

From the transient of the intensity, a lifetime of $\tau = 23\,\mu\mathrm{s}$ can be extracted. This is in good agreement with previous measurements [193, 200].

The transient of circular polarization (Fig. 4.4, green circles in bottom panel) is characterized by a plateau at about 8 % polarization. This indicates that the spin relaxation time is much longer than the time range of the scan, which is about 100 µs. A lower bound of 1 ms for the spin relaxation time can be given nevertheless.

The transient of linear polarization (Fig. 4.4, blue triangles in bottom panel) exhibits a fast initial decay, followed by a plateau. The time constant of the initial decay is defined by the apparatus function and can therefore not be resolved.

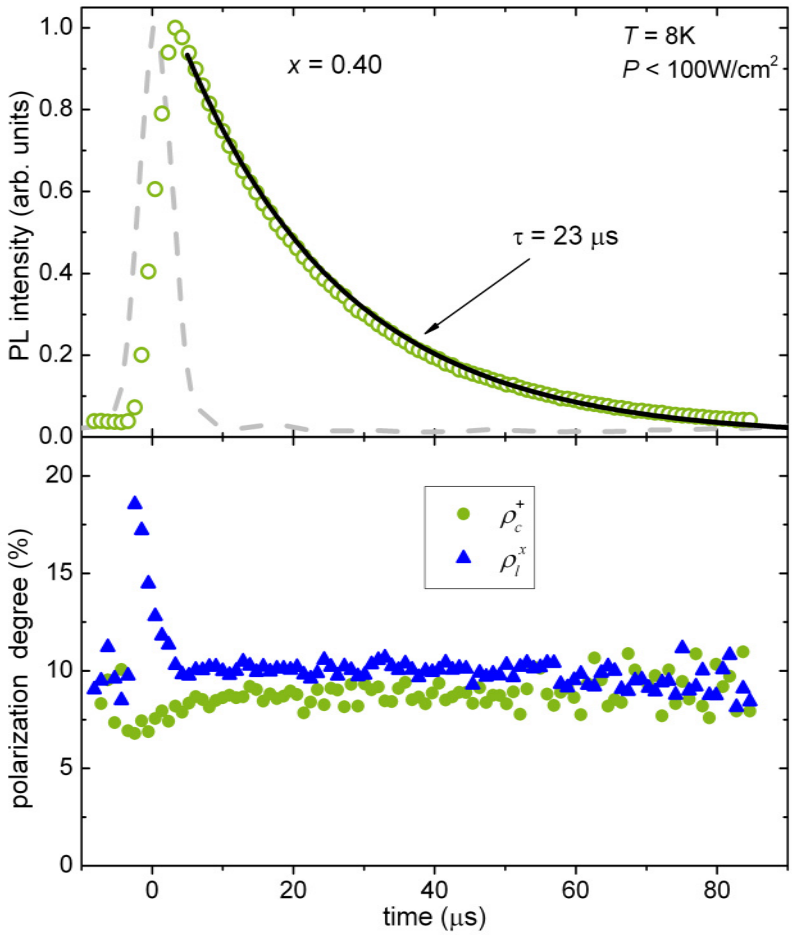

Figure 4.4 Time-resolved photoluminescence data for the sample with $x = 0.40$ at an excitation energy of 2.175 eV. The decay of the photoluminescence intensity (open circles, top panel) is fitted with a monoexponential function (black curve) revealing a decay time of $\tau = 23\,\mu s$. The dashed line is the apparatus function. The bottom panel contains the dynamics of the circular ρ_c (green circles) and linear ρ_l (blue triangles) degrees of polarization

4.3 Role of the spin glass phase

The intra-ion transition of Mn^{2+} in $Cd_{1-x}Mn_xTe$ is only observable for manganese contents of $x = 0.4$ or higher [151, 152]. At the same time, manganese contents of above $x = 0.17$ [141, 142] lead to the development of the spin glass phase in CdMnTe (see paragraph "CdMnTe" in Subsec. 2.3.1, [140, 147]). Accordingly, the studied sample is expected to exhibit spin glass behavior. The long-range interaction leads to reduced fluctuations of the Mn^{2+} spins. This in turn leads to reduced spin relaxation (see Subsec. 2.2.6) and thereby to enhanced spin polarization which is detected by the polarization of photoluminescence. It is therefore instructive to

study the influence of the spin glass phase on the observed optical polarization displayed in Fig. 4.3.

4.3.1 Temperature dependence

A characteristic feature of the spin glass phase is the associated transition temperature [140, 147] . With increasing temperature, the fluctuations of the Mn^{2+} spins should also increase, enhancing the spin relaxation and decreasing the observed polarization.

In order to test this, the ambient temperature (i.e. lattice temperature) of the sample was set to different values below 35 K and the degree of circular polarization was measured. The results are shown in Fig. 4.5.

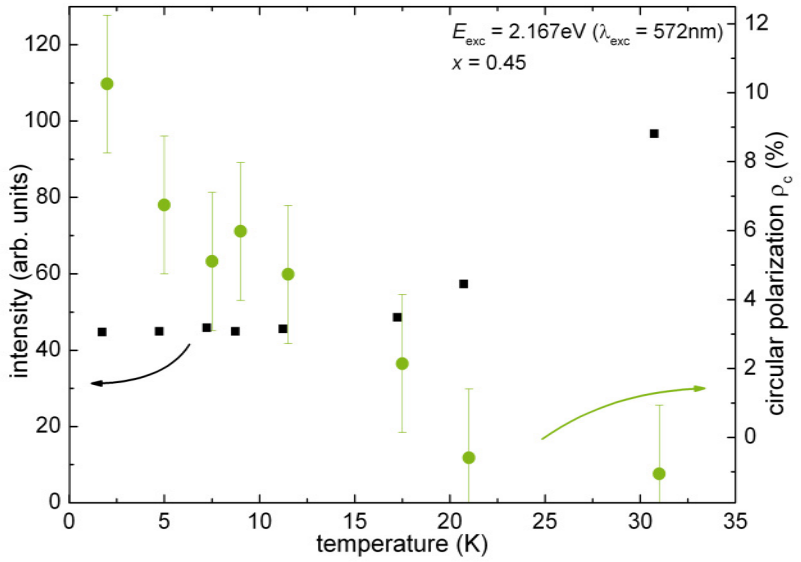

Figure 4.5 Temperature dependence of the photoluminescence from the Mn^{2+} intra-ion transition. The polarization decreases with increasing temperature and reaches zero at the transition temperature T_{sg} of the spin glass phase.

Indeed, the degree of circular polarization decreases with rising temperature. Furthermore, for temperatures above the spin glass transition temperature T_{sg} the polarization vanishes entirely. This suggests that the spin glass phase plays a crucial role for the observed polarization of the photoluminescence from the Mn^{2+} intra-ion transition.

4.3.2 Power dependence

The spin orientation of the Mn^{2+} ions in the spin glass phase is frozen randomly, but the optical excitation with polarized light defines a preferred direction for spin ori-

entation. This leads to the conjecture that an optical manipulation and orientation of the spin glass could be possible. This would lead to even stronger suppression of the spin relaxation and consequently to a higher degree of polarization. The effect would depend strongly on the number density of optically oriented charge carriers and hence on excitation power density. The power dependence of the degree of circular polarization was measured with a constant excitation spot size.

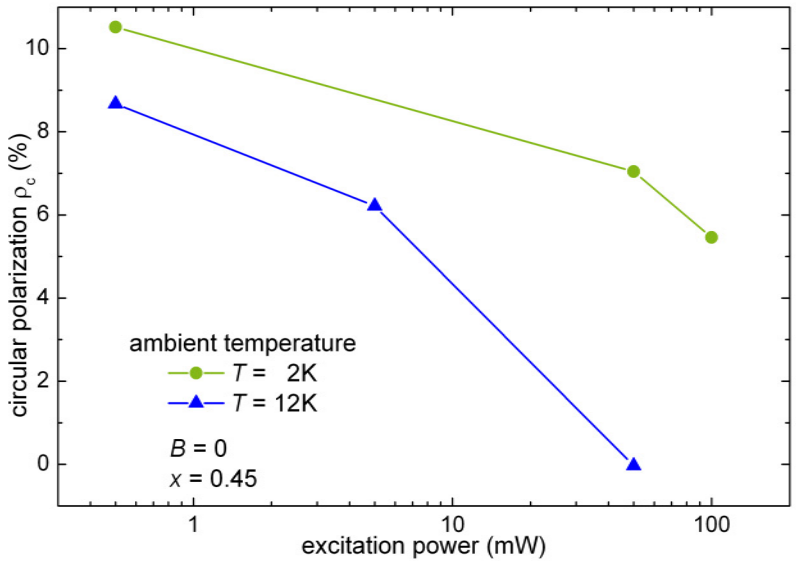

Figure 4.6 Excitation power dependence of the degree of circular polarization of the photoluminescence from the Mn^{2+} intra-ion transition. For rising excitation power, the degree of polarization decreases. The measurement was repeated for ambient temperatures of $T = 2\,\mathrm{K}$ (green circles) and $T = 12\,\mathrm{K}$ (blue triangles).

The results are shown in Fig. 4.6, where it can be seen clearly that there is no increase in polarization with rising excitation power density. On the contrary, the polarization decreases significantly for increasing power. This is attributed to the increased heat input for higher excitation powers, which has the same effect as an increase in ambient temperature as discussed in Subsec. 4.3.1.

4.3.3 Comparison with ZnMnSe

In order to determine the influence of the spin glass phase on the spin polarization of Mn^{2+} ions, it would be instructive to compare with a sample showing no spin glass phase. As already discussed in Subsec. 3.1.1, this is not possible in CdMnTe since the Mn^{2+} intra-ion transition can only be studied when the Mn content exceeds the threshold for the formation of the spin glass phase.

For the observation of the intra-ion transition in absence of a spin glass phase, a different material has to be investigated. In zinc selenide (ZnSe), the exciton

resonance is at 2.8 eV and considerably larger than the Mn^{2+} transition. Hence even for small Mn concentrations, the Mn^{2+} ions can be addressed directly. Additionally, being a II-VI semiconductor, in ZnSe the Mn ions assume the same configuration as in CdTe and form isoelectronic magnetic centers.

Albeit slightly shifted in energy, the optical orientation of the same intra-ion transition ($^6A_1 \rightarrow {}^4T_1$) can be studied in ZnSe and directly compared to the behavior in CdTe. The optical orientation under resonant excitation is shown in Fig. 4.7 for external magnetic fields between zero and 3 T.

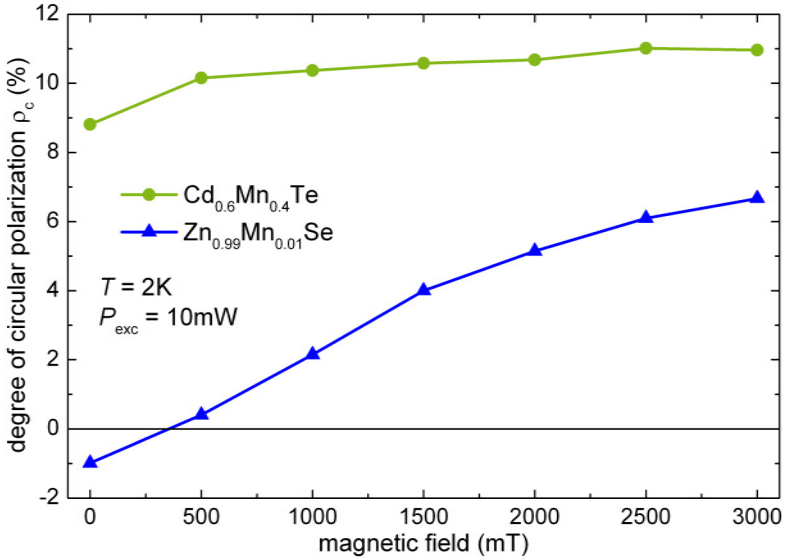

Figure 4.7 Magnetic field dependence of the degree of circular polarization in ZnMnSe. For small external fields, the polarization is close to zero. Only for considerable field strenghts of $B \leq 3\,\mathrm{T}$, a polarization can be observed that is always smaller than the minimal polarization observed in the CdMnTe sample.

In the ZnMnTe sample, there is less than one percent polarization, $|\rho_c| < 1\,\%$ for field strengths of $|B| \leq 500\,\mathrm{mT}$. For higher fields, the degree of circular polarization rises markedly, reaching close to 7 % for $B = 3\,\mathrm{T}$ (blue triangles in Fig. 4.7). For the CdMnTe sample (green circles in Fig. 4.7), the increase of polarization with magnetic field is only minor throughout the entire range. The value of ρ_c, however, is generally higher than for the ZnSe sample. In fact, in the sample with spin glass properties, the polarization exceeds 8 % already at zero field.

This behavior can be interpreted as follows: the observation of optical orientation requires the suppression of spin relaxation. This can be achieved in different ways. For the CdTe sample, the spin relaxation is suppressed by the reduction of fluctuating fields due to the spin glass phase. The spin glass is robust against external magnetic fields and is present also for zero external field. In ZnMnSe, a sizeable polarization can only be observed for magnetic fields of $B \geq 1\,\mathrm{T}$. For zero field, the

polarization is zero, confirming the necessity of spin glass.

For stronger magnetic fields, a spin polarization can also be observed in the paramagnetic ZnMnSe. This can be caused by a suppression of the spin relaxation due to the Zeeman energy barrier for spin flips. To resolve the underlying effect, it would be necessary to investigate the time-resolved photoluminescence of the Mn^{2+} transition in ZnMnTe. For the statement that the spin glass phase of the sample is crucial for the observation of optical orientation, the finding that there is no spin polarization in ZnMnSe for $B = 0$ is sufficient.

4.4 Theoretical modeling

In an isolated Mn^{2+} ion, inner d–d transitions are forbidden by spin and parity selection rules. In the crystal environment, this restraint is partly lifted due to different effects, including the crystal field, hybridization of Mn d-states with the chalcogenide p-states [132], and spin orbit interaction. Hence the transition can be observed. In the following, a simple model is used to estimate the polarization of the intracenter photoluminescence, taking into account only the effect of spin orbit interaction. Furthermore, spherical symmetry is assumed to model the intracenter transitions with selection rules for electric-dipole transitions in one-particle approximation using the total angular momentum formalism.

The ${}^6A_1$ ground state of Mn^{2+} is characterized by total spin $S = 5/2$ and total orbital momentum $L = 0$. It is therefore treated as a spherically symmetric state with a total angular momentum of $j = 5/2$.
The ${}^4T_1$ excited state (see paragraph "CdMnTe" in Subsec. 2.3.1) is characterized by total spin $S = 3/2$. Due to the symmetry properties of this orbital state T_1 (also represented as Γ_4 [153, 154]), it can be associated with an effective total orbital momentum of $L_{\text{eff}} = 1$. The total orbital momentum of the excited state of the system can hence take values of $j' = 1/2, 3/2, 5/2$. Within the electric dipole approximation, the selection rules only allow transitions with $j \to j' = j$ or $j \to j' = j \pm 1$. Since $j = 5/2$, the state with $j' = 1/2$ is out of consideration and only the transition matrix elements for the states with $j' = 3/2$ and $j' = 5/2$ need to be calculated.

The probability of a transition is proportional to the square of the absolute value of the transition matrix element. For the calculation of photoluminescence polarization only the ratios of the matrix elements are relevant, not their individual values.

With the aforementioned approximations, the Wigner-Eckart theorem can be exploited to decompose the different transition matrix elements into a single mutual reduced matrix element, multiplied by individual Clebsch-Gordan coefficients. These can be calculated with the formulas from the pertinent literature (see, e.g. [201]).

The allowed transitions between the $j = 5/2$ ground state and the $j' = 3/2$ and $j' = 5/2$ excited states for right-handed circular polarized light and their transition probabilities are depicted in Fig. 4.8.

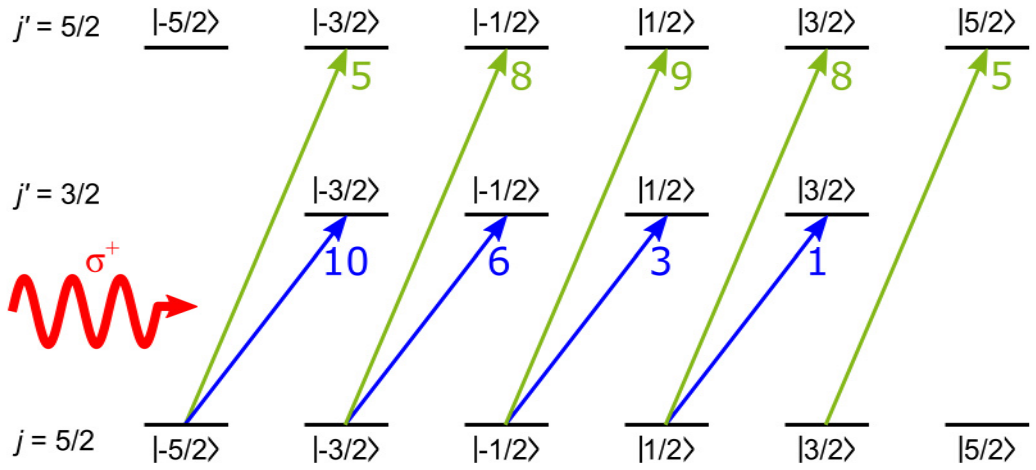

Figure 4.8 Selection rules for Mn^{2+} under right-handed circularly polarized excitation. The arrows correspond to the dipole-allowed transitions from the ground states to the excited states of the Mn^{2+} ion. The relative intensity of the transitions is shown next to the corresponding arrows.

From the inequalities of the transition probabilities results an unequal occupation of the excited substates and a nonzero polarization of the photoluminescence. From the calculated transition probabilities, degrees of polarization of 44.55 % and 7.25 % follow for recombination from the excited states with $j' = 3/2$ and $j' = 5/2$, respectively. Assuming that both excited states share the same reduced matrix element, an overall polarization of 22.17 % is expected. This is nearly three times higher than observed in experiment.
In the above discussion of the allowed transitions, spin depolarization was disregarded. Indeed, as the almost constant polarization in the lower panel of Fig. 4.4 shows, the spin depolarization is suppressed. However, Fig. 4.4 also shows a very fast decay of the linear polarization immediately after the excitation - for the circular polarization it even seems to be too fast to be resolved.

The large Stokes shift of about 0.2 eV evidences a considerable energy relaxation of the excited state prior to the emission of photoluminescence. The spin depolarization can occur during this relaxation via one or both of the following underlying mechanisms. (i) An electron-phonon interaction changes the configuration of the *d*-orbital electrons and the Mn ions [202]. This locally reduces the atomic potential energy, which, in turn, induces a reduction of the recombination energy from the excited state. It also leads to a modulation of the spin-orbit interaction of the electrons, inducing a spin flip and thereby a reduction of the photoluminescence polarization. (ii) Excitation energy is transferred among manganese ions. Since the spins of neighboring manganese ions are not parallel to each other, this process can also reduce the spin orientation and alignment. By the additional emission of a phonon, this process can also provide a Stokes shift.

In order to describe the temporal behavior of the signal, a three-level system is considered. It is sketched in Fig. 4.9 and comprises a ground state $|0\rangle$, an excited state $|1\rangle$ and a radiative state $|2\rangle$. These correspond to the resonances observed in experiment. The transition $|0\rangle \rightarrow |1\rangle$ denotes the resonant excitation of the Mn^{2+} intra-ion transition at 2.175 eV (570 nm), while the transition $|2\rangle \rightarrow |0\rangle$ corresponds to the emission of the photoluminescence at 2.0 eV (620 nm).
In general, the entire system of interacting Mn spins has to be considered for the excited state. In the scope of the model, the description of the excited state is limited to parameters that are accessible experimentally. These are the degrees of polarization, that represent the polarization of the dipole moment[1] $P(t)$ of the system. With the dipole density $N(t)$, the polarization degrees for circular polarization $\rho_c \propto P_c(t)/N(t)$, linear polarization $\rho_L \propto P_L(t)/N(t)$, and linear polarization $\rho_{L'} \propto P_{L'}(t)/N(t)$ with respect to a basis that is rotated by 45° with respect to the basis of P_L, can be specified. Exemplarily, the linear polarization for $P_L(t)$ will be discussed further.
The response of the 3-level-system in Fig. 4.9 to an illumination can be described by the rate equations

$$\dot{N}_1 = G(t) - W \cdot N_1 \qquad \dot{P}_{1,L} = g_L(t) - (\gamma + W)\, P_{1,L} \tag{4.1}$$

$$\dot{N}_2 = W \cdot N_1 - N_2/\tau \qquad \dot{P}_{2,L} = W \cdot P_{1,L} - P_{2,L}/\tau. \tag{4.2}$$

The generation rates G for the occupation and $g_L(t)$ for the polarization are determined by the selection rules and by the polarization of the laser. Relaxation from the optically excited state $|1\rangle$ to the radiative state $|2\rangle$ occurs with the rate W, while the radiative state is characterized by the lifetime τ. Spin depolarization occurs only in state $|1\rangle$ with rate γ.

The rate equations for the polarization can be solved by an exponential decay with an additive constant

$$\rho_L^x \propto \exp(-\gamma t) + \rho_{L,0}^x. \tag{4.3}$$

This solution is plausible, since after the initiation by a laser pulse, the polarization only decays in $|1\rangle$, leading to an exponential decrease of polarization. As soon as the system has relaxed into state $|2\rangle$, no depolarization takes place any more and a constant value remains. This is a valid approximation, since the polarization in Fig. 4.4 exhibits a plateau-like long-term dependence.
In extension of the model, an additional exponential decay can be conceded for the polarization in $|2\rangle$, so that $\rho_{L,0}^x \propto \exp\left(-t/T_{|2\rangle}\right)$. In this case, the decay constant is very long at $T_{|2\rangle} > 1\,\text{ms}$. The function with an additional exponential term is displayed in Fig. 4.9.

[1] According to the correspondence principle [55], optical transitions can be described by classical dipoles with a frequency equal to the optical transition frequency and a dipole moment equal to the matrix element of the transition.

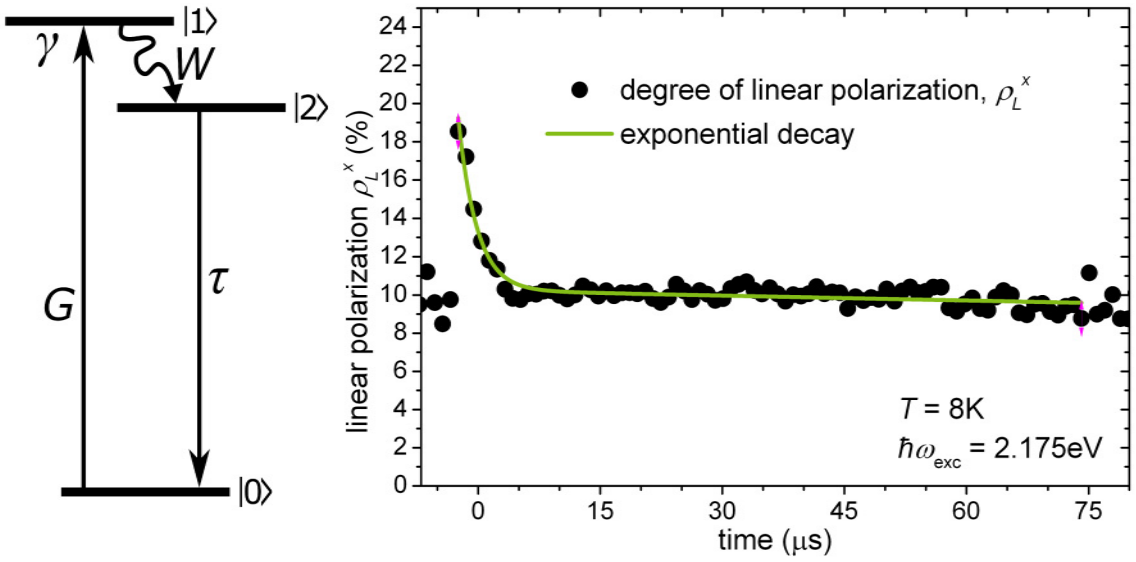

Figure 4.9 Left: 3-level-model of the system involved in the emission of photoluminescence. Electrons are excited from level $|0\rangle$ to level $|1\rangle$ optically at rate G. The relaxation to level $|2\rangle$ is the origin of the Stokes shift and occurs at rate W. The radiative recombination from $|2\rangle$ to $|0\rangle$ exhibits a lifetime of τ. Spin relaxation occurs only in level $|1\rangle$ at rate γ. Right: measurement of the linear degree of polarization (black) and biexponential fit (green) to the data. After a fast decay with a time constant of 2.3 µs, the polarization exhibits an almost constant behavior with a decay constant in excess of 1 ms.

4.5 Conclusion

The polarization of photoluminescence from CdMnTe crystals evidences optical orientation and alignment of resonantly excited Mn^{2+} spins. The degrees of polarization for circularly polarized excitation (optical orientation of spins) and of linearly polarized excitation (optical alignment of spins) amount to 8 % and 10 %, respectively. This is possible by the suppression of spin relaxation due to the low temperatures in experiment, leading to the emergence of a spin glass phase in the studied sample. Thereby, the spin relaxation times are extended to values on the order of a millisecond, exceeding by far the recombination time of the Mn^{2+} excited state, which amounts to 23 µs.

A simple phenomenological model is developed, based on the approximation of isolated centers. Polarizations of up to about 25 % are compliant with the model. The lower values found in experiment can be explained by the disregard of spin depolarization in the model. Possible mechanisms for that include electron-phonon interaction changing the *d*-orbital configuration of electrons and Mn ions and an excitation energy transfer among Mn ions.

The dynamics of the signal can be reproduced by studying a 3-level-system allow-

ing for spin relaxation and the Stokes shift.

The results approve the Mn^{2+} ion in CdTe as an optically active center. The embedding in a spin glass system establishes the connection to collective magnetism and opens perspectives for optical control and recording of information.

5 Spin polarization in a ferromagnet/semiconductor hybrid structure

Hybrid structures consisting of a ferromagnetic layer and a semiconductor are aimed at the integration of magnetism into the semiconductor architecture. They represent an alternative to diluted magnetic semiconductors, which struggle with the loss of their electronical and optical properties at increased magnetic doping levels [28, 29, 130]. Essential for hybrid structures is the interaction of the ferromagnetic layer with the charge carriers in the semiconductor across the barrier separating the two materials.

This interaction is investigated by time-resolved photoluminescence spectroscopy and Kerr rotation for a GaAs-based hybrid structure consisting of an InGaAs quantum well and a ferromagnetic GaMnAs layer. The sample is described in detail in Subsec. 3.1.2. The literature [64–66] predicts the interaction to be a p–d exchange interaction, leading to a spin polarization of holes. This, in turn, leads to a polarization of the photoluminescence emitted from the quantum well.
The polarization observed experimentally, however, exceeds the value that can be expected due to p–d exchange interaction. Instead, the spin-polarized charge carrier is found to be the electron, as shown in Sec. 5.2. Moreover, the dominant mechanism for the spin polarization is found to be a spin-dependent tunneling of electrons from the quantum well into the ferromagnetic layer. The respective measurements are presented in Secs. 5.3 and 5.4. All related phenomena are observed for temperatures up to the Curie temperature of the ferromagnetic layer, confirming its active role in the spin polarization of the charge carriers in the semiconductor quantum well. Parts of the findings are published in [203] and [204].

5.1 Characterization and influence of the ferromagnetic layer

As discussed in Subsec. 2.3.2, a unique property of ferromagnets is the hysteresis of their magnetization in an external magnetic field. The magnetization of the ferromagnetic layer is detected by Kerr rotation (see Sec. 3.3) for a temperature

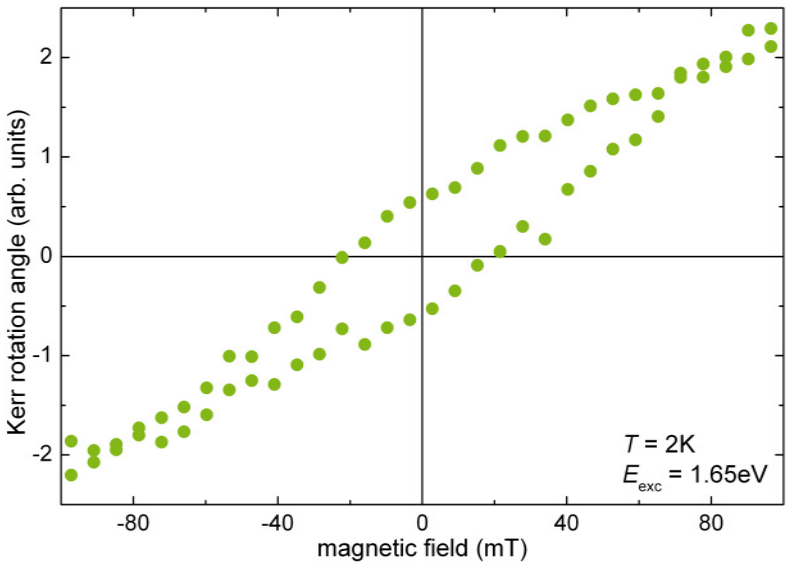

Figure 5.1 Kerr rotation measurement of the ferromagnetic GaMnAs layer in the sample with 10 nm spacer. The Kerr rotation angle is measured as a function of the external magnetic field in Faraday geometry, exposing a hysteresis loop of the magnetization.

of $T = 2\,\mathrm{K}$ and an excitation energy of $E_{\mathrm{exc}} = 1.65\,\mathrm{eV}(\lambda_{\mathrm{exc}} = 750\,\mathrm{nm})$. The low temperature ensures ferromagnetism ($T < T_{\mathrm{C}}$) and a prolonged spin relaxation. The sample is excited from the side of the GaMnAs layer. The detection is thus only sensitive to the magnetization of the GaMnAs and is not influenced by the magnetization of the quantum well, which is confirmed by the independence of the characteristic magnetic parameters from the excitation energy. The Kerr rotation measurement reveals a hysteresis loop shown in Fig. 5.1. Saturation starts at approximately 80 mT external field and the coercive force is about 15 mT.

The influence of the ferromagnetic layer on the semiconductor quantum well is studied by the photoluminescence from the quantum well. The photoluminescence spectrum of the sample is given in Fig. 5.2 (black line). Apart from lines stemming from the GaAs buffer layer at 1.51 eV (exciton–impurity complex, not shown) and 1.49 eV (band-shallow acceptor, not shown), a peak corresponding to the electron-heavy hole recombination in their quantum well ground states at about 1.417 eV is observed.

An influence of the ferromagnetic layer should manifest itself in a spin polarization of the charge carriers inside the quantum well. This spin polarization can be detected by studying the degree of polarization of the photoluminescence under linearly polarized excitation, since the radiative recombination of charge carriers is subject to selection rules (see Subsec. 2.2.5). A spin polarization of either electron or hole spins in the quantum well leads to a polarization of the photoluminescence.

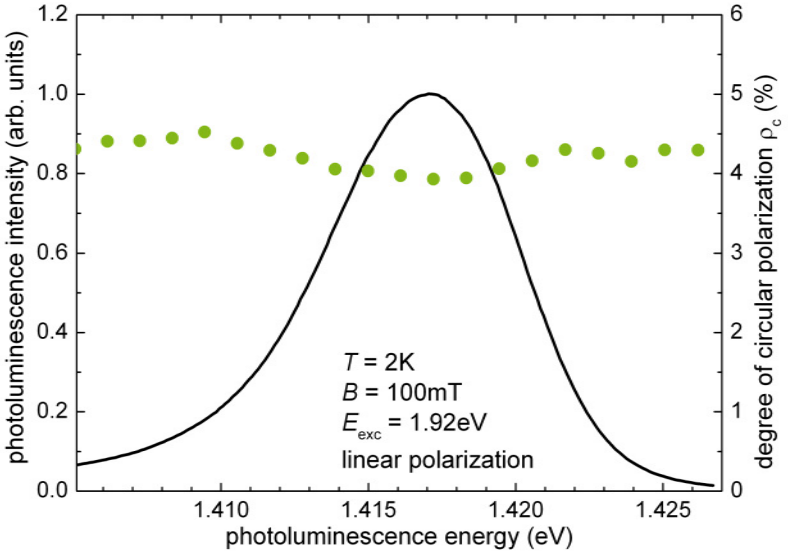

Figure 5.2 Photoluminescence spectrum and degree of circular polarization (green circles, right axis) under linearly polarized excitation of the sample with 10 nm spacer. At the maximum of photoluminescence intensity, a circular polarization of about 4 % is observed in a Faraday field of 100 mT.

That means that the intensities I_+ and I_- for the σ^+ and σ^- circularly polarized parts of the photoluminescence, respectively, are of different magnitude and the degree of circular polarization defined in Eq. (3.1) is unequal to zero.

As can be seen in Fig. 5.2 (green circles), a sizeable polarization of about 4 % is observed for an external magnetic field of $B = 100\,\mathrm{mT}$ in Faraday geometry. This polarization is induced by the ferromagnetic layer, as in structures that do not possess a GaMnAs layer, no polarization can be observed for magnetic fields in this range and for linearly polarized excitation.

Additionally, if the spin polarization is induced by the ferromagnetic layer, the degree of polarization is expected to show a hysteresis-like behavior depending on the magnetization. For this, the magnetic field dependence of the photoluminescence from the quantum well is examined by exciting charge carriers quasi-resonantly with photon energies of $E_{\mathrm{exc}} = 1.44\,\mathrm{eV} (\lambda = 861\,\mathrm{nm})$. This below-barrier excitation permits optical access to the quantum well through the GaAs substrate. By avoiding an excitation involving the transmission through the GaMnAs layer, any magnetic circular dichroism effect of the ferromagnetic layer can be excluded.

Indeed, as Fig. 5.3 shows, the degree of circular polarization of the photoluminescence from the quantum well follows a hysteresis that is similar to the one that was measured for the ferromagnetic layer by Kerr rotation (compare Fig. 5.1). This demonstrates that the ferromagnetic layer influences the spins of the charge carriers inside the quantum well and a read out of the ferromagnet's magnetization by

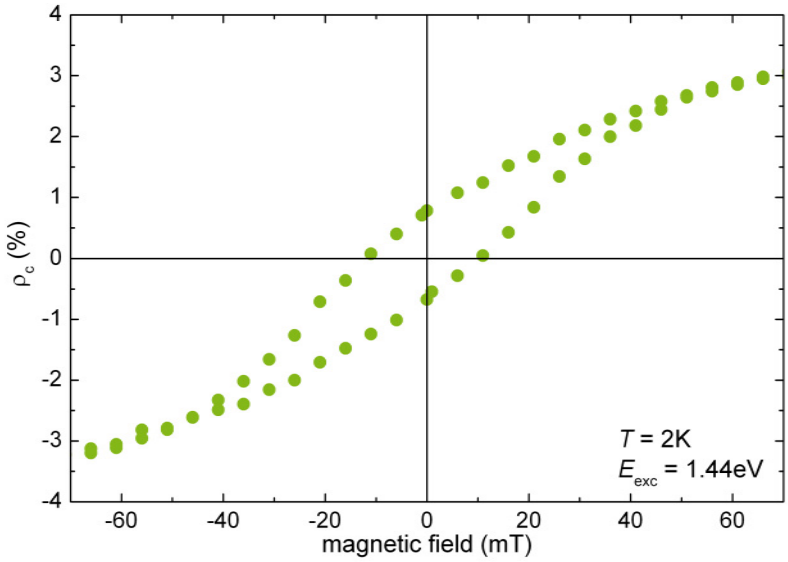

Figure 5.3 Degree of circular polarization of the photoluminescence from the quantum well in the sample with 10 nm spacer under linearly polarized excitation. A clear hysteresis curve is observed, proving the influence of the ferromagnet.

examining the charge carriers of the quantum well is possible.

In order to determine which charge carrier (electron or hole) experiences spin polarization and to reveal the mechanism of interaction, further investigations were carried out.

5.2 Determination of the polarized charge carrier

A distinguishing feature for the spin polarization of electrons and holes is their different spin relaxation rates (see Subsec. 2.2.6).

In order to determine the respective times, optical orientation measurements are carried out. Spin-polarized charge carriers are excited optically and the degree of circular polarization is extracted from the photoluminescence (see Subsec. 3.2.1).

Figure 5.4 shows the degree of circular polarization under circularly polarized excitation ρ_c^σ for $B = 0$ and $B = 125\,\mathrm{mT}$. The influence of the magnetic field is evidenced by a considerable reduction of spin depolarization in the longitudinal magnetic field. The initial fast decay of ρ_c^σ exhibits a time constant on the order of the resolution of the setup and is attributed to the relaxation of the hole spin (see "spin relaxation" in Subsec. 2.2.6). The spin relaxation time of electrons is $\tau_S = 9\,\mathrm{ns}$ at $B = 0$ and increases to $> 30\,\mathrm{ns}$ under the application of a longitudinal magnetic field with $B = 125\,\mathrm{mT}$. A magnetic field of this strength aligns all magnetic domains of the ferromagnet (see Fig. 5.1). The spin relaxation of electrons caused by the interaction with differently oriented magnetic domains of the ferromagnet is hence

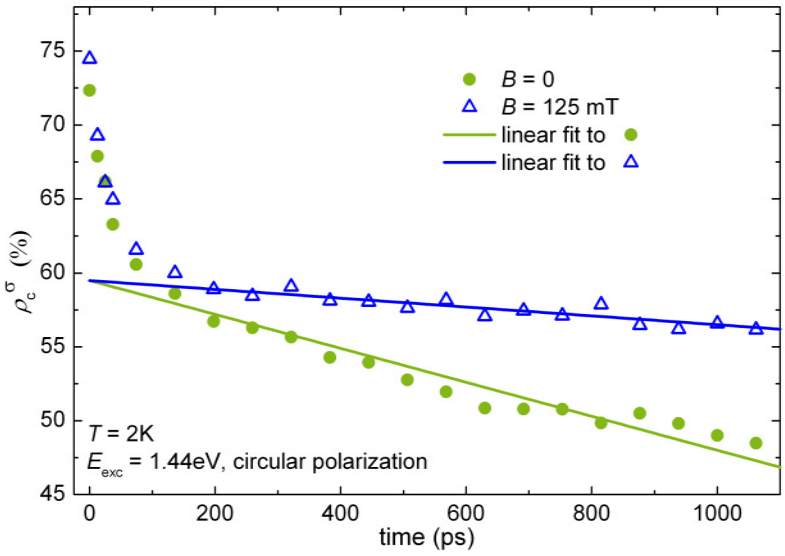

Figure 5.4 Degree of circular polarization of photoluminescence after circularly polarized excitation (optical orientation) of the sample with 10 nm spacer. After an initial fast decay, the polarization decays with a time constant of 9 ns for $B = 0$. The application of a longitudinal magnetic field with $B = 125$ mT extends the time constant to > 30 ns.

suppressed.

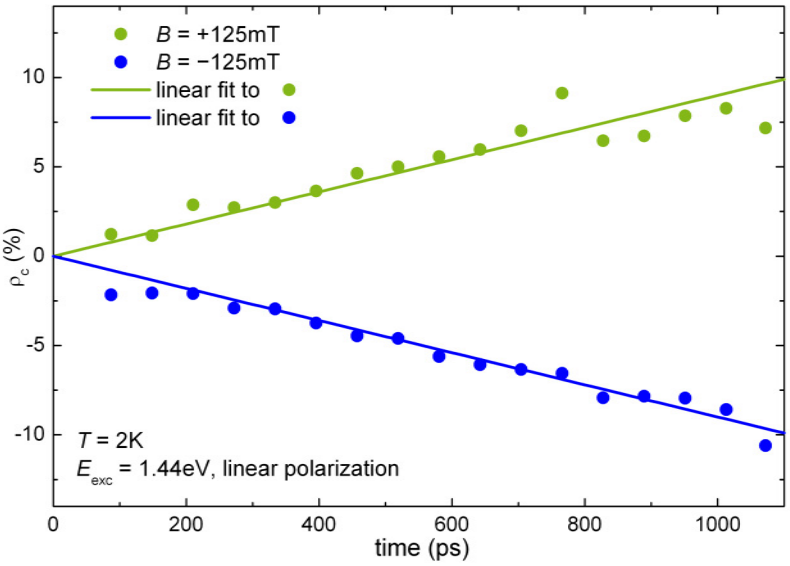

Figure 5.5 Time dependence of the degree of circular polarization of the photoluminescence under linearly polarized excitation. The degree of circular polarization ρ_c rises monotonically with time, exhibiting a time constant of 11 ns for both field orientations.

For linearly polarized excitation, the time dependence of the degree of circu-

lar polarization ρ_c is shown in Fig. 5.5 for magnetic fields of $B = 125\,\mathrm{mT}$ and $B = -125\,\mathrm{mT}$. The sign of ρ_c follows the magnetic field and the direction of magnetization of the ferromagnet. The degree of circular polarization rises monotonically throughout the entire observation period of 1 ns. Therefore it must be concluded that the spin relaxation time of the involved charge carrier exceeds 1 ns. A linear fit to the data yields a time constant of 11 ns. In the system under study this is only plausible for the electron.

Consistently, the equilibrium polarization of hole spins due to p–d exchange interaction, as previously discussed in the literature [64–66] must be ruled out as the primary cause of the observed polarization.

5.3 Spin-dependent capture of charge carriers

For electron spins, the s–d exchange interaction with Mn ions causes an effective magnetic field in which the spins get polarized due to thermal occupation of spin-split levels.

The effective magnetic field B_{ex} that results from the exchange interaction with the ferromagnet can be detected with the Hanle effect [55, 185]. Spin-polarized charge carriers are injected optically by circularly polarized continuous-wave excitation. The polarization of the photoluminescence is measured as a function of the external magnetic field applied in Voigt geometry. In the time-integrated detection, the field-induced Larmor precession of the injected spins results in depolarization of the photoluminescence with rising field. The characteristic field for the depolarization must be on the order of the internal field leading to polarization. The Hanle curve for the studied sample is shown in Fig. 5.6.

It displays a clear hysteresis with a characteristic width of about 15 mT, which is the same value as was found for the coercive force of the ferromagnetic layer by Kerr rotation measurement in Sec. 5.1. For increasing field strength (both positive and negative signs), the polarization decreases, reaching the half maximum value at about $B_{1/2} = 40\,\mathrm{mT}$. This represents an upper bound for the exchange field B_{ex}, so that the spin level splitting can be estimated to

$$\Delta E_{\mathrm{ex}} \leq 2\mu_B |g| B_{1/2} \approx 2.5\,\mu\mathrm{eV}, \tag{5.1}$$

where the electron Landé factor $|g| = 0.53$ is used. This is considerably smaller than the estimated 8.5 meV for an electron in ferromagnetic GaMnAs [205].

Another way to determine the characteristic energy scale of the splitting by exchange interaction is time-resolved Kerr rotation (see Subsec. 3.3.1). In Fig. 5.7, Kerr rotation transients for different external magnetic fields are shown. As can be seen, the external field in Voigt configuration induces oscillations of the optically injected spins. The curves can be described by two components: one fast-decaying

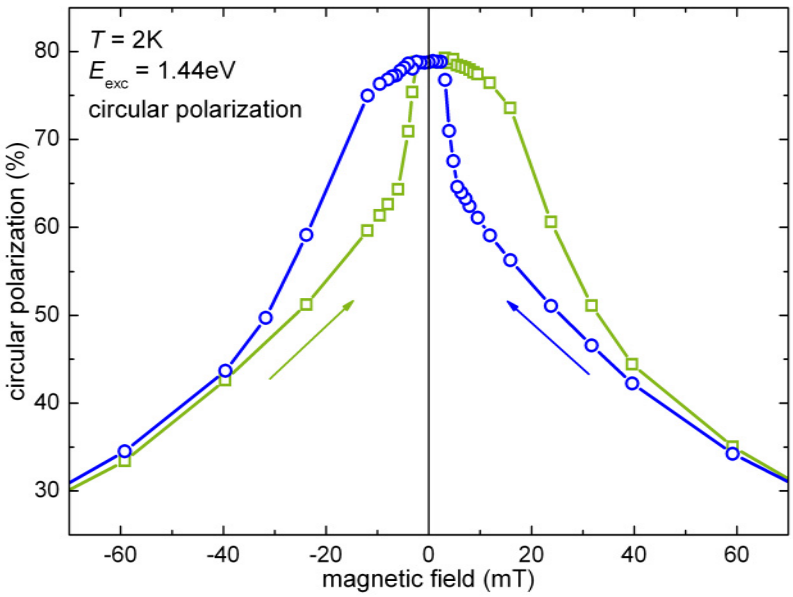

Figure 5.6 Hanle curve for the photoluminescence from the quantum well. Green squares are measured for increasing magnetic field, blue circles are measured for decreasing magnetic field.

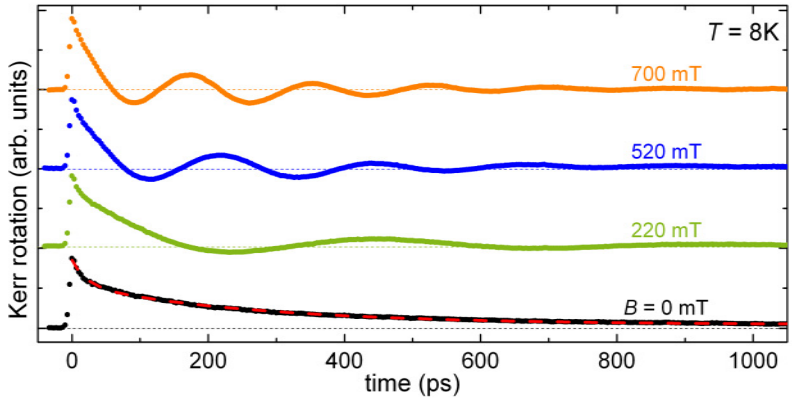

Figure 5.7 Time-resolved Kerr rotation measurements for different magnetic fields in Voigt geometry for the sample with $d_S = 10\,\text{nm}$ spacer. The excitation energy is tuned to the exciton resonance in order to investigate the charge carriers in the quantum well, instead of in the ferromagnetic layer. The curves are shifted vertically for better readability. For ero field, a double-exponential decay was fitted to the data (dashed red curve).

signal and a long-living part. The fast decay is attributed to the spin relaxation of holes with a relaxation time of $\tau_S^h = 20\,\text{ps}$. This value is in agreement with the spin relaxation time extracted from the optical orientation measurements in Fig. 5.4. The long-living component is assigned to the electrons, yielding an electron-spin

lifetime of $\tau_S = 0.3\,\mathrm{ns}$. The field-induced oscillations can be well described by $\cos(\Omega_\mathrm{L} t)\exp(-t/\tau_S)$, where Ω_L denotes the Larmor frequency. In Fig. 5.8, the Lar-

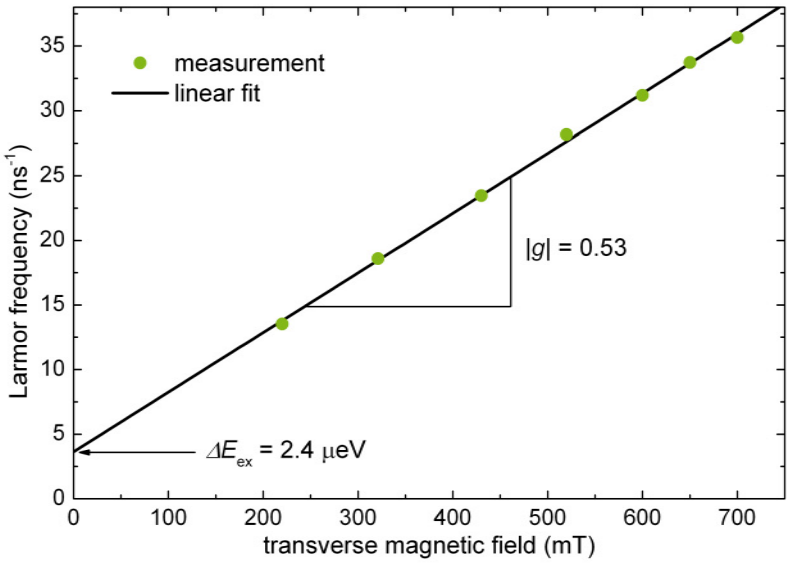

Figure 5.8 Larmor precession frequencies extracted from Kerr rotation for different magnetic fields. The slope of the linear fit gives a Landé factor of $|g| = 0.53$ and the y-intercept indicates a zero-field spin splitting of $\Delta E_\mathrm{ex} = 2.4\,\mu\mathrm{eV}$.

mor frequency of the long-living component is plotted in dependence of the magnetic field. From the slope of the curve, a Landé factor of $|g| = 0.53$ can be extracted. This corroborates the conclusion of Sec. 5.2, associating the long spin relaxation time with the electron and thereby identifying the electron as the spin-polarized charge carrier.

Additionally, in Fig. 5.8, a y-intercept can be observed, that is a measure for the zero-field spin splitting induced by s–d exchange interaction with the ferromagnetic layer and amounts to $\Delta E_\mathrm{ex} = 2.4\,\mu\mathrm{eV}$.

This splitting leads to an equilibrium spin polarization of $P_\mathrm{ex} = \frac{\Delta E_\mathrm{ex}}{2k_b T} < 0.5\,\%$ at $T = 2\,\mathrm{K}$ (k_B is the Boltzmann constant), which is considerably smaller than the 4 % found in experiment. It must therefore be concluded that the (equilibrium) exchange interaction has to be ruled out as the primary mechanism of the observed polarization.

In order to identify additional effects, that lead to spin polarization, the role of the ferromagnetic layer was studied further by varying the distance to the quantum well, i.e. by varying the spacer thickness d_S (see the sample description in Subsec. 3.1.2).

The bottom panel of Fig. 5.9 shows the time dependence of the degree of circular polarization of the photoluminescence under linearly polarized below-barrier excitation for spacers of 5 nm and 10 nm thickness. For both spacers, the initial degree of circular polarization is close to zero and rises linearly with time. However, for

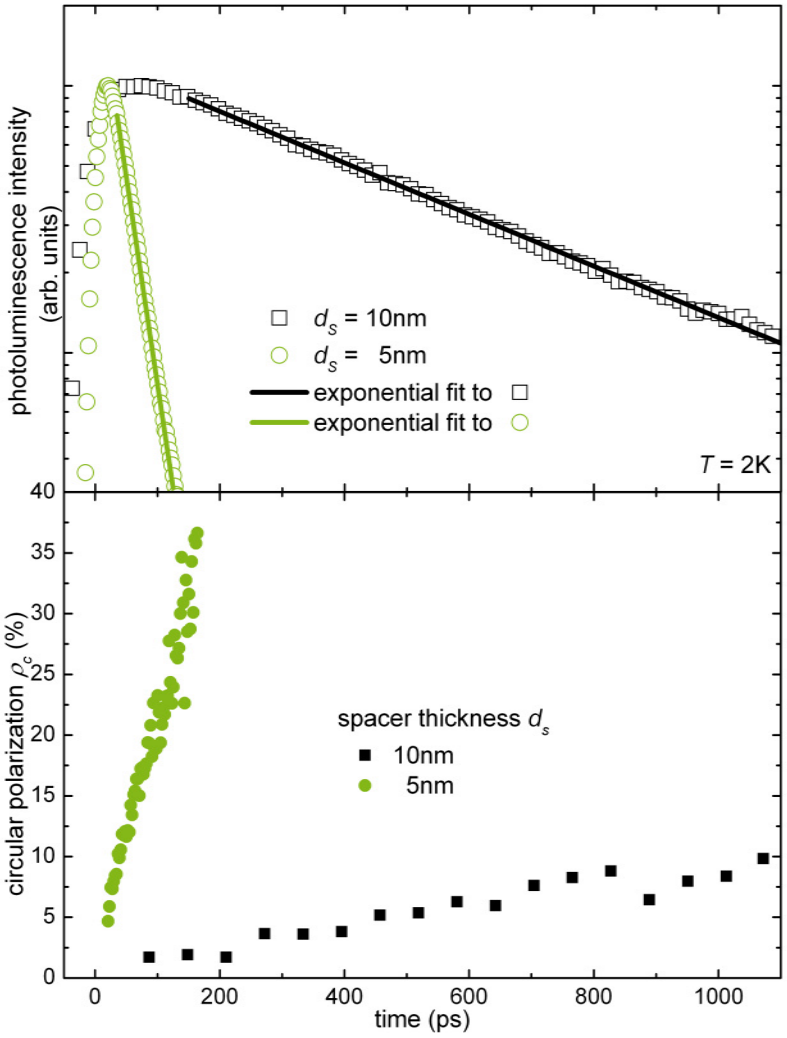

Figure 5.9 Top panel: decay of the photoluminescence intensity for spacers of $d_S = 10\,\text{nm}$ (black) and $d_S = 5\,\text{nm}$ (green) thickness. The curves are well described by exponential decays with time constants of 450 ps and 30 ps, respectively. Bottom panel: degree of circular polarization under linearly polarized excitation for the same spacer thicknesses.

the sample with thinner spacer, ρ_c increases about 25 times faster and reaches much higher values (10 % vs. 35 %).

The top panel of Fig. 5.9 gives the time dependence of the photoluminescence intensity for the above spacer thicknesses. Both transients exhibit exponential decay with $I \propto \exp(-\Gamma t)$, but the time constants are very different. While the photoluminescence from the quantum well that is separated by $d_S = 10\,\text{nm}$ from the ferromagnetic layer decays with $\Gamma_{10\text{nm}}^{-1} = 450\,\text{ps}$, the decay for the sample with $d_S = 5\,\text{nm}$ is about 15 times faster at $\Gamma_{5\text{nm}}^{-1} = 30\,\text{ps}$.

Earlier experiments of Epstein et al. [206] showed non-equilibrium polarization

of free electrons in MnAs/bulk-GaAs structures, that were explained by Ciuti et al. [207] by spin-dependent reflection from the ferromagnet/semiconductor interface. In the case discussed here, however, the polarization is observed even when the photon energy of the excitation is tuned below the band-gap of GaAs $\hbar\omega < E_g^{GaAs}$, so that charge carriers are excited in the quantum well only.

The pronounced dependence of both the polarization and the photoluminescence intensity on the spacer thickness d_S, suggests a spin-dependent escape of charge carriers from the quantum well into the ferromagnet. Under linearly polarized excitation, the observed polarization (as in Fig. 5.5) is hence caused by an asymmetry of the tunneling rates γ_+ and γ_- for charge carriers with spin along and opposite to the magnetization, leading to an accumulation of charge carriers with spins opposite to those leaving the quantum well faster. In this way, the ferromagnet acts as a spin separator by spin-dependent capture of charge carriers.

The asymmetry in capture rates can be detected directly by optically injecting spins along or opposite to the magnetization by circular polarized excitation. Due to the competition of radiative recombination with the spin-dependent capture by the ferromagnet, the total intensity of photoluminescence must depend on the helicity of exciting light, since it is proportional to the amount of electrons in the quantum well.

For the evaluation of this effect, the modulation parameter

$$\eta = \frac{I^+ - I^-}{I^+ + I^-} \tag{5.2}$$

is defined. The intensities $I^\pm$ denote the total photoluminescence intensity for $\sigma^\pm$-polarized excitation.
This must not be confused with the degree of circular polarization ρ_c (see Eq. (3.1)), where the intensities $I_\pm$ (with a subscript) denote the $\sigma^\pm$-polarized components of the photoluminescence, hence in the detection.

In Fig. 5.10, the dependence of η on the external magnetic field is shown. The sizeable modulation of 3 % and the hysteresis are clear signs for the spin dependent capture by the ferromagnetic layer.

Additionally, the almost identical curves for $\rho_c(B)$ and $\eta(B)$ indicate a close interdependence between the two quantities, that can be explained by analyzing their relation to the electron polarization P.

The optical orientation [55] of electrons for the case discussed here is described by the rate equations

$$\begin{aligned}
\frac{\mathrm{d}n_+}{\mathrm{d}t} =& \frac{G}{2}(1+P_i) - \gamma_+ n_+ - \frac{n_+}{\tau} - \frac{n_+ - n_-}{2\tau_S} \\
\frac{\mathrm{d}n_-}{\mathrm{d}t} =& \frac{G}{2}(1-P_i) - \gamma_- n_- - \frac{n_-}{\tau} - \frac{n_- - n_+}{2\tau_S},
\end{aligned} \tag{5.3}$$

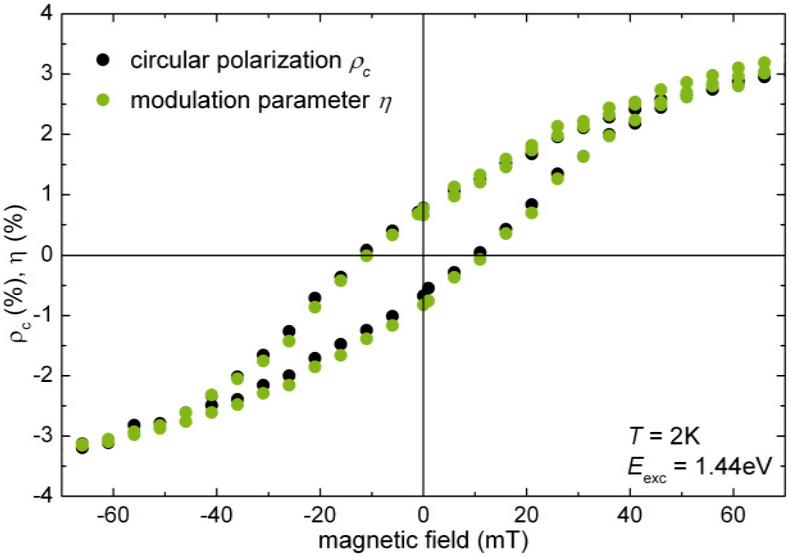

Figure 5.10 Modulation parameter (green) and degree of circular polarization (black) in an external magnetic field. The hysteresis proves the influence of the ferromagnetic layer and the almost identical curves suggest a close relation between η and ρ_c.

where $n_\pm$ denotes the number of electrons with spin up/down, G is their generation rate, τ their radiative recombination time, τ_S the electron spin lifetime and P_i their initial polarization due to the selection rules. For resonant excitation of the heavy hole subband with $\sigma_\pm$ polarized light, the initial polarization is $P_i = \mp 1$ [78]. The parameters $\gamma_\pm$ account for the capture rates for electrons with spin projections $m_s = \pm 1/2$ into the ferromagnet. Due to the very fast relaxation, the spin polarization of holes is neglected. The equilibrium polarization of electron spins due to s–d exchange interaction was quantified by the Hanle effect (Fig. 5.6) and by Kerr rotation measurements (Fig. 5.8) and can be neglected due to its small value.

With the definition of the mean capture rate $\gamma = (\gamma_+ + \gamma_-)/2$ of electrons by the ferromagnet and a parameter $\beta = (\gamma_+ - \gamma_-)/(\gamma_+ + \gamma_-)$ characterizing the difference in capture rates for the two spin-orientations, the steady-state number of electrons

$$n = n_+ + n_- = \frac{g}{1/\tau + \gamma + \gamma\beta P} \tag{5.4}$$

and their spin polarization

$$P = \frac{n_+ - n_-}{n_+ + n_-} = \frac{(\gamma + 1/\tau)\, P_i - \gamma\beta}{\gamma + 1/\tau + 1/\tau_S - \gamma\beta P_i} \tag{5.5}$$

can be specified.

Since β is an odd function of the magnetization M_z, Eq. (5.4) states that the concentration of electrons depends on the mutual orientation of the spin polarization P and the magnetization M_z. This becomes most pronounced, when the

spin-dependent capture of the ferromagnet dominates, i.e. for $\gamma\tau \gg 1$. Similarly, the polarization of electrons inside the quantum well (see Eq. (5.5)) is not only characterized by the optical orientation described by the term $\propto P_i$, but also contains a contribution that is $\propto -\beta$. The minus sign indicates that the spin polarization prevailing in the quantum well is directed opposite to the spin species that is captured at a greater rate.

With Eqs. (5.4) and (5.5) and the selection rules for optical transitions between the electron and the heavy hole subband, the degree of circular polarization for linearly polarized ($P_i = 0$) excitation is

$$\rho_c = -P = -\frac{n_+ - n_-}{n_+ + n_-} = \frac{\gamma\beta}{\gamma + 1/\tau + 1/\tau_S}, \tag{5.6}$$

and the modulation parameter for circularly polarized excitation ($|P_i| = 1$) reads

$$\eta = \frac{n(-|P_i|) - n(+|P_i|)}{n(-|P_i|) + n(+|P_i|)} = \frac{\gamma\beta}{\gamma + 1/\tau + 1/\tau_S}|P_i|. \tag{5.7}$$

As can be seen, the remarkable relation

$$\eta(B) = |P_i|\rho_c(B) \tag{5.8}$$

connects the degree of circular polarization and the modulation parameter. Moreover, in the case of resonant excitation of the quantum well heavy hole subband, the value of P_i is close to unity, making the magnetic field dependencies of η and ρ_c equal. This equality is also observed in experiment as shown in Fig. 5.10.

5.4 Kinetics of spin dependent capture

The parameters describing the dynamics of the photoluminescence and the polarization can be determined by time-resolved photoluminescence spectroscopy (see Sec. 3.2). The decay of the photoluminescence signal monitors the total decay rate $\Gamma = 1/\tau + \gamma$ of electrons due to radiative recombination ($\propto 1/\tau$) and capture by the ferromagnet ($\propto \gamma$). The spin-related parameters, such as the relaxation time τ_S and the spin accumulation rate $(\gamma_+ - \gamma_-)/2$ are monitored by the polarization $\rho_c(t)$ and the modulation $\eta(t)$. The rate equations (5.3) can be used for the calculation of spin dynamics after the excitation, when the generation rate is set to zero, $G = 0$. For the definition of the initial conditions $n_\pm(t = 0) = n_\pm^0$, the different polarizations have to be taken into account. For excitation with $\sigma^\pm$-polarized light and ideal selection rules, the initial populations are $n_\mp^0 = 1$ and $n_\pm^0 = 0$. For linearly polarized excitations, the populations are equal: $n_+^0 = n_-^0$.

As can be seen from the experiments (see Fig. 5.5), the photoluminescence intensity exhibits a much shorter time constant than the polarization and the modulation.

Consequently, the total decay rate of electrons must be much larger than the spin relaxation rate, $\Gamma \gg 1/\tau_S$, and also much larger than the spin accumulation rate, $\Gamma \gg (\gamma_+ - \gamma_-)/2$. In this case the rate equations can be simplified, so that the observable quantities read

$$I(t) = \left(n_+^0 + n_-^0\right) \exp\left(-\Gamma t\right) \tag{5.9}$$

$$\rho_c(t) = \frac{n_+^0 - n_-^0}{n_+^0 + n_-^0}\left(1 - \frac{t}{\tau_S}\right) + \frac{2n_+^0 n_-^0\left(\gamma_+ - \gamma_-\right)}{\left(n_+^0 + n_-^0\right)^2} t \tag{5.10}$$

$$\eta(t) = \frac{\gamma_+ - \gamma_-}{2} t. \tag{5.11}$$

The photoluminescence intensity decays with the total escape rate Γ and the intensity modulation is determined by the spin accumulation rate, i.e. half the difference of the capture rates γ_+ and γ_- for spin up and spin down. For the evolution of the polarization ρ_c, it is instructive to consider two different cases of excitation: (i) for circularly polarized excitation, e.g. σ^+ (and hence $n_-^0 = 1,\ n_+^0 = 0$), the degree of polarization

$$\rho_c(t) = 1 - \frac{t}{\tau_S} \tag{5.12}$$

is (initially) determined by the spin relaxation time τ_S. Since the electrons are excited fully spin-polarized and the spin dependent capture by the ferromagnet does not mix the populations of spin up and spin down, the depolarization of the photoluminescence is initially caused only by spin relaxation. (ii) For linearly polarized excitation ($n_+^0 = n_-^0$), the situation is quite the opposite. The degree of polarization

$$\rho_c = \frac{\gamma_+ - \gamma_-}{2} t \tag{5.13}$$

is determined only by the spin accumulation rate and equal to the modulation. Since the populations of spin up and spin down electrons are equal at $t = 0$, the spin relaxation term, being proportional to the difference in populations ($\propto n_\pm - n_\mp$), does not contribute. Hence for the case of linearly polarized excitation, the electron spin polarization is attributed only to the spin dependent capture by the ferromagnet.

Time-resolved photoluminescence spectroscopy is sensitive to $I(t)$, $\rho_c(t)$ and $\eta(t)$, and therefore grants access to the dynamic parameters Γ, $\gamma_+ - \gamma_-$ and τ_S, characterizing the spin dependent capture effect.

In the top panel of Fig. 5.9, the decay of the photoluminescence intensity is shown for samples with spacer thicknesses of 5 nm and 10 nm. The exponential decays reveal time constants Γ^{-1} of 440 ps for the 10 nm spacer and 30 ps for the 5 nm spacer. The decay of the photoluminescence intensity also limits the observation

of the polarization dependent quantities ρ_c and η. The steep variation of Γ with the spacer thickness signifies a strong contribution of the electron capture by the ferromagnet.

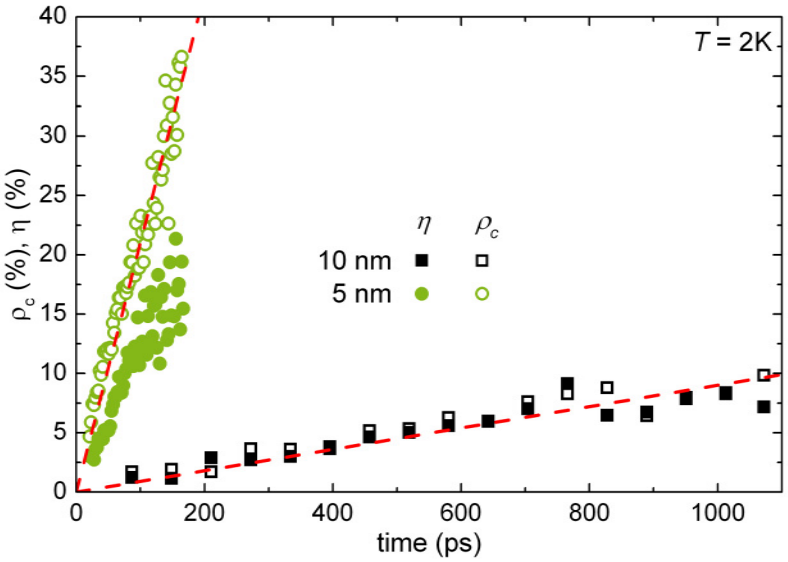

Figure 5.11 Transients of the degree of circular polarization ρ_c (solid symbols) and the modulation parameter η (open symbols) for spacer thicknesses of 5 nm (black) and 10 nm (green). The dashed red curves are linear fits to the polarization data for the extraction of the spin accumulation rate.

The transients of the modulation parameter $\eta(t)$ (under circular excitation, solid symbols) for spacer thicknesses of 5 nm and 10 nm are shown in Fig. 5.11. For comparison, the degree of circular polarization $\rho_c(t)$ (under linear excitation, open symbols) is repeated (compare Fig. 5.5). At $t = 0$, both quantities are zero, verifying the absence of an equilibrium spin polarization. In accord with Eq. (5.11), they increase linearly with time, reaching polarizations of about 10 % for the 10 nm spacer and 30 % for the 5 nm spacer during the respective electron lifetime. Linear fits to the data (according to (5.13)) reveal spin accumulation rates $(\gamma_+ - \gamma_-)^{-1}$ of 5.5 ns for the 10 nm spacer and 240 ps for the 5 nm spacer. For the sample with $d_S = 10$ nm, the transients for the degree of polarization ρ_c and for the modulation parameter η coincide, giving an initial polarization of $P_i = 1$. This is not the case for the sample with spacer thickness $d_S = 5$ nm. Here, the modulation parameter stays behind the degree of polarization, signifying a less efficient spin polarization $P_i < 1$.

5.5 Temperature dependence

In order to confirm that the effects discussed above are indeed a consequence of the interaction with the ferromagnetic layer, the relevant parameters are measured as a

function of temperature. If caused by the ferromagnet, the difference in capture rates $\gamma_+ - \gamma_-$, the zero field splitting ΔE_{ex} and the Kerr rotation angle should all show a distinct temperature dependence and drop to zero when the Curie temperature of the GaMnAs is reached and the ferromagnetism is lost.

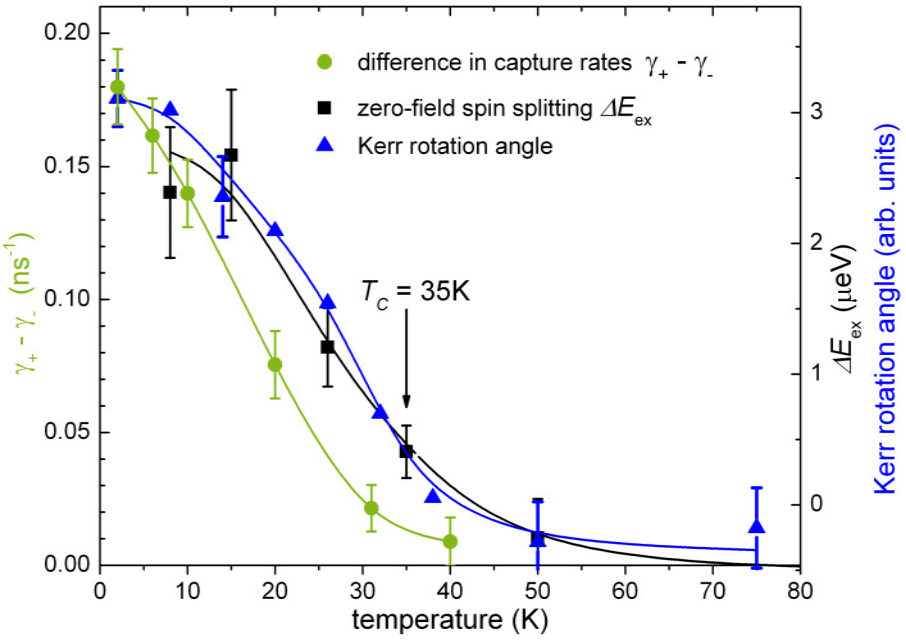

Figure 5.12 Temperature dependence of difference of capture rates (green circles), zero field spin splitting (black squares) and Kerr rotation angle (blue triangles). Solid lines are guide to the eye.

All three parameters exhibit a pronounced temperature dependence that is also clearly correlated, as the data in Fig. 5.12 shows. The signals vanish at about the Curie temperature $T_C = 35\,\mathrm{K}$, confirming that the observed phenomena are indeed induced by the ferromagnetism of the GaMnAs layer.

5.6 Conclusion

The ferromagnet/semiconductor hybrid structure is analyzed with regard to the interaction between the ferromagnetic layer and the charge carriers in the semiconductor quantum well. Kerr rotation measurements reveal the characteristic parameters of the ferromagnetic GaMnAs layer by studying the magnetic field dependence. The same parameters are measured for the magnetic field dependence of the circular degree of polarization that is emitted from the semiconductor quantum well. Thus, the circular degree of polarization is a consequence of a spin polarization induced by the ferromagnet, demonstrating an effective interaction. The temporal analysis of

the degree of polarization reveals time constants that are typical for electron spins in the studied material.
Additionally, the photoluminescence intensity is dependent on the helicity of the excitation and exhibits the same magnetic field dependence. The pronounced dependence on the thickness of the spacer between the ferromagnet and the semiconductor suggests a spin-dependent tunneling of electrons from the semiconductor quantum well into the ferromagnet.

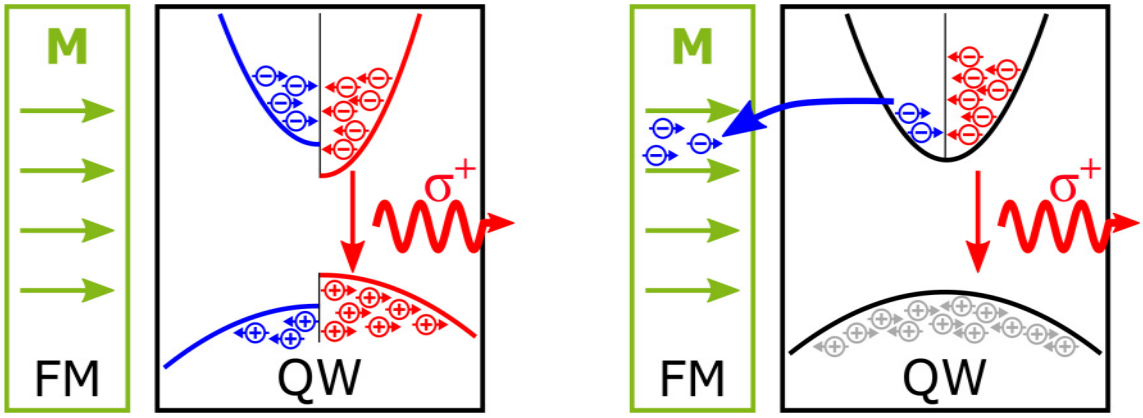

Figure 5.13 Two main effects for the ferromagnet-induced spin polarization of photoluminescence emitted from a quantum well (QW). An external magnetic field ($B = 100\,\mathrm{mT}$) is applied in-plane. Left: the energy-levels of charge carriers are split due to $s(p)$–d exchange interaction. Due to thermal occupation, the levels are populated unequally which leads to polarized photoluminescence. Right: A spin-dependent tunneling of electrons into the ferromagnetic layer (FM) is induced. Due to the additional relaxation channel, a dynamic spin polarization and hence optical polarization occurs.

Two main effects for the ferromagnet-induced spin polarization of quantum well electrons are identified: the first one is the equilibrium spin polarization due to the thermal occupation of split spin levels. The splitting is caused by the effective magnetic field that is a consequence of the s–d exchange interaction with the Mn ions of the ferromagnet. The second effect is a non-equilibrium spin-dependent transfer of electrons through the interface between semiconductor and ferromagnet.
While the first effect is well known and expected for such a hybrid structure [64–66], the second effect is unexpected and demonstrated for the first time (published in [203]).

6 Transfer of coherence using photon echoes from trions in a semiconductor quantum well

For the exploitation of the quantum character of spin states in the operation of spintronic devices, the processes have to preserve coherence. The photon echo discussed in Subsec. 2.2.4 is such a process. It can be investigated using four-wave-mixing spectroscopy as described in Sec. 3.4.

The photon echo is an optical phenomenon, that per se does not include any relation to the spin degree of freedom. The involvement of spin is achieved by utilizing polarized light and exploiting the optical selection rules (Subsec. 2.2.5) of the trion resonance. In the investigated sample described in Subsec. 3.1.3, the trion resonance is spectrally isolated and can be selectively excited by picosecond laser pulses – as will be discussed in Sec 6.1.

The access to the spin degree of freedom allows a manipulation of the photon echo by an external magnetic field. More precisely, the optical coherence that is imprinted by the laser pulses in a spontaneous photon echo experiment can be transferred into the spin state of the resident electron. This is demonstrated in Sec. 6.3. The subsequent optical retrieval of the transferred coherence is shown in Sec. 6.4 by the application of an additional laser pulse in a stimulated photon echo experiment. In order to minimize scattering effects and to maximize the coherence times, all experiments shown in the following were conducted at a temperature of $T = 2\,\mathrm{K}$. Furthermore, the excitation power is kept in the linear regime to avoid many-body effects and excitation-induced dephasing.

6.1 Spectral dependence of four-wave-mixing

The photoluminescence spectrum of the sample described in Subsec. 3.1.3 is shown in Fig. 6.1 (green). It exhibits clear features of the quasiparticles discussed in Sec. 2.2, namely the exciton recombination (X) at 1.601 eV and the trion recombination (T) at 1.599 eV. The additional binding energy of the trion (about 2 meV) makes it possible to selectively excite excitons or trions using spectrally narrow picosecond laser pulses (as indicated by the black line in Fig. 6.1).

The spectral dependence of the four-wave-mixing signal from the CdTe quantum

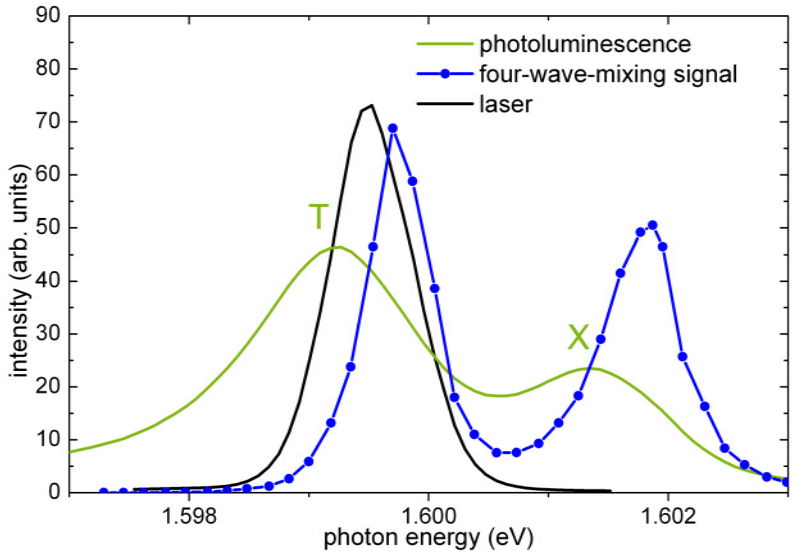

Figure 6.1 Photoluminescence spectrum (green) and four-wave-mixing signal (blue) of the studied CdTe-based quantum well sample and spectrum of the laser source (black) used for excitation in the experiments. The recombination peaks of exciton (X) and trion (T) are spectrally well separated, so that a selective excitation with picosecond laser pulses is possible.

well at zero time delay is shown in blue in Fig. 6.1. The responses from the exciton and trion resonances are clearly resolved and coincide well with the spectrum of photoluminescence. The Stokes shift of 0.5 meV indicates a spectral diffusion of excitons and trions towards localization sites caused by fluctuations of the width and composition of the quantum well. A tuning of the laser wavelength to the lower-energy flank of the trion peak even allows to selectively excite trions with enhanced localization.

6.2 Power dependence of four-wave-mixing

In Subsec. 2.2.4, the photon echo process is explained for optical excitation pulses possessing pulse areas of $\pi/2$ and π. In experiment it is desirable to keep the response of the medium in the linear regime, preventing unwanted nonlinear effects. Such effects, like exciton-exciton scattering, band gap renormalization, nonlinearities in absorption and reflection, and heating, lead to an enhanced decoherence obstructing the observation of coherent phenomena. For the four-wave-mixing signal, the linear regime is characterized by $E_{\mathrm{FWM}} \propto E_1 E_2^2$, compare Eq. (3.7). Any deviation from that dependence is an indication of excitation induced dephasing. Figure 6.2 shows the dependence of the FWM amplitude on the intensities of the first (left) and second (right) excitation pulse. The FWM signal is measured while the intensity of one of

the beams is changed. The intensity of the other beam is thereby kept constant at an intermediate level. The maximum intensity is limited by the laser system.

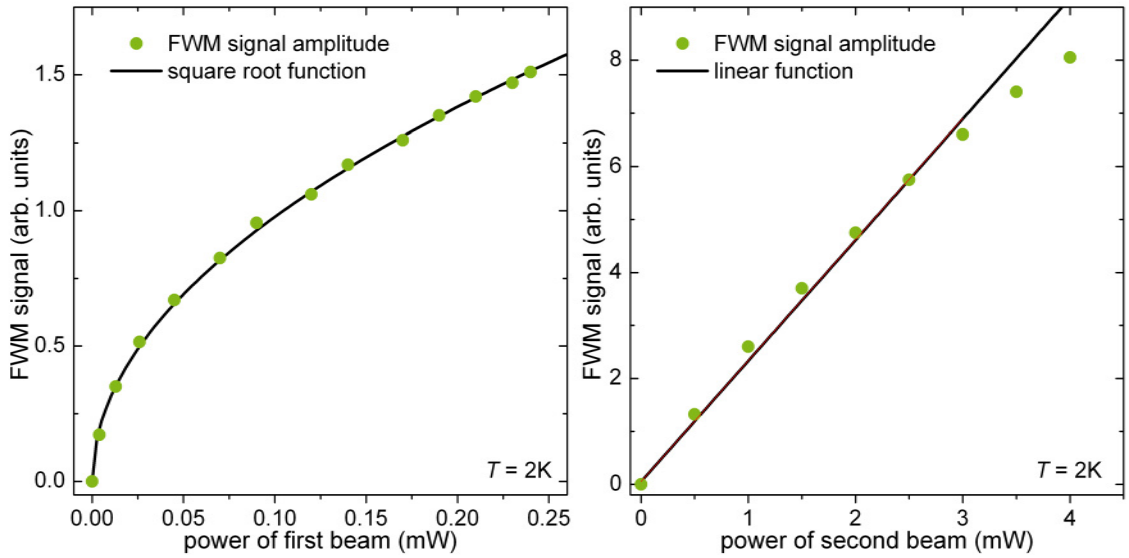

Figure 6.2 Power dependence of the four-wave-mixing signal amplitude on the excitation power. Left: The dependence on the power of the first pulse is expected to show a square-root behavior. Right: The dependence on the power of the second pulse is expected to be linear.

Since $E \propto \sqrt{I}$, a square-root dependence on the intensity of the first excitation beam is expected – and confirmed by experiment. For the second excitation beam, a linear dependence is observed for excitation powers of $P_2 < 4\,\mathrm{mW}$ – as expected. For higher powers, the measurement deviates from the linear dependence, indicating the onset of nonlinear effects. The restriction of the pulse intensity (and thereby the pulse area) leads to only a partial photon echo, meaning that not all excited oscillators partake in the echo process as shown in Fig. 2.5. Nevertheless, a clear photon echo is observed as will be shown in the following.

6.3 Spontaneous photon echo

The time dependence of the photon echo is measured according to the procedure described in Subsec. 3.4.3. Exemplary results are shown in Fig. 6.3. The colored curves show reference scans for different time delays τ_{12}, resolving the photon echo profile. Note that the maximum of the signal is observed at $\tau_{\mathrm{ref}} = 2\tau_{12}$, which is a unambiguous indication for the emission of a photon echo. By performing a synchronous scan of both the τ_{12} delay and the τ_{ref} time (black curve), the decay of the photon echo signal can be measured as a function of τ_{12}. This is the mode of

measurement used for the results discussed in the following. For the stimulated echo in Sec. 6.4, the delay τ_{23} is scanned synchronous with τ_{ref}. For very small delays τ_{12} (e.g. blue curve), a FWM signal is observed due to the direct interaction of the second laser pulse with the macroscopic polarization that was excited by the first pulse. The ensemble is not dephased in this case and the signal is called free polarization decay (see Subsec. 2.2.3).

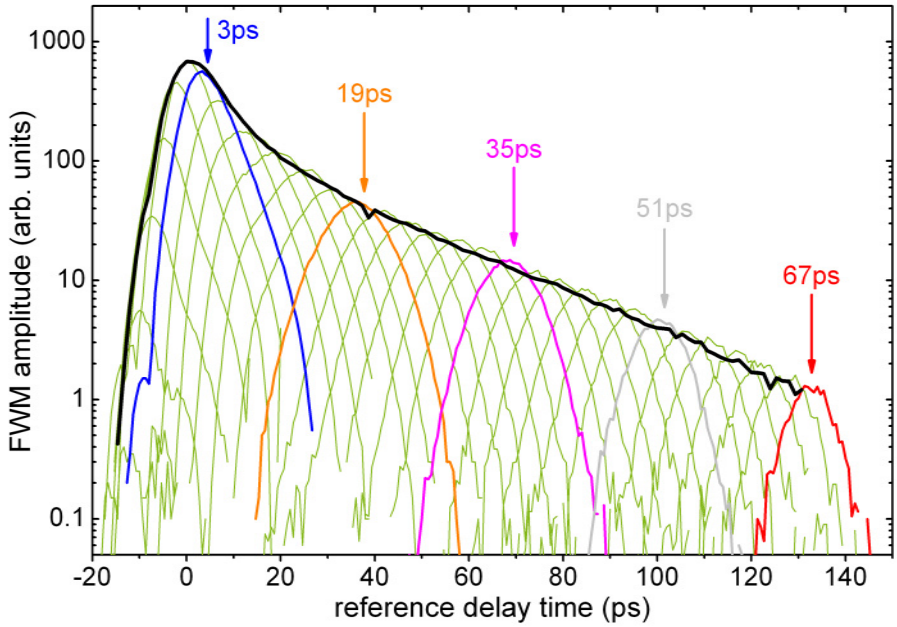

Figure 6.3 Spontaneous photon echo signals for different time delays τ_{12}. When the delay of the reference pulse is scanned while τ_{12} is fixed, the profile of the photon echo can be resolved (colored curves). The maximum of the photon echo occurs at twice the delay between the first and the second pulse – for some curves, the corresponding τ_{12} times are shown near the arrows. In order to measure the decay constant of the photon echo, it is sufficient to scan the delay of the reference pulse at twice the rate of τ_{12} (black curve).

For the determination of the decay time of the spontaneous photon echo, the polarization is chosen to be σ^+ for all beams and the time τ_{12} is increased in steps of 1/3 ps, which corresponds to a step size of the delay line of 0.05 mm. The resulting signal is shown in Fig. 6.4. A fit with an exponential decay (see Eq. (2.21)) yields a coherence time of $T_2 = (69.4 \pm 0.2)$ ps. Coherence times on this order of magnitude have been reported before for trions in CdTe quantum wells [208].

As described in Subsec. 2.2.4, the first laser pulse excites a coherent superposition of the ground state and the excited state. With the ground state being the resident electron and the excited state being the trion, the selection rules discussed in Subsec. 2.2.5 (see Fig. 2.8) apply. In the case of σ^+-polarized light, only the transition from the $m_s = +1/2$ ground state to the $m_j = +3/2$ excited state (left pair of states

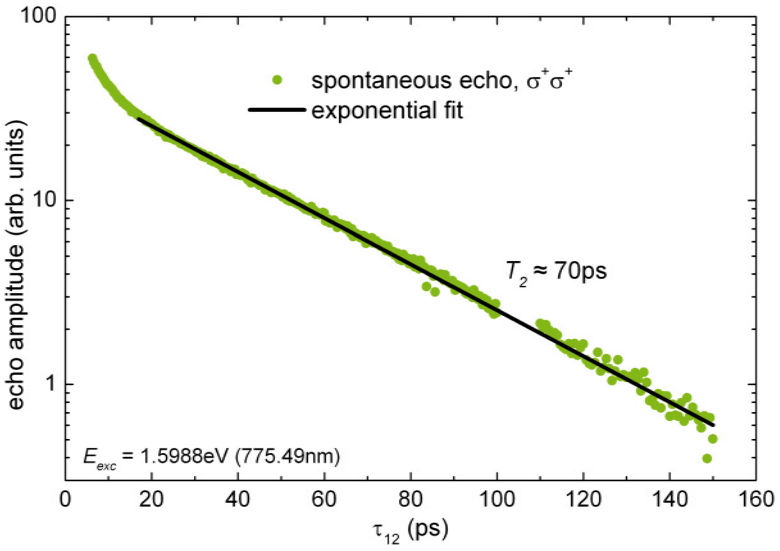

Figure 6.4 Decay of the spontaneous photon echo under circularly polarized polarization. The exponential fit (black curve) exhibits a decay constant of $T_2 = 70\,\mathrm{ps}$.

in Fig. 2.8 is driven. The same selection rules are also valid for the subsequent laser pulse. Only if the later pulse is polarized in such a way, that the selection rules allow an interaction with the coherence excited by the first pulse, the rephasing process and the photon echo emission can take place. If the subsequent pulse cannot interact with the induced coherence, no rephasing process can be induced and no photon echo signal can be observed. The manipulation of the induced coherence therefore grants access to the control of photon echoes.

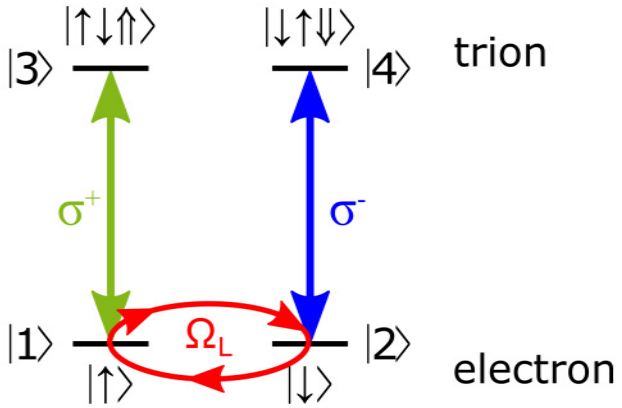

Figure 6.5 Level-scheme of the electron-trion system with the transverse magnetic field coupling the electron spin projections of the ground state.

This is achieved by the application of an external magnetic in Voigt geometry. The magnetic field induces a Larmor precession of the resident electron's spin, thereby

coupling the $|\uparrow\rangle$ and $|\downarrow\rangle$ eigenstates of the electron-trion-system's ground state (see Fig. 6.5). The excited state is not affected because the electrons in the trion complex form a spin singlet state that has no (effective) magnetic moment and the transverse Landé factor of the hole is very close to zero [209]. With this coupling, the optically induced polarization can be manipulated without being restricted to the selection rules.

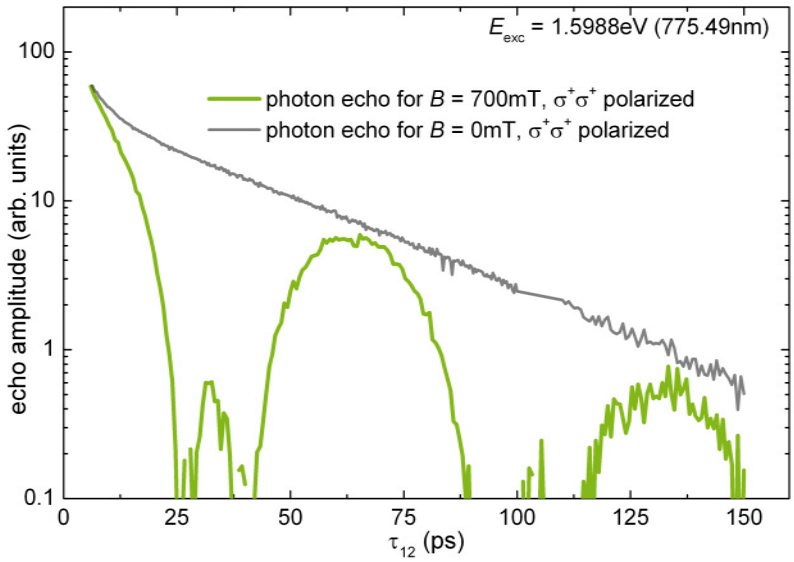

Figure 6.6 Decay of spontaneous photon echo under circularly polarized excitation. The transverse magnetic field induces oscillations of the echo signal.

Figure 6.6 shows the decay of the spontaneous photon echo signal P_{PE} with circularly polarized excitation in the presence of a constant magnetic field with $B = 700\,\mathrm{mT}$ in Voigt geometry.

The signal shows the exponential decay that was already seen for the measurement in zero magnetic field. Additionally, oscillations can be observed that are attributed to Larmor precession. In order to investigate these further, the exponential decay is erased by dividing by the signal that was measured in zero magnetic field. The resulting oscillatory part of the signal

$$R = |P_{\mathrm{PE}}(\tau_{12}, B)|/|P_{\mathrm{PE}}(\tau_{12}, B = 0)| \tag{6.1}$$

is shown in Fig. 6.7, together with a fit according to Eq. (6.3) (see below). The values of $|g_{e,\perp}| = 1.52 \pm 0.01$ ($|g_{h,\perp}| = 0.18 \pm 0.01$) for the Landé factors of the electron (hole) are in good agreement with previously published measurements in the same sample [210] and similar samples [211].

The reason for the oscillatory behavior of the photon echo signal can therefore be identified as the Larmor precession of the electron spin.

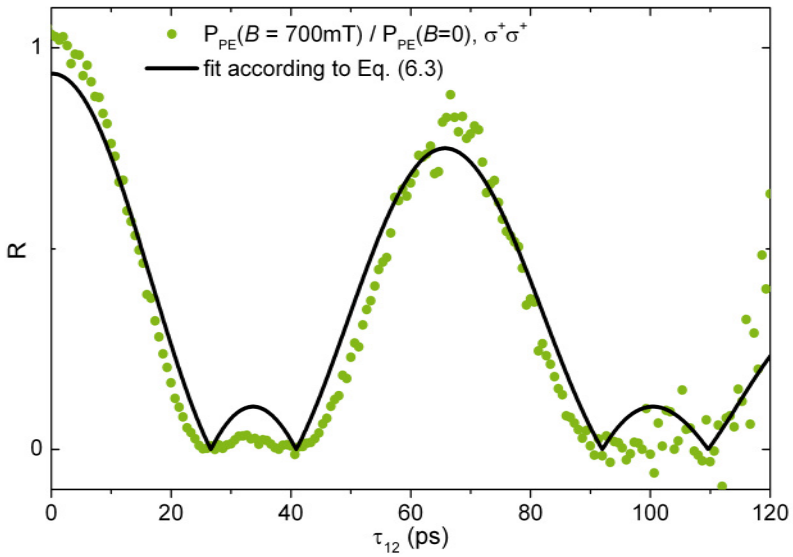

Figure 6.7 Oscillatory part R of the spontaneous photon echo under circular excitation in a transverse magnetic field of $B = 700\,\mathrm{mT}$. The fit (black curve) is according to Eq. (6.3).

The process can be described as follows: The first pulse creates a coherent superposition of electron state $|1\rangle$ and trion state $|3\rangle$. During the pulse action, the magnetic field can be disregarded, since $\tau_p \ll T_L$. The coherence is then subject to dephasing as well as to the action of the magnetic field, rotating the spin of the electron ground state. After half a Larmor precession ($t = T_L/2$) the spin direction is reversed, meaning that the optically induced coherence is transferred into a superposition of states $|2\rangle$ and $|3\rangle$. As can be seen from Fig. 2.8, the transition between $|2\rangle$ and $|3\rangle$ is optically inaccessible. If the second pulse arrives at this time ($\tau_{12} = T_L/2$), the interaction will not lead to a rephasing of the coherence. Hence no photon echo can be generated and the signal drops to zero. This situation repeats itself whenever $\tau_{12} = (2n-1)T_L/2$.
When one or more full Larmor precession are completed ($t = nT_L$), the spin direction is returned into the original state and the coherence that was excited by the first pulse is again optically accessible. If the second pulse arrives at these times ($\tau_{12} = nT_L$), the situation is the same as if there was no magnetic field. The second pulse can induce the rephasing and a photon echo is observed.

For the quantitative analysis of the process, it is instructive to model the density matrix $\rho(t)$. For the system under study, the density matrix is a 4x4 matrix that represents the coherent superpositions of the quantum mechanical states presented in Sec. 2.2 and Fig. 2.8. The diagonal elements ρ_{kk} represent populations of electrons ($k = 1, 2$) or trions ($k = 3, 4$), while the off-diagonal elements ρ_{kl} stand for coherent superpositions of electron- and trion-states.[1]

[1]Note that the indices of the density matrix change with respect to Subsec. 2.2.2, since here

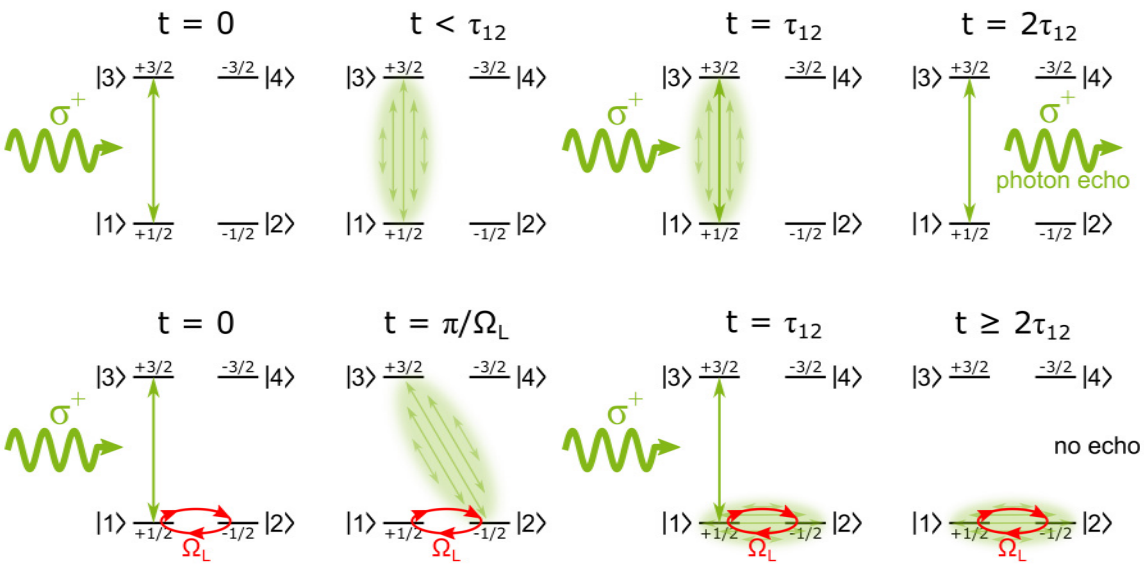

Figure 6.8 Process of the spontaneous photon echo in the electron-trion system under circularly polarized excitation. Top row: without magnetic field, bottom row: with magnetic field and $\tau_{12} = \pi/\Omega_L$.

The results presented in the following were achieved by Dr. Irina Yugova and published in the supplementary material of [212] and [213]. The model uses a semi-classical approach.

With several assumptions for a mathematical simplification of the problem, the time evolution of the density matrix can be modeled analytically. The assumptions

a) Pulse duration τ_p is short compared to trion lifetime T_1, decoherence time T_2, and electron precession time T_L; pulses are approximated with a rectangular function

b) Trion recombination time is short compared to the laser repetition time

c) The laser wavelength is large compared to the length scale of localization (dipole approximation)

d) The excitation of the quantum wells is in the linear regime (pulse area < 1)

e) The charge carrier concentration is low, there is no interaction of trions

f) All other excited states are disregarded

are in agreement with the conditions under which the experiments were conducted.

effectively *two* two-level system are described and the optical couplings are covered by ρ_{13} and ρ_{24} (see Fig. 2.8)

In this scope, the density matrix can be tracked through time, calculating the evolution of the elements of $\rho(t)$ sequentially, considering the interaction with polarized laser pulses and a magnetic field and taking into account the damping processes.

The calculation of the spontaneous echo under right-handed circular polarized excitation in a transverse magnetic field can be found in Appendix A and yields

$$P_{\mathrm{PE}}^{\sigma^+\sigma^+} \propto \rho_{13} \propto \exp(-2\tau_{12}/T_2)\frac{1+\cos(\Omega_L\tau_{12})}{2}\frac{1+\cos(\Omega_L^H\tau_{12})}{2}. \tag{6.2}$$

The oscillatory part as shown in Fig. 6.7 is hence

$$R^{\sigma^+\sigma^+} = \frac{1+\cos(\Omega_L\tau_{12})}{2}\frac{1+\cos(\Omega_L^H\tau_{12})}{2}. \tag{6.3}$$

6.3.1 Linearly polarized excitation

The experiment is repeated with linearly polarized excitation, driving both the $|1\rangle \rightarrow |3\rangle$ and the $|2\rangle \rightarrow |4\rangle$ transition. The phase between the right- and left-handed part of the excitation determines the direction of linear polarization. In the experiment, two configurations are used. In both cases, the first pulse is polarized parallel to the optical table. This direction is denoted "horizontal" (H). The second pulse is either polarized parallel (H) or orthogonal ("vertical", V) to the first one. Both transients are shown in Fig. 6.9 and exhibit the same time constant of $T_2 \approx 70\,\mathrm{ps}$.

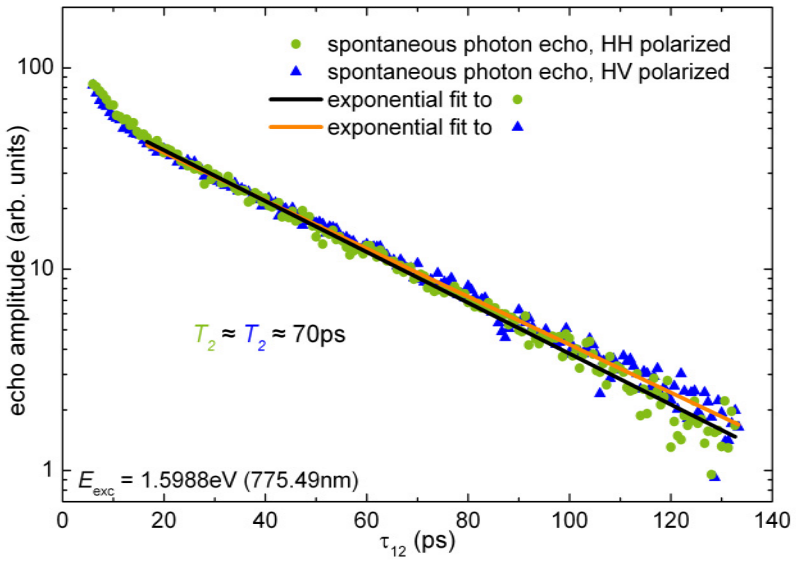

Figure 6.9 Decay of the spontaneous photon echo signal under linearly polarized excitations. For both configurations – parallel (HH) and orthogonal (HV), the time constant is the same.

This confirms that the coherence time is independent from the polarization. However, the influence of a transverse magnetic field is expected to differ strongly for different polarization configurations.

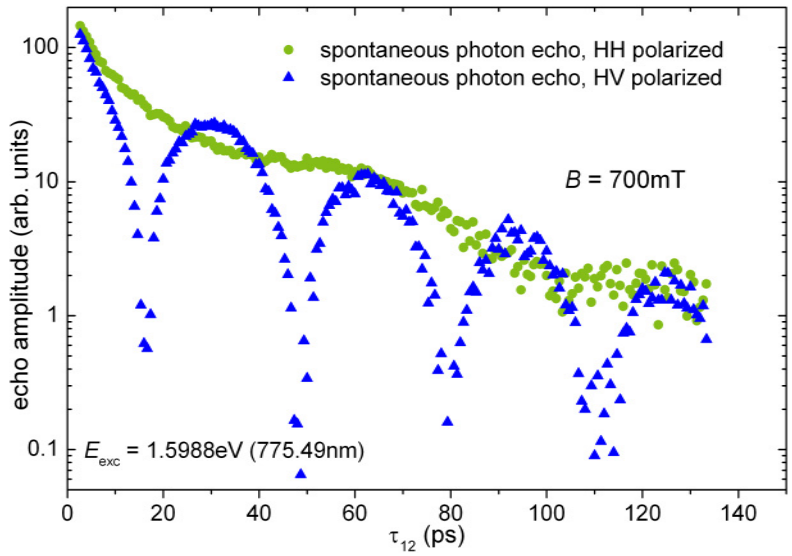

Figure 6.10 Decay of spontaneous photon echo under linearly polarized excitation. For the two linear polarization configurations, the spontaneous photon echo signals behave differently. The transverse magnetic field of 700 mT induces distinct oscillations for orthogonal (HV) polarization (blue triangles), but only marginal oscillations for parallel linear (HH) polarization.

Figure 6.10 displays the time dependence of the spontaneous photon echo under linearly polarized excitation in the presence of a transverse magnetic field with $B = 700\,\mathrm{mT}$. In the collinear case (HH), there is no qualitative effect of the magnetic field on the signal. The minute oscillation that can be observed occurs with the same frequency as in the purely circular polarized case and is attributed to a slight ellipticity that is caused by minor imperfections of the polarization optics used during the experiments. Also the modeling of the density matrix confirms the signal to follow

$$P_{\mathrm{PE}}^{HH} \propto \exp(-2\tau_{12}/T_2) \tag{6.4}$$

without oscillations.

In the configuration with crossed linear polarization (HV), marked oscillations can be observed. They show a sharp bend at zero signal which can be explained by the fact that the setup used for the measurements is sensitive to the absolute value of the polarization. Hence all signals will be displayed as non-negative. In the calculation this is accounted for by using the absolute value.

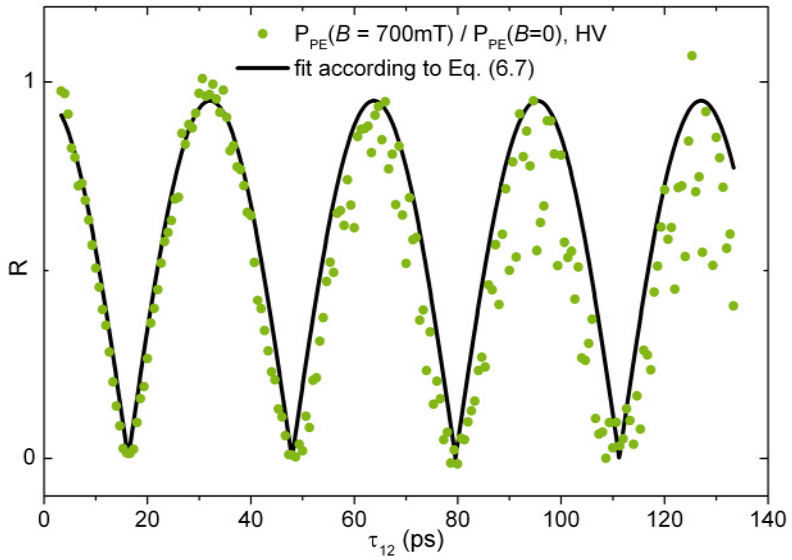

Figure 6.11 Oscillatory part R of the spontaneous photon echo under crossed linear (HV) excitation in a transverse magnetic field of $B = 700\,\mathrm{mT}$. The fit (black curve) is according to Eq. (6.7).

The oscillatory part of the signal is again isolated by calculating

$$R = |P_{\mathrm{PE}}(\tau_{12}, B)|/|P_{\mathrm{PE}}(\tau_{12}, B = 0)|. \tag{6.5}$$

It is shown in Figure 6.11 along with a curve that results from the same theoretical approach as discussed above. For crossed linear excitation, a photon echo signal of

$$P_{\mathrm{PE}}^{HV} \propto |\exp(-2\tau_{12}/T_2) \cos\Big((\Omega_L - \Omega_L^H)\tau_{12}\Big)| \tag{6.6}$$

is expected. Accordingly, the oscillatory part follows

$$R^{HV} = |\cos\Big((\Omega_L - \Omega_L^H)\tau_{12}\Big)|. \tag{6.7}$$

In the time-resolved experiment, the frequency of the oscillation is determined by the difference in Larmor frequencies of the electron Ω_L and the hole Ω_L^H. Consequently, only the difference in Landé factors $|g_e - g_{h,\perp}| \approx 1.7$ is accessible experimentally, confirming the results extracted from circularly polarized excitation. The derivation of Eq. (6.6) is presented in detail in Appendix A.

The oscillations are characterized by the product of the (effective) Larmor frequency Ω_L and the delay time τ_{12}. In addition to changing the time delay, as discussed above, the Larmor frequency $\Omega_L = |g|\frac{\mu_B}{\hbar}B$ can be scanned by sweeping the external magnetic field B. The spontaneous photon echo signal should again show oscillations that are compatible with the model. Figure 6.12 shows the magnetic field dependence of the photon echo amplitude (open symbols) for different,

but fixed delay times τ_{12} in crossed linear (HV) polarization. The solid lines follow Eq. (6.7).[2]

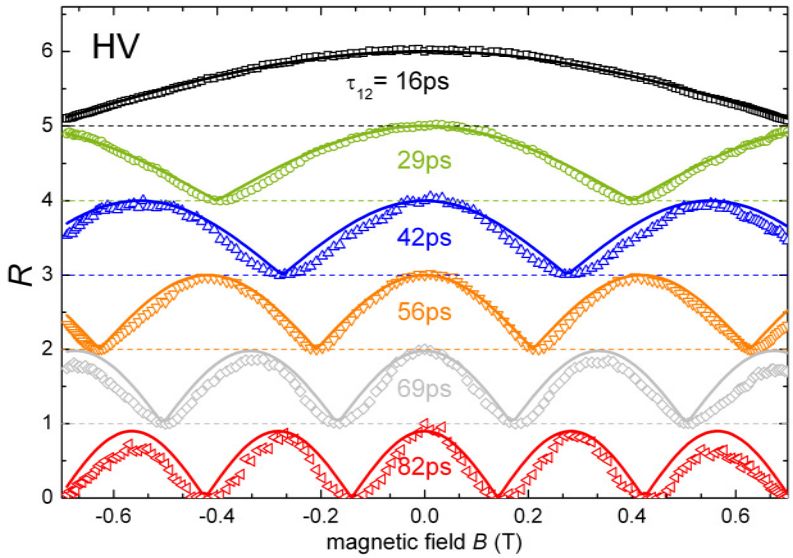

Figure 6.12 Magnetic field dependence of the oscillatory part of the spontaneous photon echo signal in crossed linear polarization configuration for different time delays τ_{12}.

Experiment and theory are in full agreement, confirming that the oscillations of the spontaneous photon echo signal are caused by the magnetic-field-induced Larmor precession of carrier spins. The modeling of the optically excited coherence can describe the measured signals quantitatively.

A further inspection of the coherence tracked by the density matrix reveals that even when the second pulse arrives at a time when the system is in an optically inaccessible state, some interaction does take place, converting the optically excited coherence into a *spin* coherence. In order to verify this finding experimentally, the experiment is extended by an additional laser pulse, entering the regime of *stimulated photon echoes*. The findings are discussed in detail in Subsec. 6.4.

6.3.2 Spectral dependence of T_2

In Sec. 6.1 it was shown that the four-wave-mixing amplitude (and hence the photon echo amplitude) depends on the excitation energy (see Fig. 6.1). Additionally, the spectral dependence of the decay time of the spontaneous photon echo, i.e. the coherence time T_2, was investigated. Therefor, the measurement "τ_{12} scan" described in Subsec. 3.4.3 was repeated for different excitation energies. The results are shown in Fig. 6.13.

[2] In this case, the calculation of R is simply a normalization to 1.

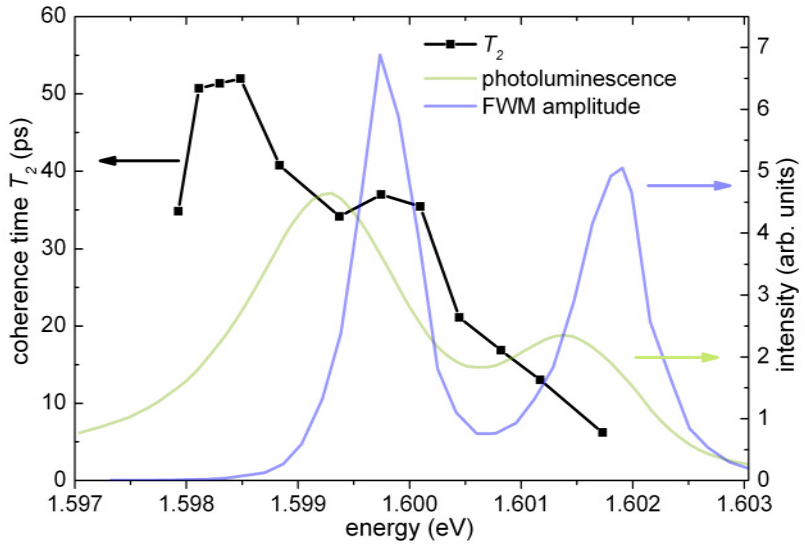

Figure 6.13 Spectral dependence of the time constant T_2 for spontaneous photon echo (black). Highest values are observed for the low-energy flank of the trion transition. The intensities of the photoluminescence (green) and the four-wave-mixing signal (blue) are included for reference.

While the excitation around the exciton resonance results in coherence times on the order of the pulse length, the coherence time of the trion is considerably longer, amounting to some tens of picoseconds. A maximal coherence time is observed for photon energies of 1.5985 eV (775.63 nm) in the low-energy flank of the trion resonance. In this spectral range, the trions feature an enhanced localization which is the basis for the observed dependency. The localization reduces the efficiency of scattering processes, which are the reason for decoherence. Therefore the coherence time T_2 is extended.

6.4 Stimulated photon echo

The field-induced oscillations in the spontaneous photon echo signal as well as the theoretical modeling of the density matrix evidence an involvement of the spin in the photon echo process in the studied system. By the application of an additional laser pulse and the investigation of the stimulated photon echo, it is possible to investigate the involvement of spin optically.

According to Eq. (2.23), the lifetime of the optical transition can be measured by scanning the stimulated photon echo amplitude in dependence of the delay τ_{23} between the second and the third pulse. The procedure is described in detail in "τ_{23} scan" in Subsec. 3.4.3.

The measurement was repeated for three different polarization configurations:

circular polarizations with all beams having the same helicity ($\sigma^+\sigma^+\sigma^+$), collinear polarization (HHH) and crossed linear polarization, in which the first pulse is polarized perpendicular to the others (HVV).

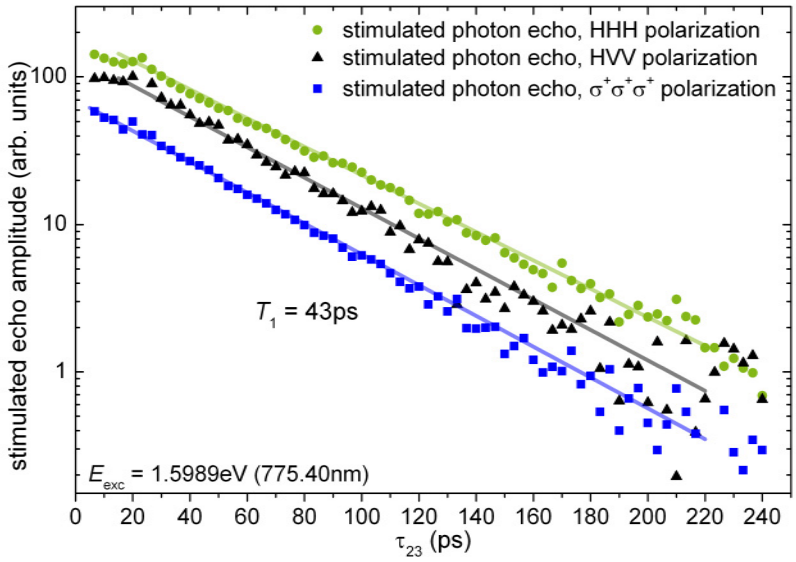

Figure 6.14 Decay of the stimulated photon echo signal under circularly and linearly polarization configurations. All transients show the same time constant of $T_1 = 43\,\mathrm{ps}$.

Exponential fits with

$$P_{\mathrm{SPE}} \propto \exp(-\tau_{23}/T_1) \tag{6.8}$$

to all three curves are displayed with solid lines in figure 6.14. For all configurations, the experiment reveals the same time constant of $T_1 \approx 43\,\mathrm{ps}$. This is consistent with Eq. (2.20) and indicates that the dominant mechanism for the decay of the signal is the recombination of the trion, since $T_2 \approx 2T_1$ and not $T_2 \ll 2T_1$.

6.4.1 $\sigma^+\sigma^+\sigma^+$ polarized excitation in magnetic field

Until the second pulse, the excitation scheme for the stimulated photon echo is the same as that of the spontaneous photon echo discussed in Sec. 6.3: The first pulse creates a coherent superposition of $|1\rangle$ and $|3\rangle$ which is then subject to dephasing and to the action of the magnetic field. The same is true for the magnetic field induced perpetual alternation between optically accessible state ρ_{13} and optically inaccessible state ρ_{23} before the arrival of the second pulse.

However, the time of arrival of the second laser pulse relative to the phase of the Larmor precession of the electron now not only determines whether a spontaneous photon echo is emitted or not. The exact modification of the optically excited coherence can be further investigated due to the disposal of a third laser pulse.

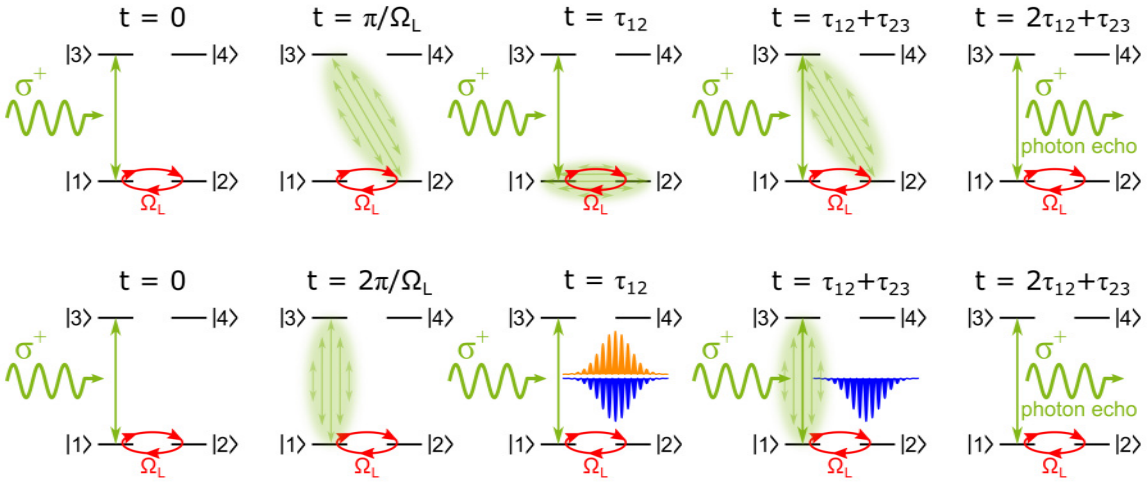

Figure 6.15 Stimulated echo process in electron-trion system. Top row: magnetic field and pulse-delay are such that $\tau_{12} = \pi/\Omega_L$, bottom row: magnetic field and pulse-delay are such that $\tau_{12} = 2\pi/\Omega_L$.

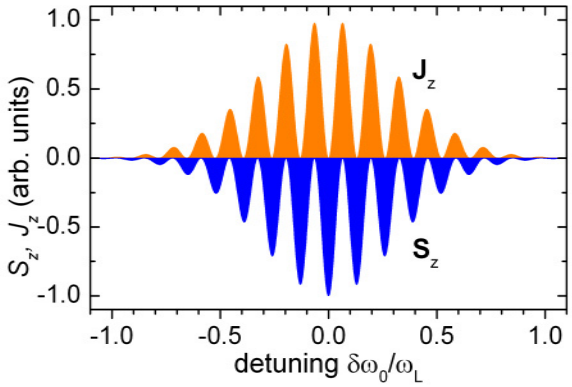

Figure 6.16 Fringes for electron (blue) and hole (orange) spins resulting from two laser pulses acting coherently on the same transition.

The action of the second pulse results in the transfer of the optically excited coherence into the spin state of the studied system. This transfer is governed by two effects whose relative importance depends on the time of arrival of the second laser pulse relative to the Larmor precession of the electron.

The first effect is dominant when the second pulse arrives after an odd multiple of half Larmor rotations, i.e. $\tau_{12} = (2n-1)T_L/2$. The coherent superposition that was excited by the first pulse is then in the state described by ρ_{23}. The laser pulse acts on the transition $|1\rangle \rightarrow |3\rangle$ and transfers (part of) the coherence into a superposition of states $|1\rangle$ and $|2\rangle$. In this condition no spontaneous photon echo can be observed since the coherence is not in an optically accessible state but was shifted to a spin coherence described by ρ_{12}. Consequently the decoherence is no longer governed by

optical processes, having relatively short time constants in the range of picoseconds (as seen in Sec. 6.3), but is determined by the electron spin coherence time T_2^e in the range of nanoseconds (see [210] and below). By the use of a third pulse and again exploiting the effect of the magnetic field, it is possible to convert the spin coherence back into an optical coherence which can then emit a photon echo. This is achieved by reversing the procedure used before: the third optical pulse, again acting on the transition $|1\rangle \rightarrow |3\rangle$, converts the spin coherence into a coherence of the states $|2\rangle$ and $|3\rangle$ (ρ_{23}). Then the Larmor precession of the spin leads to an optical coherence of states $|1\rangle$ and $|3\rangle$. Due to the specifics of the excitation scheme ($\tau 12 = (2n-1)T_L/2$), the rephasing of the ensemble is complete just as the coherence is shuffled back into the optically accessible state and a stimulated photon echo is emitted.

The second process is dominant for $\tau_{12} = nT_L$, when the second laser pulse arrives after a number of full Larmor rotations. It is pictured in Fig. 6.15 (bottom row) and involves the excitation of spectral population gratings.

As before, the first pulse creates a macroscopic polarization and a coherent superposition of electron and trion. Between the first and the second pulse, the excited coherence is subject to dephasing due to the inhomogeneous broadening of the ensemble of dipoles. Every dipole thereby picks up a phase that is defined by the detuning $\delta\omega_0 = \omega - \omega_0$ of the dipole's eigenfrequency ω from the laser frequency ω_0. Upon the arrival of the second pulse ($\tau_{12} = nT_L$), the system is again in an optically accessible state described by ρ_{13}. Depending on the phase that every individual dipole accumulated during τ_{12}, the second laser pulse projects the coherent state into a population state, either of the electron ρ_{11} or the trion ρ_{33}. This results in spectral population gratings [98] for the electron and the trion state with opposite phase that are given by

$$\rho_{11} \propto \sin^2(\delta\omega\tau_{12}/2) \qquad \rho_{33} \propto \cos^2(\delta\omega\tau_{12}/2). \tag{6.9}$$

Due to the selection rules, the excitation with circularly polarized light connects a population with a spin orientation. The population gratings of the electrons and trions are therefore equivalent with fringes of electron spins ($S_z = (\rho_{11} - \rho_{22})/2$) and hole spins ($J_z = (\rho_{33} - \rho_{44})/2$), respectively. They are illustrated in Figure 6.16.

Since the external magnetic field acts differently on electrons and trions, the two gratings are desynchronized.[3] The Larmor precession of the electrons along with the lack of Larmor precession of the trions prevents the annihilation of the gratings, even beyond trion recombination.

At the incidence of the third laser pulse, the electron grating is still present and interacts with the laser pulse. As the grating is a consequence of the coherent

[3] The non-existence of the echo for zero field is due to the annihilation of the gratings during recombination. In principle, a desynchronization could also come from a spin decoherence during the trion lifetime. But this is not the case here since the spin coherence time is much longer than the trion lifetime ($T_e, T_h \gg T_1$) [210, 213]

excitation by the precedent two pulses, it still carries the phase information that is necessary to create a stimulated photon echo [213]. Indeed, this phase information is stored in an electron spin coherence, rather than in an optically accessible state. This means that the decay of the signal between the second and third pulse is determined by the electron spin coherence time T_2^e. In previous studies spin relaxation times of 30 ns [214–216] were found.

Both processes represent the transfer of optically excited coherence from the electron-trion state into the spin state of the resident electron. For circularly polarized excitation and arbitrary τ_{12}, both processes occur in conjunction and therefore all spin components contribute to the spontaneous photon echo signal. A distinction is not possible under these circumstances. Moreover, one of the assumptions for the modeling was the absence of spin polarization before the first laser pulse. For circularly polarized excitation, this initial condition of $\rho_{11} = \rho_{22} = 1/2$ is not fulfilled. Circularly polarized excitation induces a macroscopic spin polarization which decays with the electron spin relaxation time $T_2^e \approx 30\,\text{ns}$. This relaxation time is longer than the pulse repetition period of the laser excitation (13.2 ns) which means that upon the arrival of a laser pulse, the spin polarization that was induced by the preceding laser pulse has not yet vanished.

Consequently, it must be stated that circularly polarized excitation is not optimal for the investigation of the magnetic-field-induced stimulated photon echo. Linearly polarized excitation not only prevents a macroscopic spin polarization, it also involves only the dephasing-free S_x component of the electron spin in the generation of the stimulated photon echo (see Eq. (B.36) in Appendix B).

6.4.2 Linearly polarized excitation in magnetic field

As for the case without magnetic field discussed above, two different linearly polarized excitation configurations were used. One collinear polarization (HHH), in which all beams are polarized parallel to each other and one crossed linear polarization (HVV), in which the first pulse is polarized perpendicular to the others.

The result of the measurement for (HHH) polarized excitation and a transverse magnetic field with $B = 700\,\text{mT}$ is shown in Fig. 6.17. The stimulated photon echo signal remains at a sizeable amplitude throughout the entire measurement window of 1200 ps (green circles). When the magnetic field is switched off, the signal drops to zero within 250 ps (grey circles, compare also Fig. 6.14).

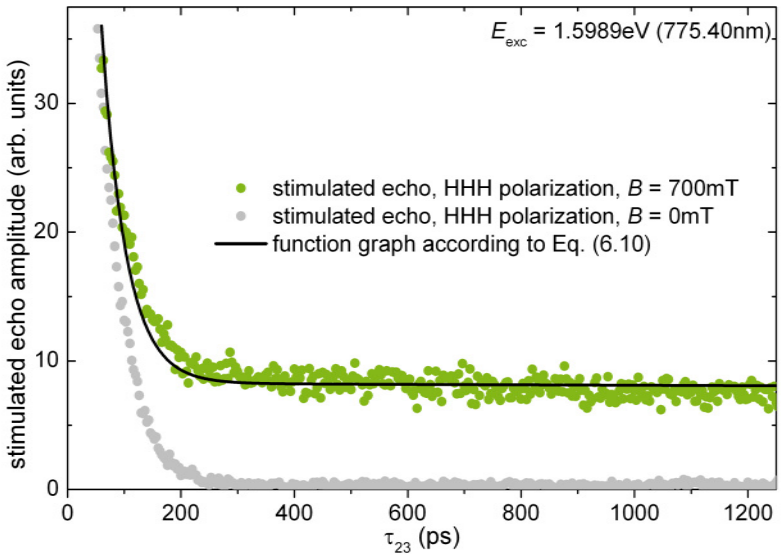

Figure 6.17 Effect of the magnetic field on the stimulated photon echo in HHH polarized excitation. The black curve is according to Eq. (6.10) with only amplitude as fitting parameter.

The black line in Fig. 6.17 follows

$$\begin{aligned} P_{HHH} \propto & \exp\left(-\frac{\tau_{23}}{T_1^e}\right) \sin^2\left(\frac{\Omega_L \tau_{12}}{2}\right) \\ & + \exp\left(-\frac{\tau_{23}}{T_1}\right) 2\cos^2\left(\frac{\Omega_L \tau_{12}}{2}\right) \\ & + \exp\left(-\frac{\tau_{23}}{T_1}\right) \exp\left(-\frac{\tau_{23}}{T_h}\right) \sin^2\left(\frac{\Omega_L \tau_{12}}{2}\right), \end{aligned} \tag{6.10}$$

which is derived from the same model as for the spontaneous echo. The calculations are presented in Appendix B. The dynamic parameters were taken from the literature or from the previous measurements; the only fitting-parameter is the constant of proportionality. Theory and experiment concur, demonstrating the transfer of optically excited coherence into the spin state of the resident electron and the subsequent retrieval as an optical pulse by means of the stimulated photon echo.

The decisive role of the external magnetic field can be elucidated by scanning its value for fixed delay times τ_{12} and τ_{23}. In the collinear case, no oscillations are expected as was already observed for the variation of the delay time τ_{23} (see Fig. 6.17). Instead, the magnetic field enables the storage of the optical information in spectral interference fringes (see Fig. 6.16) by preventing the annihilation of electron and trion fringes upon trion recombination. This is achieved by the desynchronization of the two fringes through Larmor precession at different frequencies for electron and trion.

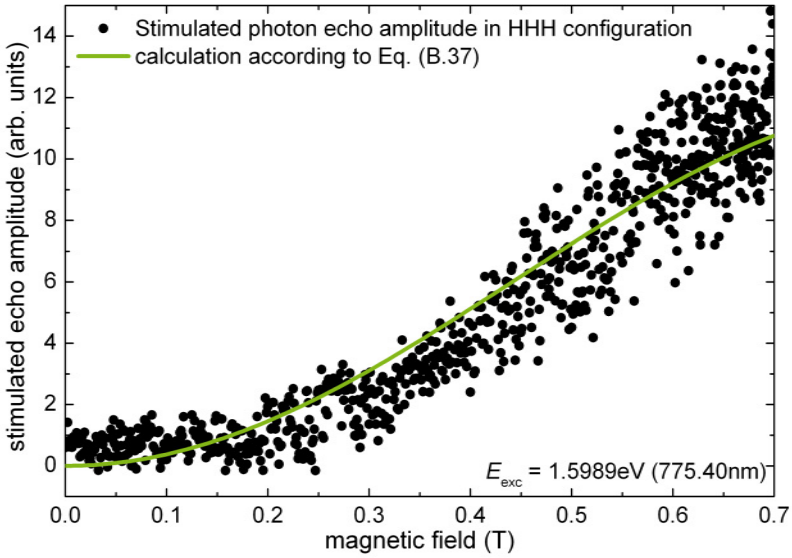

Figure 6.18 Magnetic field dependence of the stimulated photon echo for collinear polarized excitation. The long-lived photon echo for $\tau_{12} = 27\,\text{ps}$ and $\tau_{23} = 1.27\,\text{ns}$ is only observed in the presence of a transverse magnetic field.

The desynchronization is more efficient for faster rotation, so that the monotonous increase with rising magnetic field measured in experiment (see Fig. 6.18) can be understood also intuitively. The calculated curve (green in Fig. 6.18) follows Eq. (B.36). Experiment and calculation agree, evidencing the crucial role of the magnetic field for the storage of optically excited coherence in the spin state of the resident electron of the CdTe quantum well.

The results for time-resolved measurement of the stimulated photon echo for crossed linear excitation (HVV) are shown in Fig. 6.19. For nonzero magnetic field[4] (green circles), the photon echo amplitude shows distinct oscillations throughout the entire measurement window of 1200 ps. The sharp bends at zero signal are attributed to the same conjuncture as for spontaneous photon echoes (compare Fig. 6.10): the measurement setup records all signals as non-negative. Without magnetic field, the signal vanishes within 250 ps (grey circles, compare also Fig. 6.14).

The black line in Fig. 6.19 obeys

$$\begin{aligned} P_{HVV} \propto & \exp\left(-\frac{\tau_{23}}{T_2^e}\right)\cos\left(\Omega_L\left(\tau_{12}+\tau_{23}\right)\right) \\ & + \exp\left(-\frac{\tau_{23}}{T_1}\right)\cos(\Omega_L\tau_{12}), \end{aligned} \tag{6.11}$$

[4] In contrast to the previous graphs, here the measurement in a magnetic field of $B = 150\,\text{mT}$ is shown. For the sake of clarity, the number of oscillations within the measurement window had to be limited. All measurements were repeated for several different magnetic fields and all conclusions hold for all fields.

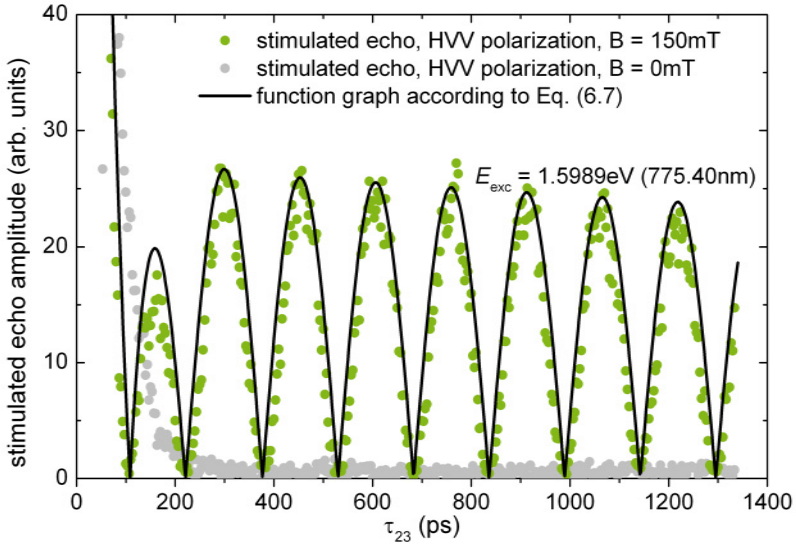

Figure 6.19 Effect of the magnetic field on the stimulated photon echo in HVV polarized excitation. The black curve is according to Eq. (6.11) with only amplitude as fitting parameter.

with the constant of proportionality being the only fitting-parameter. Equation (6.11) is derived from the same semiclassical model already introduced in Subsec. 6.3. Detailed calculations are given in Appendix B. The calculated curve reproduces the experimental data, evidencing the retrieval of optically excited coherence from the spin state of the resident electron.

As already observed for the spontaneous photon echo in Subsec. 6.3.1, the field-induced oscillations of the photon echo signal are described by trigonometric functions with the product of Larmor frequency and delay time as their argument. This is also the case for the stimulated echo for crossed linear (HVV) polarization, as Eq. (6.11) shows. Accordingly, for a varied external magnetic field and fixed time delays, the same oscillations should be observable. The measurements shown in Fig. 6.20 confirm this expectation.

Furthermore, the measured signal (black) and the calculated curve (green) show excellent agreement. This again confirms the involvement of spin in the echo process and reinforces the validity of the model.

The observation of stimulated photon echo signals at long delay times between second and third pulse of $\tau_{23} = 1.27\,\mathrm{ns}$ indicates the transfer of optically excited coherence into the spin coherence of the resident electron and back. Due to the particular pulse sequence of the stimulated photon echo process, this finding can be interpreted as a coherent storage of optical information. In this interpretation, the first laser pulse (“write”) contains the information that is to be stored. The second

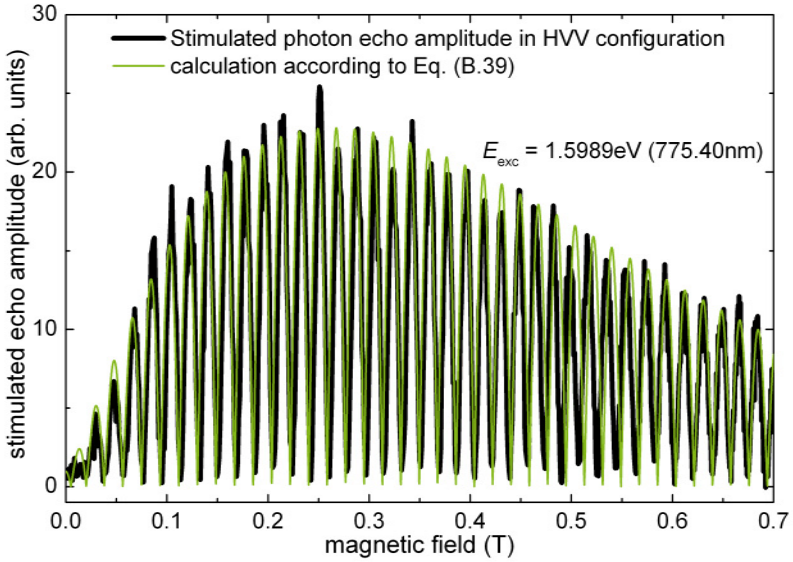

Figure 6.20 Magnetic field dependence of the stimulated photon echo for crossed linear polarized excitation. The oscillations of the measured curve (black) evidence Larmor precession and confirm the model for the calculations (black). The delay times were chosen $\tau_{12} = 27\,\text{ps}$ and $\tau_{23} = 1.27\,\text{ns}$.

laser pulse takes the function of a "store" command, transferring the volatile optical coherence into the robust spin coherence of the electron state. The third pulse then acts as the "read-out", providing the information in the original, optical form, long after the expiration of all optical decay times.

6.4.3 Spectral dependence of T_1

The lifetime T_1 of the stimulated photon echo signal was measured for different excitation energies by scanning the delay between the second and the third laser pulse, as described in "τ_{23} scan" in Subsec. 3.4.3. The measured spectral dependence shown in Fig. 6.21 resembles the spectral dependence of the coherence time T_2 measured for the spontaneous photon echo in Subsec. 6.3.2.

The maximum for the lifetime T_1 is observed for photon energies of 1.5985 eV (775.63 nm), the same value at which the maximum of T_2 was found (compare Fig. 6.13). In the case of the coherence time T_2, this was explained by the enhanced localization of trions in the low-energy flank of the photoluminescence spectrum. The same is valid for the lifetime T_1. An increased localization is equivalent to a reduced Bohr radius, which makes a recombination less probable and hence extends the lifetime T_1. Simultaneously, the smaller Bohr radius also reduces the absorption probability which causes the amplitude of the photon echo signal to shrink, making it impossible to further decrease the excitation energy.

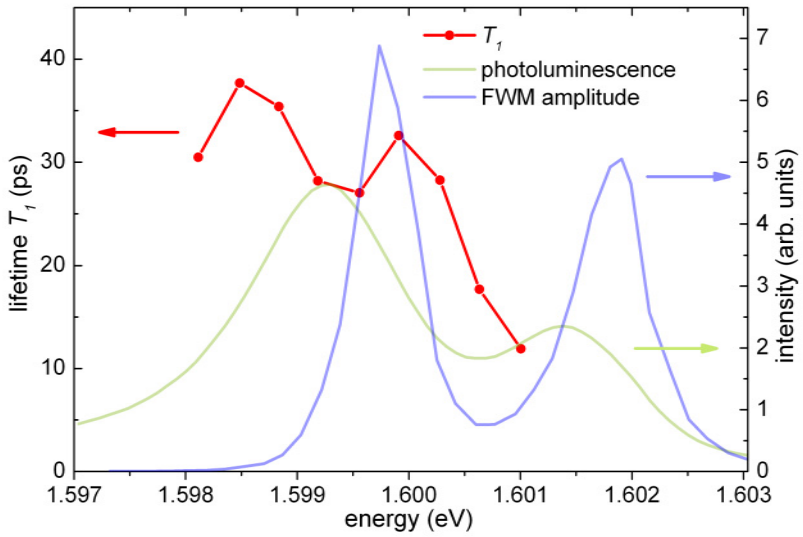

Figure 6.21 Spectral dependence of the time constant T_1 for stimulated photon echoes (red). The highest value is observed for the low-energy flank of the trion transition. The intensities of the photoluminescence (green) and the four-wave-mixing signal (blue) are included for reference.

Furthermore, there is a more profound spectral dependence of the observed effects. The selection rules of the trion play a crucial role in the transfer of coherence between optically accessible states and spin states as discussed above. In particular the fact that the two-level systems driven by polarized light possess individual ground states (see Fig. 6.5) makes it possible to map the coherent superposition of optically coupled states onto a superposition of spin states. Other resonances will therefore not permit any transfer of coherence.

The exciton resonance, for example, is subject to fundamentally different optical selection rules. They are shown in Fig. 6.22.

An external magnetic field does couple the states with opposite spin orientation, but the mutual ground state erases any coherent superposition – optical or spin – upon relaxation. Any manipulation is therefore limited by the lifetime of the excited state.

The spectral separation of excitons and trions is hence essential for the experiment.

6.5 Conclusion

The photon echo is employed to store optically excited coherence in the spin state of the resident electron of a CdTe quantum well. By the application of a transverse magnetic field, a modification of the optical selection rules is induced, that makes

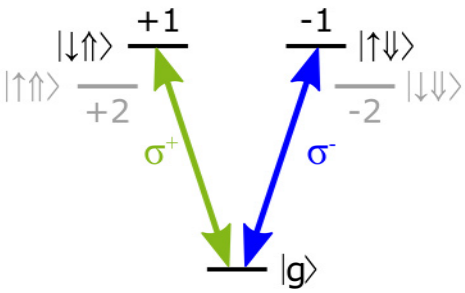

Figure 6.22 Optical selection rules for the exciton and circularly polarized light. The ground state is spin-independent. The optically accessible excited states have angular momenta of $m_j = \pm 1$.

the spin system accessible for coherent optical effects. In this way, the decay time of the stimulated photon echo can be extended by three orders of magnitude.

The unique level scheme of the negatively charged exciton (trion), consisting of two individual two-level systems under circularly polarized excitation (see Fig. 2.8), provides the basis for the optical manipulation of electron spins. The coupling of the two-level systems, that is achieved by the application of a transverse magnetic field, modifies the selection rules such that a transfer of optically excited coherence into the spin state and back becomes possible. In the scope of the 2-pulse experiment of spontaneous photon echo (see Sec. 6.3), the information contained in the first pulse can be transferred into the spin system of the resident electron by the second pulse. This is evidenced by the magnetic-field-induced oscillations of the photon echo signal at the Larmor frequency of the electron spin. A retrieval of the stored information is possible by the application of an additional, third laser pulse, inducing a stimulated photon echo (Sec. 6.4). This third pulse transfers the coherence from the electron spin state back into an optically accessible state. The storage of information is evidenced by the prolongation of the decay time of the stimulated echo signal. Without the involvement of the spin, the decay time of the stimulated echo was measured as $T_1 = 43\,\mathrm{ps}$. Upon the application of a transverse magnetic field and the storage of the optically excited coherence in the spin state, the decay time was found to exceed several nanoseconds, meaning an extension of three orders of magnitude.

7 Summary

The interaction and reciprocal manipulation of polarized light and electron spins in semiconductors was studied with three different approaches.

In Chap. 4 the intra-ion transition of Mn^{2+} ions in CdMnTe is examined. The resonant excitation with circularly polarized light leads to a circular polarization of the photoluminescence of 8 %, evidencing the optical orientation of Mn^{2+} spins. Linearly polarized excitation leads to alignment of the Mn^{2+} spins expressed in a linear polarization of the photoluminescence of 10 %. The existence of polarization is attributed to the suppression of spin depolarization due to the spin glass phase of the studied material. A simple phenomenological model is used to deduce the optical selection rules for the Mn^{2+} intra-ion transition.

The Mn^{2+} ion in CdTe is confirmed as an optically active center and a promising candidate for spintronic applications. In combination with the collective magnetism of the spin glass phase of CdMnTe, it paves the way for optical control and recording of information.

In Chap. 5, a GaAs-based ferromagnet/semiconductor hybrid structure is examined. The influence of the ferromagnetic GaMnAs layer on the charge carriers in the InGaAs quantum well is detected by the circular polarization of the quantum well photoluminescence as well as by the dependence of the photoluminescence intensity on the helicity of the excitation. Both effects show identical hysteresis-like dependencies on the external magnetic field and can be observed for temperatures up to the Curie temperature of the ferromagnetic layer. Moreover, both effects show an identical pronounced time dependence, which is compatible with the time constants typical for electron spins.

Therefore, the spin level splitting due to p–d exchange interaction of holes, that was expected to be the main mechanism of interaction between ferromagnet and semiconductor, is not sufficient to explain the observed effects. Instead, a spin-dependent tunneling of electrons from the quantum well into the ferromagnet is identified as the primary cause for the polarization of the photoluminescence and its dependence on the excitation helicity.

Unlike previously studied spin polarization effects involving a hybrid structure interface [22, 206, 207, 217, 218], the phenomenon discussed here is expected to also take place in insulating structures not specifically designed for electrical spin-injection. This increases the number of potentially suitable materials drastically.

The spin polarization that is induced by the ferromagnet persists up to the Curie temperature of the employed material. Hence with a different choice of the ferromagnetic material, the effect could be observable at elevated temperatures. Excellent prospect for such future investigations is provided by the elements iron, cobalt, and nickel, and by compounds containing manganese, such as MnAs, MnB or MnBi, which exhibit ferromagnetism even above room temperature. Furthermore, the discovery of this unexpected effect exemplifies the open questions in this field and motivates further investigation of hybrid structures for optical spin manipulation.

In Chap. 6, the photon echo and its dependence on an external magnetic field is examined. The photon echo is observed for the excitation of the trion resonance in an n-doped CdTe quantum well. A transverse magnetic field modifies the optical selection rules of the trion transition and grants access to the spin state of the resident electron of the quantum well. In this way, an additional degree of freedom is introduced in the echo procedure, so that the optically excited coherent process can be manipulated by the external magnetic field. The involvement of the spin via the selection rules even allows a transfer of the optical coherence into the spin coherence of the resident electron. The optical retrieval of this coherence is evidenced in the scope of the stimulated photon echo. Due to the considerably longer coherence time of the spin state compared to the optical transition, the transfer of optically imprinted information into the spin state and the subsequent retrieval can be regarded as a storage of the optical information. In the conducted stimulated photon echo experiment, the three laser pulses then take the functions of "write", "store", and "read". The investigated quantum well sample allows an extension of the stimulated photon echo decay time from 43 ps to several nanoseconds, signifying an increase of three orders of magnitude.

The utilization of systems with longer spin coherence times offers the potential to increase this number even further. A prime candidate for such a system are quantum dots which offer an increased localization of the charge carriers (which was already found to be beneficial in Subsec. 6.4.3). An additional benefit comes from the reduced many-body effects that permit higher excitation power densities. The lower absorption probability provided by quantum dots can be further counteracted by placing them in a cavity.
Another way of increasing the coherence time is by using elaborated excitation schemes ([219, 220]) involving additional laser pulses.

A Calculation of the spontaneous photon echo amplitude

As already hinted at in Chap. 6, the modeling of the density matrix ρ of the electron-trion system opens the possibility to track the optically excited coherence through time. The evolution of the density matrix is given by the Lindblad equation

$$\mathrm{i}\hbar\dot{\rho} = \left[\hat{H}, \rho\right] + \Gamma, \tag{A.1}$$

with $\hat{H}$ being the Hamilton operator of the system and Γ describing the relaxation processes phenomenologically. In the Hamilton operator, three contributions need to be considered: the unperturbed spin system, the interaction with the magnetic field and the interaction with the light field. In the short pulse approximation, the pulse duration is considered to be much shorter than the trion lifetime, the decoherence times and the electron spin precession time (Larmor period). This approximation is justified for the experiment discussed in Chap. 6. Under these conditions, the interaction of the electron-trion system with light and its dynamics in the magnetic field can be separated and considered individually. The Hamilton operator can thus be written as $\hat{H} = \hat{H}_0 + \hat{H}_B + \hat{V}$, where $\hat{H}_0$ is the Hamilton operator of the unperturbed system, $\hat{H}_B$ describes the interaction with the magnetic field and

$$\hat{V}(t) = -\int \left(\hat{d}_+(\boldsymbol{r})E_{\sigma^+}(\boldsymbol{r},t) + \hat{d}_-(\boldsymbol{r})E_{\sigma^-}(\boldsymbol{r},t)\right)\mathrm{d}^3r \tag{A.2}$$

accounts for the interaction with the light field. The circularly polarized components of the dipole operator are denoted $\hat{d}_\pm(\boldsymbol{r})$, whereas $E_{\sigma^\pm}(\boldsymbol{r},t)$ are the correspondingly polarized components of the electric field. For simplicity, the laser pulses will be approximated by rectangular functions, so that the pulse area is given by $f_\pm\tau_p$, where τ_p is the pulse duration and $f_\pm$ is the effective amplitude of the $\sigma^\pm$ polarized part. For a light wavelength that is much larger than the length scale of localization (as in the experiment discussed here), the pulse area can also be written as $f_\pm\tau_p = \Theta_\pm \mathrm{e}^{\mathrm{i}\boldsymbol{k}\boldsymbol{r}}$, with $\boldsymbol{r}$ being the position of the localized electron [221].

With these assumptions, the action of the first pulse can be calculated. For the initial value of the density matrix, it is assumed that the trion recombination is short compared to the laser repetition time of 13.2 ns, so that before the arrival of the first pulse, only the ground state of the system is occupied. This means that only ρ_{11} and ρ_{22} are unequal to zero. The action of the first pulse with a pulse area of $|f_\pm\tau_p \ll 1|$, conforming with

experiment, results in the following density matrix elements:

$$\begin{aligned}
\rho_{11}(\tau_p) &= \rho_{11}^{(0)} + \frac{\mathrm{i}\tau_p}{2}\left(f_+\rho_{13}^{(0)} - f_+^*\rho_{31}^{(0)}\right) + \left(\rho_{33}^{(0)} - \rho_{11}^{(0)}\right)\frac{|f_+\tau_p|^2}{4} \\
\rho_{33}(\tau_p) &= \rho_{33}^{(0)} - \frac{\mathrm{i}\tau_p}{2}\left(f_+\rho_{13}^{(0)} - f_+^*\rho_{31}^{(0)}\right) - \left(\rho_{33}^{(0)} - \rho_{11}^{(0)}\right)\frac{|f_+\tau_p|^2}{4} \\
\rho_{22}(\tau_p) &= \rho_{22}^{(0)} + \frac{\mathrm{i}\tau_p}{2}\left(f_-\rho_{24}^{(0)} - f_-^*\rho_{42}^{(0)}\right) + \left(\rho_{44}^{(0)} - \rho_{22}^{(0)}\right)\frac{|f_-\tau_p|^2}{4} \\
\rho_{44}(\tau_p) &= \rho_{44}^{(0)} - \frac{\mathrm{i}\tau_p}{2}\left(f_-\rho_{24}^{(0)} - f_-^*\rho_{42}^{(0)}\right) - \left(\rho_{44}^{(0)} - \rho_{22}^{(0)}\right)\frac{|f_-\tau_p|^2}{4}
\end{aligned} \tag{A.3}$$

$$\begin{aligned}
\rho_{12}(\tau_p) &= \rho_{12}^{(0)} + \rho_{34}^{(0)}\frac{f_+^* f_-\tau_p^2}{4} + \rho_{14}^{(0)}\frac{\mathrm{i}f_-\tau_p}{2} - \rho_{32}^{(0)}\frac{\mathrm{i}f_+^*\tau_p}{2} \\
\rho_{34}(\tau_p) &= \rho_{34}^{(0)} + \rho_{12}^{(0)}\frac{f_+ f_-^*\tau_p^2}{4} + \rho_{32}^{(0)}\frac{\mathrm{i}f_-^*\tau_p}{2} - \rho_{14}^{(0)}\frac{\mathrm{i}f_+\tau_p}{2}
\end{aligned} \tag{A.4}$$

$$\begin{aligned}
\rho_{13}(\tau_p) &= \mathrm{e}^{\mathrm{i}\omega\tau_p}\left[\rho_{13}^{(0)} - \frac{\mathrm{i}f_+^*\tau_p}{2}(\rho_{33}^{(0)} - \rho_{11}^{(0)}) + \frac{f_+^*\tau_p^2}{4}(f_+\rho_{13}^{(0)} + f_+^*\rho_{31}^{(0)})\right] \\
\rho_{24}(\tau_p) &= \mathrm{e}^{\mathrm{i}\omega\tau_p}\left[\rho_{24}^{(0)} - \frac{\mathrm{i}f_-^*\tau_p}{2}(\rho_{44}^{(0)} - \rho_{22}^{(0)}) + \frac{f_-^*\tau_p^2}{4}(f_-\rho_{24}^{(0)} + f_-^*\rho_{42}^{(0)})\right] \\
\rho_{14}(\tau_p) &= \mathrm{e}^{\mathrm{i}\omega\tau_p}\left[\rho_{14}^{(0)} + \rho_{32}^{(0)}\frac{f_+^* f_-^*\tau_p^2}{4} + \rho_{12}^{(0)}\frac{\mathrm{i}f_-^*\tau_p}{2} - \rho_{34}^{(0)}\frac{\mathrm{i}f_+^*\tau_p}{2}\right] \\
\rho_{32}(\tau_p) &= \mathrm{e}^{-\mathrm{i}\omega\tau_p}\left[\rho_{32}^{(0)} + \rho_{14}^{(0)}\frac{f_+ f_-\tau_p^2}{4} + \rho_{34}^{(0)}\frac{\mathrm{i}f_-\tau_p}{2} - \rho_{12}^{(0)}\frac{\mathrm{i}f_+\tau_p}{2}\right]
\end{aligned} \tag{A.5}$$

The first group gives the diagonal elements of the density matrix and hence the occupations of the different states, the second group contains the spin coherence and the third group covers the coherent superpositions of ground and excited states. The superscript "(0)" signifies the matrix elements before pulse action. Due to the short pulse approximation, the magnetic field and the relaxation processes can be disregarded.

Between the first and second pulse (i.e. during τ_{12}), the system is subject to the action of the magnetic field. The corresponding Hamiltonian

$$\hat{H}_B = \begin{pmatrix} 0 & \hbar\Omega_\mathrm{L} & 0 & 0 \\ \hbar\Omega_\mathrm{L} & 0 & 0 & 0 \\ 0 & 0 & 2\hbar\omega_0 & \hbar\Omega_\mathrm{L}^H \\ 0 & 0 & \hbar\Omega_\mathrm{L}^H & 2\hbar\omega_0 \end{pmatrix} \tag{A.6}$$

contains the Larmor frequencies Ω_L and Ω_L^H of electron and hole (trion). Furthermore,

the relaxation Γ has to be taken into account by

$$\begin{pmatrix} -\frac{\rho_{11}-\rho_{22}}{2T_2^e} + \frac{\rho_{33}}{T_1} & \frac{T_1^eT_2^e}{2}\left[\frac{-\rho_{12}}{T_1^e+T_2^e} - \frac{\rho_{21}}{T_1^e-T_2^e}\right] & -\frac{\rho_{13}}{T_2} & -\frac{\rho_{14}}{T_2} \\ \frac{T_1^eT_2^e}{2}\left[\frac{-\rho_{21}}{T_1^e+T_2^e} - \frac{\rho_{12}}{T_1^e-T_2^e}\right] & -\frac{\rho_{22}-\rho_{11}}{2T_2^e} + \frac{\rho_{44}}{T_1} & -\frac{\rho_{23}}{T_2} & -\frac{\rho_{24}}{T_2} \\ -\frac{\rho_{31}}{T_2} & -\frac{\rho_{32}}{T_2} & \frac{\rho_{44}-\rho_{33}}{2T^h} - \frac{\rho_{33}}{T_1} & -\frac{\rho_{34}}{T^h} - \frac{\rho_{34}}{T_1} \\ -\frac{\rho_{41}}{T_2} & -\frac{\rho_{42}}{T_2} & -\frac{\rho_{43}}{T^h} - \frac{\rho_{43}}{T_1} & \frac{\rho_{33}-\rho_{44}}{2T^h} - \frac{\rho_{44}}{T_1} \end{pmatrix}. \quad \text{(A.7)}$$

Here T_2 is the optical coherence time, T_1 is the trion recombination time, T_1^e and T_2^e are the longitudinal and transverse electron spin relaxation times, respectively, and T^h is the hole spin relaxation time.[1]

Shortly before the arrival of the second pulse, the matrix elements that are relevant for the interaction with light read

$$\begin{aligned} \rho_{13}(\tau_{12}) &= \left[\rho_{13}(\tau_p)\cos\left(\Omega_\mathrm{L}\tau_{12}/2\right) - \mathrm{i}\rho_{23}(\tau_p)\sin\left(\Omega_\mathrm{L}\tau_{12}/2\right)\right]\mathrm{e}^{\tau_{12}(\mathrm{i}\omega_0 - 1/T_2)} \\ \rho_{23}(\tau_{12}) &= \left[\rho_{23}(\tau_p)\cos\left(\Omega_\mathrm{L}\tau_{12}/2\right) - \mathrm{i}\rho_{13}(\tau_p)\sin\left(\Omega_\mathrm{L}\tau_{12}/2\right)\right]\mathrm{e}^{\tau_{12}(\mathrm{i}\omega_0 - 1/T_2)} \\ \rho_{24}(\tau_{12}) &= \left[\rho_{24}(\tau_p)\cos\left(\Omega_\mathrm{L}\tau_{12}/2\right) - \mathrm{i}\rho_{14}(\tau_p)\sin\left(\Omega_\mathrm{L}\tau_{12}/2\right)\right]\mathrm{e}^{\tau_{12}(\mathrm{i}\omega_0 - 1/T_2)} \\ \rho_{14}(\tau_{12}) &= \left[\rho_{14}(\tau_p)\cos\left(\Omega_\mathrm{L}\tau_{12}/2\right) - \mathrm{i}\rho_{24}(\tau_p)\sin\left(\Omega_\mathrm{L}\tau_{12}/2\right)\right]\mathrm{e}^{\tau_{12}(\mathrm{i}\omega_0 - 1/T_2)}. \end{aligned} \quad \text{(A.8)}$$

Again, the short pulse approximation was used, so that $\tau_{12} - t_d \approx \tau_{12}$.

The action of the second pulse leads to

$$\begin{aligned} \rho_{11}(\tau_{12}+\tau_p) &\propto -f_{1+}f_{2+}\tau_p^2\mathrm{e}^{-\mathrm{i}(\omega\tau_p+\omega_0\tau_{12})}\cos\left(\frac{\Omega_\mathrm{L}\tau_{12}}{2}\right)\mathrm{e}^{-\tau_{12}/T_2} \\ \rho_{22}(\tau_{12}+\tau_p) &\propto -f_{1-}f_{2-}\tau_p^2\mathrm{e}^{-\mathrm{i}(\omega\tau_p+\omega_0\tau_{12})}\cos\left(\frac{\Omega_\mathrm{L}\tau_{12}}{2}\right)\mathrm{e}^{-\tau_{12}/T_2} \\ \rho_{33}(\tau_{12}+\tau_p) &\propto \quad f_{1+}f_{2+}\tau_p^2\mathrm{e}^{-\mathrm{i}(\omega\tau_p+\omega_0\tau_{12})}\cos\left(\frac{\Omega_\mathrm{L}\tau_{12}}{2}\right)\mathrm{e}^{-\tau_{12}/T_2} \\ \rho_{44}(\tau_{12}+\tau_p) &\propto \quad f_{1-}f_{2-}\tau_p^2\mathrm{e}^{-\mathrm{i}(\omega\tau_p+\omega_0\tau_{12})}\cos\left(\frac{\Omega_\mathrm{L}\tau_{12}}{2}\right)\mathrm{e}^{-\tau_{12}/T_2} \end{aligned} \quad \text{(A.9)}$$

for the diagonal elements and

$$\begin{aligned} \rho_{12}(\tau_{12}+\tau_p) &\propto -\mathrm{i}f_{1+}f_{2+}\tau_p^2\mathrm{e}^{-\mathrm{i}(\omega\tau_p+\omega_0\tau_{12})}\sin\left(\frac{\Omega_\mathrm{L}\tau_{12}}{2}\right)\mathrm{e}^{-\tau_{12}/T_2} \\ \rho_{34}(\tau_{12}+\tau_p) &\propto \quad \mathrm{i}f_{1+}f_{2-}\tau_p^2\mathrm{e}^{-\mathrm{i}(\omega\tau_p+\omega_0\tau_{12})}\sin\left(\frac{\Omega_\mathrm{L}\tau_{12}}{2}\right)\mathrm{e}^{-\tau_{12}/T_2} \end{aligned} \quad \text{(A.10)}$$

for the matrix elements describing spin coherence. The symbols $f_{n\pm}$ stand for the pulse amplitude of the $\sigma^\pm$-polarized component of the n-th pulse. The matrix elements for the

[1] For the hole spin relaxation, longitudinal and transverse direction are not discerned because no Larmor precession of the trion is observed $\Omega_\mathrm{L}^\mathrm{T} = 0$

optically active coherent superpositions of ground and excited state are

$$\begin{aligned}\rho_{13}(\tau_{12}+\tau_p) \propto & \mathrm{i}\tau_p^3 \mathrm{e}^{i\omega t}\mathrm{e}^{-t/T_2}\left[(f_{2+}^*)^2 f_{1+}\rho_{11}^{(0)}\cos(\Omega_\mathrm{L}\tau_{12}/2)\cos\left(\Omega_\mathrm{L}(t-\tau_{12})/2\right)\right. \\ & \left. + f_{2+}^* f_{2-}^* f_{1-}\rho_{22}^{(0)}\sin(\Omega_\mathrm{L}\tau_{12}/2)\sin\left(\Omega_\mathrm{L}(t-\tau_{12})/2\right)\right] + c.c. \\ \rho_{24}(\tau_{12}+\tau_p) \propto & \mathrm{i}\tau_p^3 \mathrm{e}^{i\omega t}\mathrm{e}^{-t/T_2}\left[(f_{2-}^*)^2 f_{1-}\rho_{22}^{(0)}\cos(\Omega_\mathrm{L}\tau_{12}/2)\cos\left(\Omega_\mathrm{L}(t-\tau_{12})/2\right)\right. \\ & \left. + f_{2+}^* f_{2-}^* f_{1+}\rho_{11}^{(0)}\sin(\Omega_\mathrm{L}\tau_{12}/2)\sin\left(\Omega_\mathrm{L}(t-\tau_{12})/2\right)\right] + c.c.\end{aligned} \tag{A.11}$$

In order to calculate the four wave mixing signal, the Eqs. (A.11) for individual oscillators must be summed over all electron-trion-complexes. The polarization at the time $t = 2\tau_{12}$ of echo emission amounts to

$$\begin{aligned}P_\mathrm{PE}^+ &\propto \mathrm{e}^{-2\tau_{12}/T_2}\left[(f_{2+}^*)^2 f_{1+}\rho_{11}^{(0)}\cos^2(\Omega_\mathrm{L}\tau_{12}/2) + f_{2+}^* f_{2-}^* f_{1-}\rho_{22}^{(0)}\sin^2(\Omega_\mathrm{L}\tau_{12}/2)\right] + c.c. \\ P_\mathrm{PE}^- &\propto \mathrm{e}^{-2\tau_{12}/T_2}\left[(f_{2-}^*)^2 f_{1-}\rho_{11}^{(0)}\cos^2(\Omega_\mathrm{L}\tau_{12}/2) + f_{2+}^* f_{2-}^* f_{1+}\rho_{22}^{(0)}\sin^2(\Omega_\mathrm{L}\tau_{12}/2)\right] + c.c.\end{aligned} \tag{A.12}$$

From these equations, all polarization configurations can be calculated by inserting the respective $f_{n\pm}$ for the pulse sequence.

For σ^+ polarized excitation, $f_{1-} = f_{2-} = 0$, so that $P_\mathrm{PE}^- = 0$ and

$$P_\mathrm{PE}^+ \propto (f_{2+})^2 (f_{1+})^* \mathrm{e}^{-2\tau_{12}/T_2}\left[\rho_{11}^{(0)}\frac{1+\cos(\Omega_\mathrm{L}\tau_{12})}{2}\right] + c.c. \tag{A.13}$$

For collinear polarized excitation, $f_{1+} = f_{1-} = f_1$ and $f_{2+}^* = f_{2-}^* = F_2^*$, so that

$$P_\mathrm{PE}^{lin,co} \propto \frac{1}{2}(f_2^*)^2 f_1 \mathrm{e}^{-2\tau_{12}/T_2} + c.c. \tag{A.14}$$

For crossed-linear polarized excitation, again $f_{1+} = f_{1-} = f_1$ but $f_{2+}^* = -f_{2-}^*$, so that

$$P_\mathrm{PE}^{lin,cr} \propto \frac{1}{2}(f_2^*)^2 f_1 \mathrm{e}^{-2\tau_{12}/T_2}\cos(\Omega_\mathrm{L}\tau_{12}) + c.c. \tag{A.15}$$

An additional analysis of the Larmor precession of the hole spin reveals that for P_PE^+ and $P_\mathrm{PE}^\mathrm{lin,co}$ only a slowly-varying envelop function has to be multiplied to Eq. (A.13) and Eq. (A.14), which for the relatively short decay times observed in the experiment are of no consequence.

An analysis of the Larmor precession of the hole spin reveals that for P_PE^+ an additional slowly-varying envelop function has to be multiplied to Eq. (A.13). The additional contribution of the hole spin precession that is added in

$$P_\mathrm{PE}^+ \propto (f_{2+})^2 (f_{1+})^* \mathrm{e}^{-2\tau_{12}/T_2}\left[\rho_{11}^{(0)}\frac{1+\cos(\Omega_\mathrm{L}\tau_{12})}{2}\frac{1+\cos(\Omega_\mathrm{L}^H\tau_{12})}{2}\right] + c.c. \tag{A.16}$$

has hardly any consequence due to the relatively short decay time observed in experiment. For collinearly polarized excitation, the oscillation due to the hole spin precession cancel

in the same way as the contribution of the electron spin precession.
In contrast to that, for crossed linear polarization, the precession frequency of the signal is altered so that it follows

$$P_{\mathrm{PE}}^{lin,cr} \propto \frac{1}{2}(f_2^*)^2 f_1 \mathrm{e}^{-2\tau_{12}/T_2} \cos\Big((\Omega_{\mathrm{L}} - \omega_L^H)\tau_{12}\Big) + c.c. \tag{A.17}$$

The Larmor precession frequency is determined by the Landé factors of electron and hole via $\Omega_{\mathrm{L}} - \Omega_{\mathrm{L}}^H = |g_e - g_{h,\perp}|\mu_B B$.

B Calculation of the stimulated photon echo amplitude

For the calculation of the stimulated photon echo amplitude, the density matrix approach already used for the calculation of the spontaneous echo in Appendix A is followed. Due to the considerably longer times ($\tau_{23} \ll T_2$) it is convenient to describe the evolution through the electron and trion spin polarizations as well as the occupation of electron and trion levels instead of all individual density matrix elements. The following relations hold:

$$\begin{aligned}
&S_z = (\rho_{11} - \rho_{22})/2, \quad && S_y = \mathrm{i}\,(\rho_{12} - \rho_{21})/2, \quad && S_x = (\rho_{12} + \rho_{21})/2, \\
&J_z = (\rho_{33} - \rho_{44})/2, && J_y = \mathrm{i}\,(\rho_{34} - \rho_{43})/2, && J_x = (\rho_{34} + \rho_{43})/2, \\
&n_e = (\rho_{11} + \rho_{22})/2, && n_T = \ (\rho_{33} + \rho_{44})/2 && .
\end{aligned} \tag{B.1}$$

The populations of electrons and trions are denoted n_e and n_T, respectively, and $S_{x,y,z}$ and $J_{x,y,z}$ are the components of the electron and trion spin polarizations.

The situation up to the action of the second laser pulse was already discussed in Appendix A, so that Eqs. (A.9) and (A.10) only need to be inserted in Eqs. (B.1) to obtain the spin polarizations and occupations after the action of the second pulse. The results are

$$S_z(\tau_{12} + 2\tau_p) \propto -K\Delta \cos(\Omega_{\mathrm{L}}\tau_{12}/2), \tag{B.2}$$
$$S_y(\tau_{12} + 2\tau_p) \propto \ \ K\Delta \sin(\Omega_{\mathrm{L}}\tau_{12}/2), \tag{B.3}$$
$$S_x(\tau_{12} + 2\tau_p) \propto -\mathrm{i}K\Delta\Sigma \cos(\Omega_{\mathrm{L}}\tau_{12}/2), \tag{B.4}$$

for the electron spin polarizations,

$$J_z(\tau_{12} + 2\tau_p) \propto \ \ K\Delta \ \ \cos(\Omega_{\mathrm{L}}\tau_{12}/2), \tag{B.5}$$
$$J_y(\tau_{12} + 2\tau_p) \propto -K\Delta_T \sin(\Omega_{\mathrm{L}}\tau_{12}/2), \tag{B.6}$$
$$J_x(\tau_{12} + 2\tau_p) \propto \ \mathrm{i}\,K\Sigma_T \sin(\Omega_{\mathrm{L}}\tau_{12}/2), \tag{B.7}$$

for the trion spin polarizations and

$$n_e(\tau_{12}+2\tau_p) \propto -2K\Sigma\cos\left(\Omega_{\mathrm{L}}\tau_{12}/2\right), \tag{B.8}$$
$$n_T(\tau_{12}+2\tau_p) \propto \quad 2K\Sigma\cos\left(\Omega_{\mathrm{L}}\tau_{12}/2\right) \tag{B.9}$$

for the occupations. The parameters

$$\Delta \;= \tau_p\left(f_{1+}f_{2+}-f_{1-}f_{2-}\right), \qquad \Sigma \;= \tau_p\left(f_{1+}f_{2+}+f_{1-}f_{2-}\right), \tag{B.10}$$
$$\Delta_T = \tau_p\left(f_{1+}f_{2-}-f_{1-}f_{2+}\right), \qquad \Sigma_T = \tau_p\left(f_{1+}f_{2-}+f_{1-}f_{2+}\right) \tag{B.11}$$

reflect different polarization configurations and

$$K = \frac{1}{16}\mathrm{e}^{-\left(\omega\tau_p+\omega_0\tau_{12}\right)}\mathrm{e}^{-\tau_{12}/T_2} \tag{B.12}$$

abbreviates a factor that all parameters share.

After the action of the second pulse, the dynamics of the electron spin components are mainly characterized by the Larmor precession about the x-axis:

$$S_x(t) = S_{x,0}\mathrm{e}^{-(t-\tau_{12})/T_1^e} \tag{B.13}$$
$$S_y(t) = \mathrm{e}^{-(t-\tau_{12})/T_2^e}\left(S_{y,0}+\xi_2 J_{z,0}\right)\cos\left(\Omega_{\mathrm{L}}(t-\tau_{12})\right) \tag{B.14}$$
$$+\,\mathrm{e}^{-(t-\tau_{12})/T_2^e}\left(S_{z,0}+\xi_1 J_{z,0}\right)\sin\left(\Omega_{\mathrm{L}}(t-\tau_{12})\right) \tag{B.15}$$
$$-\,\mathrm{e}^{-(t-\tau_{12})/\tau_T}\xi_2 J_{z,0} \tag{B.16}$$
$$S_z(t) = \mathrm{e}^{-(t-\tau_{12})/T_2^e}\left(S_{z,0}+\xi_1 J_{z,0}\right)\cos\left(\Omega_{\mathrm{L}}(t-\tau_{12})\right) \tag{B.17}$$
$$+\,\mathrm{e}^{-(t-\tau_{12})/T_2^e}\left(S_{y,0}+\xi_2 J_{z,0}\right)\sin\left(\Omega_{\mathrm{L}}(t-\tau_{12})\right) \tag{B.18}$$
$$-\,\mathrm{e}^{-(t-\tau_{12})/\tau_T}\xi_1 J_{z,0} \tag{B.19}$$

For compactness $\xi_1+\mathrm{i}\xi_2 = \frac{1}{T_1(\gamma-\mathrm{i}\omega)}$ was defined with $\gamma = 1/\tau_T - 1/T_2^e$.
In contrast to the electron, the Landé factor of the hole is close to zero, which allows the description of the spin dynamics solely with an exponential decay:

$$J_z(t) = J_{z,0}\mathrm{e}^{-(t-\tau_{12})/\tau_T}, \qquad J_y(t) = J_{y,0}\mathrm{e}^{-(t-\tau_{12})/\tau_T}, \qquad J_x(t) = J_{x,0}\mathrm{e}^{-(t-\tau_{12})/\tau_T}, \tag{B.20}$$

where τ_T is the trion spin lifetime with $1/\tau_T = 1/T^h + 1/T_1$.
Also the dynamics of the occupations are defined by an exponential decay. The recombination of the trion with characteristic time T_1 is the reason for the increase of the electron population an a decrease of the hole population with

$$n_T(t) = n_{T,0}\mathrm{e}^{-(t-\tau_{12})/T_1} \tag{B.21}$$
$$n_e(t) = n_{e,0}+n_{T,0}-n_T(t). \tag{B.22}$$

These dependencies hold until the arrival of the third laser pulse. In order to calculate the effect of the third beam, the situation before its arrival has to be defined. The spin

polarization components and occupations of electrons and holes are given by

$$
\begin{aligned}
S_z \propto & K\Delta \Big[-\mathrm{e}^{-\tau_{23}/\tau_T} \xi_1 \cos(\Omega_\mathrm{L}\tau_{12}/2) + && \text{(B.23)}\\
& \mathrm{e}^{-\tau_{23}/T_2^e} \left((\xi_1 - 1)\cos(\Omega_\mathrm{L}\tau_{12}/2)\cos(\Omega_\mathrm{L}\tau_{23}) + \sin(\Omega_\mathrm{L}\tau_{12}/2) + \right. && \text{(B.24)}\\
& \left. \xi_2 \cos(\Omega_\mathrm{L}\tau_{12}/2)\sin(\Omega_\mathrm{L}\tau_{12}/2) \right) \Big], && \text{(B.25)}\\
S_y \propto & K\Delta \Big[-\mathrm{e}^{-\tau_{23}/\tau_T} \xi_2 \cos(\Omega_\mathrm{L}\tau_{12}/2) + && \text{(B.26)}\\
& \mathrm{e}^{-\tau_{23}/T_2^e} \left((1 - \xi_1)\cos(\Omega_\mathrm{L}\tau_{12}/2)\sin(\Omega_\mathrm{L}\tau_{23}) + \sin(\Omega_\mathrm{L}\tau_{12}/2) + \right. && \text{(B.27)}\\
& \left. \xi_2 \cos(\Omega_\mathrm{L}\tau_{12}/2)\cos(\Omega_\mathrm{L}\tau_{12}/2) \right) \Big], && \text{(B.28)}\\
S_x \propto & -\mathrm{i}K\Sigma \mathrm{e}^{-\tau_{23}/T_1^e} \sin\left(\Omega_\mathrm{L}\tau_{12}/2\right), && \text{(B.29)}
\end{aligned}
$$

$$
\begin{aligned}
J_z &\propto K\Delta \mathrm{e}^{-\tau_{23}/\tau_T} \cos(\Omega_\mathrm{L}\tau_{12}/2), && \text{(B.30)}\\
J_y &\propto -K\Delta_T \mathrm{e}^{-\tau_{23}/\tau_T} \sin(\Omega_\mathrm{L}\tau_{12}/2), && \text{(B.31)}\\
J_x &\propto \mathrm{i}K\Sigma_T \mathrm{e}^{-\tau_{23}/\tau_T} \sin(\Omega_\mathrm{L}\tau_{12}/2), && \text{(B.32)}
\end{aligned}
$$

and

$$
\begin{aligned}
n_e &\propto -2K\Sigma \mathrm{e}^{-\tau_{23}/T_1} \cos(\Omega_\mathrm{L}\tau_{12}/2), && \text{(B.33)}\\
n_T &\propto 2K\Sigma \mathrm{e}^{-\tau_{23}/T_1} \cos(\Omega_\mathrm{L}\tau_{12}/2). && \text{(B.34)}
\end{aligned}
$$

With these, the action of the third laser pulse can be calculated. For the emission of the photon echo signal, the density matrix elements ρ_{13} and ρ_{24} are crucial. At the time of the stimulated photon echo occurrence, $t = \tau_{23} + 2\tau_{12} + 3\tau_p$, they read

$$
\begin{aligned}
\rho_{13} = & -\frac{\mathrm{i}}{2} \mathrm{e}^{\mathrm{i}(\omega\tau_p + \omega_0\tau 12)} \mathrm{e}^{-\tau_{12}/T_2} \times \\
& \Big[f_{3+}\tau_p \left(\frac{n_T - n_e}{2} + J_z - S_z \right) \cos(\Omega_\mathrm{L}\tau_{12}/2) \\
& + \left(f_{3-}\tau_p \left(J_y - \mathrm{i}J_x \right) - f_{3+}\tau_p \left(S_y - \mathrm{i}S_x \right) \right) \sin(\Omega_\mathrm{L}\tau_{12}/2) \Big] \\
\rho_{24} = & -\frac{\mathrm{i}}{2} \mathrm{e}^{\mathrm{i}(\omega\tau_p + \omega_0\tau 12)} \mathrm{e}^{-\tau_{12}/T_2} \times \\
& \Big[f_{3-}\tau_p \left(\frac{n_T - n_e}{2} - J_z + S_z \right) \cos(\Omega_\mathrm{L}\tau_{12}/2) \\
& - \left(f_{3+}\tau_p \left(J_y - \mathrm{i}J_x \right) - f_{3+}\tau_p \left(S_y - \mathrm{i}S_x \right) \right) \sin(\Omega_\mathrm{L}\tau_{12}/2) \Big].
\end{aligned}
\qquad \text{(B.35)}
$$

For the calculation of the stimulated photon echo signals for different excitation polarizations, the pulse intensity parameters $f_{n\pm}$ have to be matched to the experimental conditions.

Configuration HHH

For the excitation with collinear polarization, this means $f_{1+} = f_{1-} \equiv f_1$, $f_{2+} = f_{2-} \equiv f_2$, and $f_{3+} = f_{3-} \equiv f_3$. This means $\Delta = \Delta_T = 0$, $\Sigma = \Sigma_T = 2f_1 f_2$ and consequently $S_z = S_y = J_z = J_y = 0$. The photon echo is given by

$$\begin{aligned} P_{HHH} \propto & -\mathrm{i}\mathrm{e}^{\mathrm{i}\left(\omega\tau_p+\omega_0\tau_{12}\right)}\mathrm{e}^{-\tau_{12}/T_2} f_3 \times \\ & \left[\frac{n_T - n_e}{2}\cos(\Omega_\mathrm{L}\tau_{12}/2) - \mathrm{i}\,(J_x - S_x)\sin(\Omega_\mathrm{L}\tau_{12}/2)\right] + c.c. \end{aligned} \tag{B.36}$$

and polarized in the same way. Two important features have to be noted here: 1) The only factor that decays with the long relaxation time of the electron spin is the term $\propto S_x$. All the other factors decay on shorter time scales of T_1 or τ_T. 2) Due to the factor $\propto \sin(\Omega_\mathrm{L}\tau_{12}/2)$, this long-living contribution is only present in a magnetic field.

With all the substitutions reversed, the stimulated photon echo amplitude reads

$$\begin{aligned} P_{HHH} \propto & -\mathrm{i}\mathrm{e}^{-2\tau_{12}/T_2} f_1 f_2 f_3 \tau_p^3 \left[\mathrm{e}^{-\tau_{23}/T_1^e}\sin^2(\Omega_\mathrm{L}\tau_{12}/2)\right. \\ & \left. + \mathrm{e}^{-\tau_{23}/T_1}\left(2\cos^2(\Omega_\mathrm{L}\tau_{12}/2) + \mathrm{e}^{-\tau_{23}/T_h}\sin^2(\Omega_\mathrm{L}\tau_{12}/2)\right)\right] + c.c. \end{aligned} \tag{B.37}$$

Configuration HVV

Likewise, for crossed-linear polarization the pulse intensity parameters $f_{1+} = f_{1-} \equiv f_1$, $f_{2+} = -f_{2-} \equiv f_2$, and $f_{3+} = -f_{3-} \equiv f_3$ lead to $\Delta = -\Delta_T = 2f_1 f_2$ and $\Sigma = \Sigma_T = 0$.

The polarization of the photon echo is parallel to the polarization of the first pulse and the amplitude is given by

$$\begin{aligned} P_{HVV} \propto & -\mathrm{i}\mathrm{e}^{\mathrm{i}(\omega\tau_p+\omega_0\tau_{12})}\mathrm{e}^{-\tau_{12}/T_2} f_3 \tau_p \times \\ & \left[(J_z - S_z)\cos(\Omega_\mathrm{L}\tau_{12}/2) - (J_y + S_y)\sin(\Omega_\mathrm{L}\tau_{12}/2)\right] + c.c. \end{aligned} \tag{B.38}$$

The substitution of the parameters defined in Eq. (B.1) results in a lengthy term reading

$$\begin{aligned} P_{HVV} \propto & -\mathrm{i}\mathrm{e}^{-2\tau_{12}/T_2} f_1 f_2 f_3 \tau_p^3 \times \\ & \Big[\mathrm{e}^{-\tau_{23}/\tau_T}\cos(\Omega_\mathrm{L}\tau_{12}) \\ & + \mathrm{e}^{-\tau_{23}/\tau_T}\cos(\Omega_\mathrm{L}\tau_{12}/2)\left[\xi_1\cos(\Omega_\mathrm{L}\tau_{12}/2) + \xi_2\sin(\Omega_\mathrm{L}\tau_{12}/2)\right] \\ & + \mathrm{e}^{-\tau_{23}/T_2^e}\cos\left(\Omega_\mathrm{L}(\tau_{12}+\tau_{23})\right) \\ & - \mathrm{e}^{-\tau_{23}/T_2^e}\left[\xi_1\cos(\Omega_\mathrm{L}(\tau_{12}/2+\tau_{23})) + \xi_2\sin(\Omega_\mathrm{L}(\tau_{12}/2+\tau_{23}))\right]\Big] \\ & + c.c. \end{aligned} \tag{B.39}$$

This can be simplified by the assumption that the hole spin relaxation is faster than the radiative recombination, $T_h \ll T_1$. In that case, $\xi_1 = \xi_2 = 0$ and the stimulated photon echo amplitude is

$$\begin{aligned} P_{HVV} \propto & -\mathrm{i}\mathrm{e}^{-2\tau_{12}/T_2} f_1 f_2 f_3 \tau_p^3 \times \\ & \left[\mathrm{e}^{-\tau_{23}/\tau_T}\cos(\Omega_\mathrm{L}\tau_{12}) + \mathrm{e}^{-\tau_{23}/T_2^e}\cos\left(\Omega_\mathrm{L}(\tau_{12}+\tau_{23})\right)\right] + c.c. \end{aligned} \tag{B.40}$$

Bibliography

[1] M. Hilbert and P. Lopez, *The World's Technological Capacity to Store, Communicate, and Compute Information*, Science, **332**(6025), 60 (2011)

[2] Apple Inc., *Apple Reinvents the Phone with iPhone* (2007), URL `http://www.apple.com/pr/library/2007/01/09Apple-Reinvents-the-Phone-with-iPhone.html`

[3] G. E. Moore, *Cramming more components onto integrated circuits*, Electronics, **38**(8), 114 (1965)

[4] G. E. Moore, *Afternoon Session*, in *Intel Developers's Forum*, Intel Corporation, San Francisco (2007)

[5] M. Fuechsle, J. A. Miwa, S. Mahapatra, H. Ryu, S. Lee, O. Warschkow, L. C. L. Hollenberg, G. Klimeck, and M. Y. Simmons, *A single-atom transistor*, Nature Nanotechnology, **7**(4), 242 (2012)

[6] I. L. Markov, *Limits on fundamental limits to computation*, Nature, **512**(7513), 147 (2014)

[7] Y. I. Manin, *Vychislimoe i nevychislimoe [Computable and Uncomputable]*, Sovetskoye radio, Moscow (1980)

[8] P. Benioff, *Quantum mechanical hamiltonian models of turing machines*, Journal of Statistical Physics, **29**(3), 515 (1982)

[9] R. P. Feynman, *Simulating physics with computers*, International Journal of Theoretical Physics, **22**(6/7), 467 (1982)

[10] D. Deutsch, *Quantum Theory, the Church-Turing Principle and the Universal Quantum Computer*, Proceedings of the Royal Society A: Mathematical, Physical and Engineering Sciences, **400**(1818), 97 (1985)

[11] L. K. Grover, *A fast quantum mechanical algorithm for database search*, in *Proceedings of the 28th annual ACM symposium on Theory of computing - STOC '96*, ACM Press (1996)

[12] P. W. Shor, *Polynomial-Time Algorithms for Prime Factorization and Discrete Logarithms on a Quantum Computer*, SIAM Journal on Computing, **26**(5), 1484 (1997)

[13] F. Henneberger and O. Benson (editors), *Semiconductor quantum bits*, Pan Stanford, Singapore (2009)

[14] O. Gywat, H. J. Krenner, and J. Berezovsky, *Spins in optically active quantum dots: Concepts and methods*, Wiley-VCH, Weinheim (2010)

[15] N. C. Jones, R. V. Meter, A. G. Fowler, P. L. McMahon, J. Kim, T. D. Ladd, and Y. Yamamoto, *Layered Architecture for Quantum Computing*, Physical Review X, **2**(3) (2012)

[16] M. N. Baibich, J. M. Broto, A. Fert, F. N. V. Dau, F. Petroff, P. Etienne, G. Creuzet, A. Friederich, and J. Chazelas, *Giant Magnetoresistance of (001)Fe/(001)Cr Magnetic Superlattices*, Physical Review Letters, **61**(21), 2472 (1988)

[17] G. Binasch, P. Grünberg, F. Saurenbach, and W. Zinn, *Enhanced magnetoresistance in layered magnetic structures with antiferromagnetic interlayer exchange*, Physical Review B, **39**(7), 4828 (1989)

[18] A. Fert, *Nobel Lecture: Origin, development, and future of spintronics*, Reviews of Modern Physics, **80**(4), 1517 (2008)

[19] S. Bader and S. Parkin, *Spintronics*, Annual Review of Condensed Matter Physics, **1**(1), 71 (2010)

[20] G. A. Prinz, *Magnetoelectronics*, Science, **282**(5394), 1660 (1998)

[21] S. A. Wolf, D. D. Awschalom, R. A. Buhrman, J. M. Daughton, S. von Molnár, M. L. Roukes, A. Y. Chtchelkanova, and D. M. Treger, *Spintronics: A Spin-Based Electronics Vision for the Future*, Science, **294**(5546), 1488 (2001)

[22] I. Žutić, J. Fabian, and S. Das Sarma, *Spintronics: Fundamentals and applications*, Reviews of Modern Physics, **76**, 323 (2004)

[23] D. D. Awschalom, R. A. Buhrmann, J. M. Daughton, S. von Molnár, and M. L. Roukes (editors), *Spin electronics*, Kluwer Academic Publishers, Dordrecht, Boston (2004)

[24] T. Dietl, D. D. Awschalom, M. Kaminska, and H. Ohno (editors), *Spintronics*, Elsevier, Oxford (2008)

[25] W. Shockley, J. Bardeen, and W. H. Brattain, *Physics 1956*, in *Physics 1942–1962*, 313–386, Elsevier BV (2013)

[26] S. Datta and B. Das, *Electronic analog of the electro-optic modulator*, Applied Physics Letters, **56**(7), 665 (1990)

[27] F. Capasso, *Band-Gap Engineering: From Physics and Materials to New Semiconductor Devices*, Science, **235**(4785), 172 (1987)

[28] J. A. Gaj and J. Kossut (editors), *Introduction to the Physics of Diluted Magnetic Semiconductors*, Springer Berlin Heidelberg (2010)

[29] J. K. Furdyna and J. Kossut, *Semiconductors and Semimetals. Volume 25: Diluted Magnetic Semiconductors (Semiconductors and Semimetals)*, Academic Press, Boston (1988)

[30] W. M. Chen and I. A. Buyanova, *Handbook of Spintronic Semiconductors*, Pan Stanford, Singapore (2010)

[31] H. Ohno, A. Shen, F. Matsukura, A. Oiwa, A. Endo, S. Katsumoto, and Y. Iye, *(Ga,Mn)As: A new diluted magnetic semiconductor based on GaAs*, Applied Physics Letters, **69**(3), 363 (1996)

[32] A. H. MacDonald, P. Schiffer, and N. Samarth, *Ferromagnetic semiconductors: moving beyond (Ga,Mn)As*, Nature Materials, **4**(3), 195 (2005)

[33] T. Dietl and H. Ohno, *Dilute ferromagnetic semiconductors: Physics and spintronic structures*, Reviews of Modern Physics, **86**, 187 (2014)

[34] T. Jungwirth, J. Wunderlich, V. Novák, K. Olejník, B. L. Gallagher, R. P. Campion, K. W. Edmonds, A. W. Rushforth, A. J. Ferguson, and P. Němec, *Spin-dependent phenomena and device concepts explored in (Ga,Mn)As*, Reviews of Modern Physics, **86**, 855 (2014)

[35] Nature Materials, *Spintronics*, volume 11 (5), Nature Publishing Group (2004)

[36] D. D. Awschalom and M. E. Flatté, *Challenges for semiconductor spintronics*, Nature Physics, **3**(3), 153 (2007)

[37] J. König and M. Oestreich (editors), *Special Issue: Semiconductor Spintronics*, *physica status solidi (b)*, volume 251, (9) (2014)

[38] G. A. Prinz, *Spin-Polarized Transport*, Physics Today, **48**(4), 58 (1995)

[39] L. W. Molenkamp, R. Fiederling, M. Keim, G. Reuscher, W. Ossau, G. Schmidt, and A. Waag, *Injection and detection of a spin-polarized current in a light-emitting diode*, Nature, **402**(6763), 787 (1999)

[40] G. Schmidt and L. W. Molenkamp, *Spin injection into semiconductors, physics and experiments*, Semiconductor Science and Technology, **17**(4), 310 (2002)

[41] M. Dyakonov and V. Perel, *Current-induced spin orientation of electrons in semiconductors*, Physics Letters A, **35**(6), 459 (1971)

[42] Y. K. Kato, R. C. Myers, A. C. Gossard, and D. D. Awschalom, *Observation of the Spin Hall Effect in Semiconductors*, Science, **306**(5703), 1910 (2004)

[43] J. Wunderlich, B. Kaestner, J. Sinova, and T. Jungwirth, *Experimental Observation of the Spin-Hall Effect in a Two-Dimensional Spin-Orbit Coupled Semiconductor System*, Physical Review Letters, **94**, 047204 (2005)

[44] W. Döring, *Über die Temperaturabhängigkeit des Elastizitätsmoduls ferromagnetischer Substanzen*, Annalen der Physik, **424**(5), 465 (1938)

[45] D. V. Baxter, D. Ruzmetov, J. Scherschligt, Y. Sasaki, X. Liu, J. K. Furdyna, and C. H. Mielke, *Anisotropic magnetoresistance in* $Ga_{1-x}Mn_xAs$, Physical Review B, **65**, 212407 (2002)

[46] A. G. Petukhov, A. N. Chantis, and D. O. Demchenko, *Resonant Enhancement of Tunneling Magnetoresistance in Double-Barrier Magnetic Heterostructures*, Physical Review Letters, **89**, 107205 (2002)

[47] A. Slobodskyy, C. Gould, T. Slobodskyy, C. R. Becker, G. Schmidt, and L. W. Molenkamp, *Voltage-Controlled Spin Selection in a Magnetic Resonant Tunneling Diode*, Physical Review Letters, **90**, 246601 (2003)

[48] J. Slonczewski, *Current-driven excitation of magnetic multilayers*, Journal of Magnetism and Magnetic Materials, **159**(1-2), L1 (1996)

[49] M. Yamanouchi, D. Chiba, F. Matsukura, and H. Ohno, *Current-induced domain-wall switching in a ferromagnetic semiconductor structure*, Nature, **428**(6982), 539 (2004)

[50] D. Ralph and M. Stiles, *Spin transfer torques*, Journal of Magnetism and Magnetic Materials, **320**(7), 1190 (2008)

[51] A. Chernyshov, M. Overby, X. Liu, J. K. Furdyna, Y. Lyanda-Geller, and L. P. Rokhinson, *Evidence for reversible control of magnetization in a ferromagnetic material by means of spin–orbit magnetic field*, Nature Physics, **5**(9), 656 (2009)

[52] N. Locatelli, V. Cros, and J. Grollier, *Spin-torque building blocks*, Nature Materials, **13**(1), 11 (2013)

[53] M. Faraday, *Nov. 12, 1839 - June 26, 1847*, in T. Martin (editor), *Faraday's diary*, volume 4, 7504–7718, George Bell and Sons, Ltd, London (1933)

[54] J. Kerr, *XLIII. On rotation of the plane of polarization by reflection from the pole of a magnet*, Philosophical Magazine Series 5, **3**(19), 321 (1877)

[55] F. Meier and B. Zakharchenya (editors), *Optical Orientation*, North-Holland, Amsterdam (1984)

[56] Y. Kato, R. C. Myers, A. C. Gossard, and D. D. Awschalom, *Coherent spin manipulation without magnetic fields in strained semiconductors*, Nature, **427**(6969), 50 (2004)

[57] G. Slavcheva and O. Hess, *All-optical coherent control of spin dynamics in semiconductor quantum dots*, Optical and Quantum Electronics, **38**(12-14), 973 (2007)

[58] R. Hanson and D. D. Awschalom, *Coherent manipulation of single spins in semiconductors*, Nature, **453**(7198), 1043 (2008)

[59] H. Kosaka, T. Inagaki, Y. Rikitake, H. Imamura, Y. Mitsumori, and K. Edamatsu, *Spin state tomography of optically injected electrons in a semiconductor*, Nature, **457**(7230), 702 (2009)

[60] S. Varwig, *Optical electron spin tomography and hole spin coherence studies in (In,Ga)As/GaAs quantum dots*, Dissertation, Technische Universität Dortmund (2014)

[61] P. Y. Yu and M. Cardona, *Fundamentals of semiconductors*, Springer, Berlin, 4th edition (2010)

[62] C. F. Klingshirn, *Semiconductor Optics*, Springer, Berlin, 4th edition (2012)

[63] L. Allen and J. H. Eberly, *Optical resonance and two-level atoms*, John Wiley & Sons, New York (1975)

[64] V. Korenev, *Electric Control of Magnetic Moment in a Ferromagnet/Semiconductor Hybrid System*, JETP Letters, **78**(9), 564 (2003)

[65] R. C. Myers, A. C. Gossard, and D. D. Awschalom, *Tunable spin polarization in III-V quantum wells with a ferromagnetic barrier*, Physical Review B, **69**, 161305 (2004)

[66] S. V. Zaitsev, M. V. Dorokhin, A. S. Brichkin, O. V. Vikhrova, Y. A. Danilov, B. N. Zvonkov, and V. D. Kulakovskii, *Ferromagnetic effect of a Mn delta layer in the GaAs barrier on the spin polarization of carriers in an InGaAs/GaAs quantum well*, JETP Letters, **90**(10), 658 (2010)

[67] A. I. Lvovsky, B. C. Sanders, and W. Tittel, *Optical quantum memory*, Nature Photonics, **3**(12), 706 (2009)

[68] K. Hammerer, A. S. Sørensen, and E. S. Polzik, *Quantum interface between light and atomic ensembles*, Reviews of Modern Physics, **82**, 1041 (2010)

[69] N. A. Kurnit, I. D. Abella, and S. R. Hartmann, *Observation of a photon echo*, Physical Review Letters, **13**(19), 567 (1964)

[70] C. Kittel, *Einführung in die Festkörperphysik*, Oldenbourg, München, 14th edition (2006)

[71] F. Schwabl, *Quantenmechanik*, Springer, Berlin, 6th edition (2002)

[72] W. Nolting, *Grundkurs Theoretische Physik 5/2*, Springer, Berlin, Heidelberg, 8th edition (2015)

[73] S. Gasiorowicz, *Quantum Physics*, Wiley, 3rd edition (2003)

[74] D. J. Griffiths, *Quantenmechanik*, Pearson Studium, München (2012)

[75] R. Winkler, *Spin–Orbit Coupling Effects in Two-Dimensional Electron and Hole Systems*, Springer, Berlin (2003)

[76] M. Grundmann, *The Physics of Semiconductors*, Springer, Berlin, Heidelberg, 2nd edition (2010)

[77] M. I. Dyakonov, *Basics of semiconductors and spin physics*, in *Spin physics in semiconductors* [78], chapter 1, 1–28

[78] M. I. Dyakonov (editor), *Spin physics in semiconductors*, Springer Series in solid-state sciences 157, Springer, Berlin (2008)

[79] E. L. Ivchenko, *Optical spectroscopy of semiconductor nanostructures*, Springer, Berlin (2004)

[80] J. Frenkel, *On the Transformation of light into Heat in Solids. I*, Physical Review, **37**, 17 (1931)

[81] M. Hayashi and K. Katsuki, *Absorption spectrum of cuprous oxide*, Journal of the Physical Society of Japan, **5**(5), 380 (1950)

[82] E. F. Gross and N. A. Karryjew, *The optical spectrum of the exciton*, Doklady Akademii Nauk SSSR, **84**, 471 (1952)

[83] M. Bayer, G. Ortner, O. Stern, A. Kuther, A. A. Gorbunov, A. Forchel, P. Hawrylak, S. Fafard, K. Hinzer, T. L. Reinecke, S. N. Walck, J. P. Reithmaier, F. Klopf, and F. Schäfer, *Fine structure of neutral and charged excitons in self-assembled In(Ga)As/(Al)GaAs quantum dots*, Physical Review B, **65**, 195315 (2002)

[84] T. Kazimierczuk, D. Fröhlich, S. Scheel, H. Stolz, and M. Bayer, *Giant Rydberg excitons in the copper oxide Cu_2O*, Nature, **514**(7522), 343 (2014)

[85] S. W. Koch, M. Kira, G. Khitrova, and H. M. Gibbs, *Semiconductor excitons in new light*, Nature Materials, **5**(7), 523 (2006)

[86] M. A. Lampert, *Mobile and Immobile Effective-Mass-Particle Complexes in Nonmetallic Solids*, Physical Review Letters, **1**, 450 (1958)

[87] K. Kheng, R. T. Cox, M. Y. d' Aubigné, F. Bassani, K. Saminadayar, and S. Tatarenko, *Observation of negatively charged excitons X^- in semiconductor quantum wells*, Physical Review Letters, **71**, 1752 (1993)

[88] Y. R. Shen, *The principles of nonlinear optics*, John Wiley & Sons, New York (1984)

[89] P. W. Milonni and J. H. Eberly, *Laser Physics*, John Wiley & Sons, New Jersey, 2nd edition (2010)

[90] H. Haug and S. W. Koch, *Quantum theory of the optical and electronic properties of semiconductors*, World Scientific, Singapore, 4th edition (2004)

[91] R. v. Baltz, *Semiconductor Bloch equations*, in Klingshirn [62], chapter 27, 761–781

[92] R. P. Feynman, F. L. Vernon, and R. W. Hellwarth, *Geometrical Representation of the Schrödinger Equation for Solving Maser Problems*, Journal of Applied Physics, **28**(1), 49 (1957)

[93] T. Mossberg, A. Flusberg, R. Kachru, and S. R. Hartmann, *Total Scattering Cross Section for Na on He Measured by Stimulated Photon Echoes*, Physical Review Letters, **42**, 1665 (1979)

[94] N. Takeuchi and A. Szabo, *Observation of photon echoes using a nitrogen laser pumped dye laser*, Physics Letters A, **50**(5), 361 (1974)

[95] L. Schultheis, M. D. Sturge, and J. Hegarty, *Photon echoes from two-dimensional excitons in GaAs-AlGaAs quantum wells*, Applied Physics Letters, **47**(9), 995 (1985)

[96] G. Noll, U. Siegner, S. G. Shevel, and E. O. Göbel, *Picosecond stimulated photon echo due to intrinsic excitations in semiconductor mixed crystals*, Physical Review Letters, **64**, 792 (1990)

[97] M. D. Webb, S. T. Cundiff, and D. G. Steel, *Observation of time-resolved picosecond stimulated photon echoes and free polarization decay in GaAs/AlGaAs multiple quantum wells*, Physical Review Letters, **66**, 934 (1991)

[98] D. A. Wiersma and K. Duppen, *Picosecond Holographic-Grating Spectroscopy*, Science, **237**(4819), 1147 (1987)

[99] D. S. Chemla and J. Shah, *Many-body and correlation effects in semiconductors*, Nature, **411**(6837), 549 (2001)

[100] V. V. Samartsev, *Coherent optical spectroscopy of promising materials for solid-state optical processors*, Laser Physics, **20**(2), 383 (2010)

[101] E. Saglamyurek, N. Sinclair, J. Jin, J. A. Slater, D. Oblak, F. Bussières, M. George, R. Ricken, W. Sohler, and W. Tittel, *Broadband waveguide quantum memory for entangled photons*, Nature, **469**(7331), 512 (2011)

[102] E. K. Zavoisky, *Relaxation of liquid solutions for perpendicular fields*, Journal of Physics – USSR, **9**, 211 (1945)

[103] E. K. Zavoisky, *Spin magnetic resonance in the decimetre-wave region*, Journal of Physics – USSR, **10**, 197 (1946)

[104] H. Kuchling, *Taschenbuch der Physik*, Carl Hanser Verlag, München, 21st edition (2014)

[105] L. M. Roth, B. Lax, and S. Zwerdling, *Theory of Optical Magneto-Absorption Effects in Semiconductors*, Physical Review, **114**, 90 (1959)

[106] D. Bimberg (editor), *Semiconductor Nanostructures*, Springer, Berlin, Heidelberg (2008)

[107] R. J. Elliott, *Theory of the effect of spin-orbit coupling on magnetic resonance in some semiconductors*, Physical Review, **96**(2), 266 (1954)

[108] Y. Yafet, *g factor and spin-lattice relaxation of conduction electrons*, in F. Seitz and D. Turnbull (editors), *Solid State Physics*, chapter 1, 1–98, Academic Press (1963)

[109] R. T. Harley, *Spin Dynamics of Free Carriers in Quantum Wells*, in Dyakonov [78], chapter 2, 29–54

[110] G. Dresselhaus, *Spin-orbit coupling effects in zinc blende structures*, Physical Review, **100**(2), 580 (1955)

[111] G. E. Pikus and A. N. Titkov, *Spin relaxation under optical orientation in semiconductors*, in Meier and Zakharchenya [55], chapter 3, 73–132

[112] M. I. Dyakonov and A. V. Khaetskii, *Relaxation of nonequilibrium carrier-density matrix in semiconductors with degenerate bands*, JETP Letters, **59**(5) (1984)

[113] Y. A. Bychkov and E. I. Rashba, *Oscillatory effects and the magnetic susceptibility of carriers in inversion layers*, Journal of Physics C: Solid State Physics, **17**(33), 6039 (1984)

[114] Y. A. Bychkov and E. I. Rashba, *Properties of a 2D electron gas with lifted spectral degeneracy*, JETP Letters, **39**(2), 78 (1984)

[115] T. Uenoyama and L. J. Sham, *Hole relaxation and luminescence polarization in doped and undoped quantum wells*, Physical Review Letters, **64**, 3070 (1990)

[116] R. Ferreira and G. Bastard, *"Spin"-flip scattering of holes in semiconductor quantum wells*, Physical Review B, **43**, 9687 (1991)

[117] R. J. Seymour, M. R. Junnarkar, and R. R. Alfano, *Spin relaxation of photogenerated degenerate electron distributions in GaAs*, Physical Review B, **24**, 3623 (1981)

[118] T. C. Damen, L. Viña, J. E. Cunningham, J. Shah, and L. J. Sham, *Subpicosecond spin relaxation dynamics of excitons and free carriers in GaAs quantum wells*, Physical Review Letters, **67**, 3432 (1991)

[119] P. Roussignol, P. Rolland, R. Ferreira, C. Delalande, G. Bastard, A. Vinattieri, J. Martinez-Pastor, L. Carraresi, M. Colocci, J. F. Palmier, and B. Etienne, *Hole polarization and slow hole-spin relaxation in an n -doped quantum-well structure*, Physical Review B, **46**, 7292 (1992)

[120] L. Viña, T. Damen, J. E. Cunningham, J. Shah, and L. J. Sham, *Spin dynamics in doped and intrinsic GaAs quantum wells*, Physica Scripta, **T49B**, 464 (1993)

[121] L. Viña, *Spin relaxation in low-dimensional systems*, Journal of Physics: Condensed Matter, **11**(31), 5929 (1999)

[122] B. Dareys, T. Amand, X. Marie, B. Baylac, J. Barrau, M. Brousseau, I. Razdobreev, and D. J. Dunstan, *Spin relaxation of excitons in strained InGaAs/GaAs quantum wells*, Le Journal de Physique IV, **03**(C5), 351 (1993)

[123] A. Vinattieri, J. Shah, T. C. Damen, D. S. Kim, L. N. Pfeiffer, M. Z. Maialle, and L. J. Sham, *Exciton dynamics in GaAs quantum wells under resonant excitation*, Physical Review B, **50**, 10868 (1994)

[124] T. Amand and X. Marie, *Exciton Spin Dynamics in Semiconductor Quantum Wells*, in Dyakonov [78], chapter 3, 55–89

[125] T. Amand, B. Dareys, B. Baylac, X. Marie, J. Barrau, M. Brousseau, D. J. Dunstan, and R. Planel, *Exciton formation and hole-spin relaxation in intrinsic quantum wells*, Physical Review B, **50**, 11624 (1994)

[126] D. W. Snoke, W. W. Rühle, K. Köhler, and K. Ploog, *Spin flip of excitons in GaAs quantum wells*, Physical Review B, **55**, 13789 (1997)

[127] E. A. de Andrada e Silva and G. C. La Rocca, *Exciton-bound electron-spin relaxation*, Physical Review B, **56**, 9259 (1997)

[128] M. Goldman, *Formal Theory of Spin–Lattice Relaxation*, Journal of Magnetic Resonance, **149**(2), 160 (2001)

[129] S. J. Blundell, *Magnetism in Condensed Matter*, Oxford University Press, Oxford (2001)

[130] J. K. Furdyna, *Diluted magnetic semiconductors*, Journal of Applied Physics, **64**(4), R29 (1988), URL `http://dx.doi.org/10.1063/1.341700`

[131] H. Ohno, *Making Nonmagnetic Semiconductors Ferromagnetic*, Science, **281**(5379), 951 (1998)

[132] V. F. Agekyan, *Intracenter transitions of iron-group ions in II–VI semiconductor matrices*, Physics of the Solid State, **44**(11), 2013 (2002)

[133] P. W. Bridgman, *Certain Physical Properties of Single Crystals of Tungsten, Antimony, Bismuth, Tellurium, Cadmium, Zinc, and Tin*, Proceedings of the American Academy of Arts and Sciences, **60**(6), 305 (1925)

[134] R. R. Gałązka and T. Wojtowicz, *CdTe-Based Semimagnetic Semiconductors*, in Siffert and Triboulet [187], 133 – 168

[135] F. Hund, *Zur Deutung der Molekelspektren. I*, Zeitschrift für Physik, **40**(10), 742 (1927)

[136] F. Hund, *Zur Deutung der Molekelspektren. II*, Zeitschrift für Physik, **42**(2-3), 93 (1927)

[137] D. Yakovlev, U. Zehnder, W. Ossau, A. Waag, G. Landwehr, T. Wojtowicz, G. Karczewski, and J. Kossut, *Optical study of spin glass-like transition in epilayers and quantum well structures containing $Cd_{1-x}Mn_xTe$*, Journal of Magnetism and Magnetic Materials, **191**(1-2), 25 (1999)

[138] S. Oseroff and P. H. Keesom, *Magnetic Properties: Macroscopic Studies*, in J. K. Furdyna and J. Kossut (editors), *Semiconductors and Semimetals, Volume 25: Diluted Magnetic Semiconductors*, 73–123, Academic Press, Boston (1988)

[139] Y. Shapira, *Magnetization steps in dilute magnetic semiconductors (invited)*, Journal of Applied Physics, **67**(9), 5090 (1990)

[140] S. B. Oseroff, *Magnetic susceptibility and EPR measurements in concentrated spin-glasses: $Cd_{1-x}Mn_xTe$ and $Cd_{1-x}Mn_xSe$*, Physical Review B, **25**(11), 6584 (1982)

[141] M. A. Novak, O. G. Symko, D. J. Zheng, and S. Oseroff, *Spin freezing below the nearest-neighbor percolation concentration in $Cd_{1-x}Mn_xTe$ and $Cd_{1-x}Mn_xSe$*, Physical Review B, **33**(9), 6391 (1986)

[142] S. C. van der Marck, *Calculation of Percolation Thresholds in High Dimensions for FCC, BCC and Diamond Lattices*, International Journal of Modern Physics C, **09**(04), 529 (1998)

[143] J. Vannimenus and G. Toulouse, *Theory of the frustration effect. II. Ising spins on a square lattice*, Journal of Physics C: Solid State Physics, **10**(18), L537 (1977)

[144] S. F. Edwards and P. W. Anderson, *Theory of spin glasses*, Journal of Physics F: Metal Physics., **5**(5), 965 (1975)

[145] D. Sherrington and S. Kirkpatrick, *Solvable Model of a Spin-Glass*, Physical Review Letters, **35**, 1792 (1975)

[146] K. Binder and A. P. Young, *Spin glasses: Experimental facts, theoretical concepts, and open questions*, Reviews of Modern Physics, **58**, 801 (1986)

[147] R. R. Gałązka, S. Nagata, and P. H. Keesom, *Paramagnetic—spin-glass—antiferromagnetic phase transitions in $Cd_{1-x}Mn_xTe$ from specific heat and magnetic susceptibility measurements*, Physical Review B, **22**(7), 3344 (1980)

[148] G. Czycholl, *Theoretische Festkörperphysik*, Springer, Berlin, 3rd edition (2008)

[149] N. T. Khoi and J. A. Gaj, *Fundamental absorption edge of $Cd_{1-x}Mn_xTe$ mixed crystals*, physica status solidi (b), **83**(2), K133 (1977)

[150] J. A. Gaj, R. R. Gałązka, and M. Nawrocki, *Giant exciton Faraday rotation in $Cd_{1-x}Mn_xTe$ mixed crystals*, Solid State Communications, **25**(3), 193 (1978)

[151] W. M. Becker, *Band Structure and Optical Properties of Wide-Gap $A^{II}_{1-x}Mn_xB^{VI}$ Alloys at Zero Magnetic Field*, in J. K. Furdyna and J. Kossut (editors), *Semiconductors and Semimetals, Volume 25: Diluted Magnetic Semiconductors*, 35–72, Academic Press, Boston (1988)

[152] M. P. Vecchi, W. Giriat, and L. Videla, *Photoluminescence studies of the Mn^{2+} d-levels in $Cd_{1-x}Mn_xTe$*, Applied Physics Letters, **38**(2), 99 (1981)

[153] G. F. Koster, J. O. Dimmock, R. G. Wheeler, and H. Statz, *Properties of the thirty-two point groups*, M.I.T. Press, Cambridge, Massachusetts (1963)

[154] M. S. Dresselhaus, G. Dresselhaus, and A. Jorio, *Group Theory*, Springer Science + Business Media, Berlin, Heidelberg (2008)

[155] W. Pauli, *Über den Zusammenhang des Abschlusses der Elektronengruppen im Atom mit der Komplexstruktur der Spektren*, Zeitschrift für Physik, **31**(1), 765 (1925)

[156] W. Heisenberg, *Zur Theorie des Ferromagnetismus*, Zeitschrift für Physik, **49**(9-10), 619 (1928)

[157] P. A. M. Dirac, *Quantum Mechanics of Many-Electron Systems*, Proceedings of the Royal Society of London A: Mathematical, Physical and Engineering Sciences, **123**(792), 714 (1929)

[158] M. A. Ruderman and C. Kittel, *Indirect Exchange Coupling of Nuclear Magnetic Moments by Conduction Electrons*, Physical Review, **96**, 99 (1954)

[159] T. Kasuya, *A Theory of Metallic Ferro- and Antiferromagnetism on Zener's Model*, Progress of Theoretical Physics, **16**(1), 45 (1956)

[160] K. Yosida, *Magnetic Properties of Cu-Mn Alloys*, Physical Review, **106**, 893 (1957)

[161] H. Kramers, *L'interaction Entre les Atomes Magnétogènes dans un Cristal Paramagnétique*, Physica, **1**(1-6), 182 (1934)

[162] P. W. Anderson, *Antiferromagnetism. Theory of Superexchange Interaction*, Physical Review, **79**(2), 350 (1950)

[163] J. B. Goodenough, *Theory of the Role of Covalence in the Perovskite-Type Manganites* $[La, M(II)]MnO_3$, Physical Review, **100**(2), 564 (1955)

[164] J. Kanamori, *Superexchange interaction and symmetry properties of electron orbitals*, Journal of Physics and Chemistry of Solids, **10**(2-3), 87 (1959)

[165] S. D. Sarma, E. H. Hwang, and A. Kaminski, *How to make semiconductors ferromagnetic: a first course on spintronics*, Solid State Communications, **127**(2), 99 (2003)

[166] T. Jungwirth, J. Sinova, J. Mašek, J. Kučera, and A. H. MacDonald, *Theory of ferromagnetic (III, Mn)V semiconductors*, Reviews of Modern Physics, **78**(3), 809 (2006)

[167] A. M. Nazmul, S. Sugahara, and M. Tanaka, *Ferromagnetism and high Curie temperature in semiconductor heterostructures with Mn δ-doped GaAs and p-type selective doping*, Physical Review B, **67**, 241308 (2003)

[168] H. Ohno, *Properties of ferromagnetic III–V semiconductors*, Journal of Magnetism and Magnetic Materials, **200**(1-3), 110 (1999)

[169] K. C. Ku, S. J. Potashnik, R. F. Wang, S. H. Chun, P. Schiffer, N. Samarth, M. J. Seong, A. Mascarenhas, E. Johnston-Halperin, R. C. Myers, A. C. Gossard, and D. D. Awschalom, *Highly enhanced Curie temperature in low-temperature annealed [Ga,Mn]As epilayers*, Applied Physics Letters, **82**(14), 2302 (2003)

[170] D. Chiba, K. Takamura, F. Matsukura, and H. Ohno, *Effect of low-temperature annealing on (Ga,Mn)As trilayer structures*, Applied Physics Letters, **82**(18), 3020 (2003)

[171] M. B. Stone, K. C. Ku, S. J. Potashnik, B. L. Sheu, N. Samarth, and P. Schiffer, *Capping-induced suppression of annealing effects on* $Ga_{1-x}Mn_xAs$ *epilayers*, Applied Physics Letters, **83**(22), 4568 (2003)

[172] T. Dietl, *A ten-year perspective on dilute magnetic semiconductors and oxides*, Nature Materials, **9**, 965–974 (2010)

[173] K. M. Yu, W. Walukiewicz, T. Wojtowicz, I. Kuryliszyn, X. Liu, Y. Sasaki, and J. K. Furdyna, *Effect of the location of Mn sites in ferromagnetic* $Ga_{1-x}Mn_xAs$ *on its Curie temperature*, Physical Review B, **65**, 201303 (2002)

[174] K. W. Edmonds, P. Bogusławski, K. Y. Wang, R. P. Campion, S. N. Novikov, N. R. S. Farley, B. L. Gallagher, C. T. Foxon, M. Sawicki, T. Dietl, M. B. Nardelli, and J. Bernholc, *Mn Interstitial Diffusion in (Ga,Mn)As*, Physical Review Letters, **92**(3) (2004)

[175] D. E. Bliss, W. Walukiewicz, J. W. Ager, E. E. Haller, K. T. Chan, and S. Tanigawa, *Annealing studies of low-temperature-grown GaAs:Be*, Journal of Applied Physics, **71**(4), 1699 (1992)

[176] G. A. Prinz, *Hybrid Ferromagnetic-Semiconductor Structure*, Science, **250**(4984), 1092 (1990)

[177] B. P. Zakharchenya and V. L. Korenev, *Integrating magnetism into semiconductor electronics*, Physics-Uspekhi, **48**(6), 603 (2005)

[178] V. L. Korenev, *Optical orientation in ferromagnet/semiconductor hybrids*, Semiconductor Science and Technology, **23**(11), 114012 (2008)

[179] V. L. Korenev, M. Salewski, I. A. Akimov, V. F. Sapega, L. Langer, I. V. Kalitukha, J. Debus, R. I. Dzhioev, D. R. Yakovlev, D. Müller, C. Schröder, H. Hövel, G. Karczewski, M. Wiater, T. Wojtowicz, Y. G. Kusrayev, and M. Bayer, *Long-range p–d exchange interaction in a ferromagnet–semiconductor hybrid structure*, Nature Physics, **12**(1), 85 (2015)

[180] Y. Lee and A. Ramdas, *A piezomodulation study of the absorption edge and Mn^{++} internal transition in $Cd_{1-x}Mn_xTe$, a prototype of diluted magnetic semiconductors*, Solid State Communications, **51**(11), 861 (1984), URL `http://dx.doi.org/10.1016/0038-1098(84)91088-3`

[181] G. B. Stringfellow, *Organometallic Vapor-Phase Epitaxy: Theory and Practice*, Academic Press, San Diego, London, 2nd edition (1998)

[182] J. Harris, *Delta-doping of semiconductors*, Journal of Materials Science: Materials in Electronics, **4**(2), 93 (1993)

[183] M. Dorokhin, Y. Danilov, P. Demina, V. Kulakovskii, O. Vikhrova, S. Zaitsev, and B. Zvonkov, *Emission properties of InGaAs/GaAs heterostructures with δ<Mn>-doped barrier*, Journal of Physics D: Applied Physics, **41**(24), 245110 (2008)

[184] M. Pankov, B. Aronzon, V. Rylkov, A. Davydov, E. Meilikhov, R. Farzetdinova, M. Pashaev, M. Chuev, I. Subbotin, I. Likhachev, B. Zvonkov, A. Lashkul, and R. Laiho, *Ferromagnetic transition in $GaAs/Mn/GaAs/In_xGa_{1-x}As/GaAs$ structures with a two-dimensional hole gas*, Journal of Experimental and Theoretical Physics, **109**(2), 293 (2009)

[185] W. Hanle, *Über magnetische Beeinflussung der Polarisation der Resonanzfluoreszenz*, Zeitschrift für Physik, **30**(1), 93 (1924)

[186] I. D. Abella, N. A. Kurnit, and S. R. Hartmann, *Photon Echoes*, Physical Review, **141**(1), 391 (1966)

[187] R. Siffert and P. Triboulet (editors), *CdTe and Related Compounds; Physics, Defects, Hetero- and Nano-structures, Crystal Growth, Surfaces and Applications*, European Materials Research Society Series, Elsevier, Amsterdam (2010)

[188] J. K. Furdyna and N. Samarth, *Magnetic properties of diluted magnetic semiconductors: A review (invited)*, Journal of Applied Physics, **61**(8), 3526 (1987)

[189] I. A. Akimov, R. I. Dzhioev, V. L. Korenev, Y. G. Kusrayev, V. F. Sapega, D. R. Yakovlev, and M. Bayer, *Electron spin dynamics and optical orientation of Mn^{2+} ions in GaAs*, Journal of Applied Physics, **113**(13), 136501 (2013)

[190] V. Abramishvili, A. Komarov, S. Ryabchenko, and Y. Semenov, *Magnetic-field affected luminescence of Mn^{2+} ions in $Zn_{1-x}Mn_xSe$ compounds under resonance excitation of excitons*, Solid State Communications, **78**(12), 1069 (1991)

[191] M. Nawrocki, Y. G. Rubo, J. P. Lascaray, and D. Coquillat, *Suppression of the Auger recombination due to spin polarization of excess carriers and* Mn^{2+} *ions in the semimagnetic semiconductor* $Cd_{0.95}Mn_{0.05}S$, Physical Review B, **52**, R2241 (1995)

[192] J. D. Park, S. Yamamoto, J. Watanabe, K. Takamura, and J. Nakahara, *Decay Profiles of Mn^{2+} Photoluminescence in CdMnTe*, Journal of the Physical Society of Japan, **66**(10), 3289 (1997)

[193] E. Müller, W. Gebhardt, and V. Gerhardt, *Excition Transfer Between the Manganese Ions in the Semiconductor Alloy $Cd_{1-x}Mn_xTe$ With $x = 0.51$*, physica status solidi (b), **113**(1), 209 (1982)

[194] C. Le Gall, L. Besombes, H. Boukari, R. Kolodka, J. Cibert, and H. Mariette, *Optical Spin Orientation of a Single Manganese Atom in a Semiconductor Quantum Dot Using Quasiresonant Photoexcitation*, Physical Review Letters, **102**, 127402 (2009)

[195] M. Goryca, T. Kazimierczuk, M. Nawrocki, A. Golnik, J. A. Gaj, P. Kossacki, P. Wojnar, and G. Karczewski, *Optical Manipulation of a Single Mn Spin in a CdTe-Based Quantum Dot*, Physical Review Letters, **103**, 087401 (2009)

[196] K. A. Baryshnikov, L. Langer, I. A. Akimov, V. L. Korenev, Y. G. Kusrayev, N. S. Averkiev, D. R. Yakovlev, and M. Bayer, *Resonant optical alignment and orientation of Mn^{2+} spins in CdMnTe crystals*, Physical Review B, **92**(20) (2015)

[197] D. Heiman, P. Becla, R. Kershaw, D. Ridgley, K. Dwight, A. Wold, and R. R. Gałązka, *Field-induced exchange effects in (Cd, Mn)Te and (Cd, Mn)Se from photoluminescence measurements*, Physical Review B, **34**(6), 3961 (1986)

[198] M. M. Moriwaki, W. M. Becker, W. Gebhardt, and R. R. Gałązka, *Study of the 2.0-eV photoluminescence band in $Cd_{1-x}Mn_xTe$ semiconductor alloys*, Physical Review B, **26**(6), 3165 (1982)

[199] N. Vasilyev, *Intra-center energy transfer dynamics in $Cd_{1-x}Mn_xTe$ semi magnetic semiconductors*, Journal of Luminescence, **132**(5), 1215 (2012)

[200] H. Schenk, M. Wolf, G. Mackh, U. Zehnder, W. Ossau, A. Waag, and G. Landwehr, *Influence of the negative thermal-expansion coefficient on the luminescence properties of (CdMnMg)Te*, Journal of Applied Physics, **79**(11), 8704 (1996)

[201] D. Varshalovich, A. Moskalev, and V. Khersonskii, *Quantum Theory Of Angular Momemtum*, World Scientific, Singapore (1988)

[202] D. Leinen, *Excitonic energy transfer to the 3d electrons of Mn^{2+} in $Cd_{1-x}Mn_xTe$*, Physical Review B, **55**, 6975 (1997)

[203] V. L. Korenev, I. A. Akimov, S. V. Zaitsev, V. F. Sapega, L. Langer, D. R. Yakovlev, Y. A. Danilov, and M. Bayer, *Dynamic spin polarization by orientation-dependent separation in a ferromagnet–semiconductor hybrid*, Nature Communications, **3**, 959 (2012)

[204] I. A. Akimov, V. L. Korenev, V. F. Sapega, L. Langer, S. V. Zaitsev, Y. A. Danilov, D. R. Yakovlev, and M. Bayer, *Orientation of electron spins in hybrid ferromagnet-semiconductor nanostructures*, physica status solidi (b), **251**(9), 1663 (2014)

[205] V. Sapega, T. Ruf, and M. Cardona, *Spin-Flip Raman Study of Exchange Interactions in Bulk GaAs:Mn*, physica status solidi (b), **226**(2), 339 (2001)

[206] R. J. Epstein, I. Malajovich, R. K. Kawakami, Y. Chye, M. Hanson, P. M. Petroff, A. C. Gossard, and D. D. Awschalom, *Spontaneous spin coherence in n -GaAs produced by ferromagnetic proximity polarization*, Physical Review B, **65**, 121202 (2002)

[207] C. Ciuti, J. P. McGuire, and L. J. Sham, *Spin Polarization of Semiconductor Carriers by Reflection off a Ferromagnet*, Physical Review Letters, **89**, 156601 (2002)

[208] D. Brinkmann, J. Kudrna, P. Gilliot, B. Hönerlage, A. Arnoult, J. Cibert, and S. Tatarenko, *Trion and exciton dephasing measurements in modulation-doped quantum wells: A probe for trion and carrier localization*, Physical Review B, **60**(7), 4474 (1999)

[209] J. Debus, D. Dunker, V. F. Sapega, D. R. Yakovlev, G. Karczewski, T. Wojtowicz, J. Kossut, and M. Bayer, *Spin-flip Raman scattering of the neutral and charged excitons confined in a CdTe/(Cd,Mg)Te quantum well*, Physical Review B, **87**, 205316 (2013)

[210] E. A. Zhukov, D. R. Yakovlev, M. Bayer, M. M. Glazov, E. L. Ivchenko, G. Karczewski, T. Wojtowicz, and J. Kossut, *Spin coherence of a two-dimensional electron gas induced by resonant excitation of trions and excitons in $CdTe/(Cd,Mg)Te$ quantum wells*, Physical Review B, **76**(20), 205310 (2007)

[211] A. A. Sirenko, T. Ruf, M. Cardona, D. R. Yakovlev, W. Ossau, A. Waag, and G. Landwehr, *Electron and hole g factors measured by spin-flip Raman scattering in $CdTe/Cd_{1-x}Mg_xTe$ signle quantum wells*, Physical Review B, **56**(4), 2114 (1997)

[212] L. Langer, S. V. Poltavtsev, I. A. Yugova, D. R. Yakovlev, G. Karczewski, T. Wojtowicz, J. Kossut, I. A. Akimov, and M. Bayer, *Magnetic-Field Control of Photon Echo from the Electron-Trion System in a CdTe Quantum Well: Shuffling Coherence between Optically Accessible and Inaccessible States*, Physical Review Letters, **109**, 157403 (2012)

[213] L. Langer, S. Poltavtsev, I. Yugova, M. Salewski, D. Yakovlev, G. Karczewski, T. Wojtowicz, I. Akimov, and M. Bayer, *Access to long-term optical memories using photon echoes retrieved from semiconductor spins*, Nature Photonics, **8**(11), 851 (2014)

[214] E. A. Zhukov, D. R. Yakovlev, M. Bayer, G. Karczewski, T. Wojtowicz, and J. Kossut, *Spin coherence of two-dimensional electron gas in CdTe/(Cd, Mg)Te quantum wells*, physica status solidi (b), **243**(4), 878 (2006)

[215] H. Hoffmann, G. V. Astakhov, T. Kiessling, W. Ossau, G. Karczewski, T. Wojtowicz, J. Kossut, and L. W. Molenkamp, *Optical spin pumping of modulation-doped electrons probed by a two-color Kerr rotation technique*, Physical Review B, **74**(7) (2006)

[216] G. V. Astakhov, M. M. Glazov, D. R. Yakovlev, E. A. Zhukov, W. Ossau, L. W. Molenkamp, and M. Bayer, *Time-resolved and continuous-wave optical spin pumping of semiconductor quantum wells*, Semiconductor Science and Technology, **23**(11), 114001 (2008)

[217] A. T. Hanbicki, O. M. J. van 't Erve, R. Magno, G. Kioseoglou, C. H. Li, B. T. Jonker, G. Itskos, R. Mallory, M. Yasar, and A. Petrou, *Analysis of the transport process providing spin injection through an Fe/AlGaAs Schottky barrier*, Applied Physics Letters, **82**(23), 4092 (2003)

[218] C. Song, M. Sperl, M. Utz, M. Ciorga, G. Woltersdorf, D. Schuh, D. Bougeard, C. H. Back, and D. Weiss, *Proximity Induced Enhancement of the Curie Temperature in Hybrid Spin Injection Devices*, Physical Review Letters, **107**(5) (2011)

[219] G. S. Uhrig, *Exact results on dynamical decoupling by π pulses in quantum information processes*, New Journal of Physics, **10**(8), 083024 (2008)

[220] M. Lovrić, D. Suter, A. Ferrier, and P. Goldner, *Faithful Solid State Optical Memory with Dynamically Decoupled Spin Wave Storage*, Physical Review Letters, **111**(2) (2013)

[221] I. A. Yugova, M. M. Glazov, E. L. Ivchenko, and A. L. Efros, *Pump-probe Faraday rotation and ellipticity in an ensemble of singly charged quantum dots*, Physical Review B, **80**, 104436 (2009)

List of publications

1. V. L. Korenev, I. A. Akimov, S. V. Zaitsev, V. F. Sapega, L. Langer, D. R. Yakovlev, Yu. A. Danilov, M. Bayer: *Dynamic spin polarization by orientation-dependent separation in a ferromagnet-semiconductor hybrid*, Nature Communications, **3**, 959 (2012).

2. Ł. Langer, S. V. Poltavtsev, I. A. Yugova, D. R. Yakovlev, G. Karczewski, T. Wojtowicz, J. Kossut, I. A. Akimov, M. Bayer: *Magnetic-Field Control of Photon Echo from the Electron-Trion System in a CdTe Quantum Well: Shuffling Coherence between Optically Accessible and Inaccessible States*, Physical Review Letters, **109**, 157403 (2012).

3. I. A. Akimov, V. L. Korenev, V. F. Sapega, L. Langer, S. V. Zaitsev, Yu. A. Danilov, D. R. Yakovlev, M. Bayer: *Orientation of electron spins in hybrid ferromagnet-semiconductor nanostructures*, physica status solidi (b), **251**(9), 1663 (2014).

4. L. Langer, S. V. Poltavtsev, I. A. Yugova, M. Salewski, D. R. Yakovlev, G. Karczewski, T. Wojtowicz, I. A. Akimov, M. Bayer: *Access to long-term optical memories using photon echoes retrieved from semiconductor spins*, Nature Photonics **8**, 851 (2014).

5. K. A. Baryshnikov, L. Langer, I. A. Akimov, V. L. Korenev, Yu. G. Kusrayev, N. S. Averkiev, D. R. Yakovlev, M. Bayer: *Resonant optical alignment and orientation of Mn^{2+} spins in CdMnTe crystals*, Physical Review B **92**, 205202 (2015).

6. V. L. Korenev, M. Salewski, I. A. Akimov, V. F. Sapega, L. Langer, I. V. Kalitukha, J. Debus, R. I. Dzhioev, D. R. Yakovlev, D. Müller, C. Schröder, H. Hövel, G. Karczewski, M. Wiater, T. Wojtowicz, Yu. G. Kusrayev, M. Bayer: *Long-range p-d exchange interaction in a ferromagnet-semiconductor hybrid structure*, Nature Physics **12**, 85 (2016).

7. S. V. Nekrasov, Yu. G. Kusrayev, I. A. Akimov, V. L. Korenev, L. Langer, M. Salewski: *Negative circular polarization dynamics in InP/InGaP quantum dots*, Journal of Physics: Conference Series **741** 012189 (2016).

8. S. V. Zaitsev, I. A. Akimov, L. Langer, Yu. A. Danilov, M. V. Dorokhin, B. N. Zvonkov, D. R. Yakovlev, M. Bayer: *Coherent Spin Dynamics of Carriers in Ferromagnetic Semiconductor Heterostructures with an Mn δ Layer*, Journal of Experimental and Theoretical Physics, **123**(3), 420 (2016).

Acknowledgements

Finally, I would like to thank everyone who contributed to the successful completion of my thesis by helping, correcting, supporting, and encouraging me.

I am deeply grateful to PD Dr. Ilya Akimov for advising and mentoring me as his diploma- and PhD-student. His excellent scientific intuition was of vital importance for all crossroads of my scientific career. It was a pleasure to learn from his great experimental skill and profound knowledge.

Special thanks are due to Prof. Dr. Manfred Bayer for the opportunity to perform these studies at his chair and for providing excellent circumstances for such endeavors.

I am grateful to Prof. Dr. Dmitri Yakovlev for providing further advice and ideas.

For the help in the lab, countless discussions, and pleasant company I would like to thank Dr. Sergey Poltavtsev and Matthias Salewski.

I appreciate the fruitful collaborations and excellent teamwork with Dr. Irina Yugova, Prof. Dr. Vladimir Korenev, Prof. Dr. Victor Sapega, and Prof. Dr. Sergey Zaitsev - спасибо!

Thank you to all current and former members of E2 with whom I have shared time and who have accompanied me to conferences, who I have fenced with at christmas parties, who were available for the exchange of ideas, and especially to those I have become friends with.

I want to explicitly thank the non-scientific staff Nina Collette, Michaela Wäscher, Klaus Wiegers, Lars Wieschollek, and Thomas Stöhr for administrative and technical solutions.

In the completion of the written part of the thesis, valuable proofreading was performed by Arnd Behring, Julia and Sven Beulshausen, Jörg Debus, Johannes Thewes, and Steffen Varwig.

Finally I want to express my deepest gratitude to my parents Ulrike and Detlef, to my brother Felix, to my wife Felicitas and to my son Julian for their unconditional and continued financial, emotional and universal support, for their patience, and for taking care of all the non-scientific aspects of my life.